Metal Nanoparticles over Active Ionic-Conductive Supports for the Reverse Water Gas Shift Reaction

Raha Einakchi

Thesis submitted to the Faculty of Graduate and
Postdoctoral Studies in partial fulfillment of the
requirements for the M.A.Sc degree

In the

Department of Chemical and Biological Engineering
University of Ottawa

Abstract:

Increases in carbon dioxide emissions due to economic activity induce global warming. The strong increase in energy demand, mainly based on oil and coal, induces a rapid increase in CO_2 in the atmosphere. Within Canada, the amount of human-produced carbon dioxide is considerable because a large portion of energy is supplied by burning of fossil fuels. The Reverse Water Gas Shift (RWGS) reaction is a promising catalytic process for the utilization and subsequent activation of carbon dioxide to carbon monoxide, which can be further converted into fuels such as gasoline. The current thesis studies the development of nano-catalytic systems for the RWGS reaction. Mono- and bi-metallic nanoparticles based on Cu, Fe, Ru and Pt were prepared using a polyol synthesis method. The catalytic performance of three different types of metal oxides (ionically conductive, mixed ionic-electronic conductive and non-conductive) was investigated for the RWGS reaction. Conductive metal oxides including samarium-doped ceria (SDC), ceria (CeO_2), yttria-stabilized zirconia (YSZ) and iron III oxide (Fe_2O_3) were further used as the catalyst supports and the nanoparticles of Cu, Fe, Cu_xFe_{1-x} (x = 50 and 95 at.%), Ru, Pt, $Ru_{50}Pt_{50}$ and Ru_xFe_{1-x} (x = 80 and 90 at.%) were subsequently deposited on them. A stoichiometric mixture of H_2 and CO_2, i.e. $H_2/CO_2 = 1$, was used under atmospheric pressure in the temperature range of 300 - 600°C in order to evaluate the catalyst performance in terms of activity, stability and selectivity. Nanoparticles deposited on ceria-based supports (CeO_2 and SDC) showed superior catalytic performance compared to other metal oxides. Among all the catalyst tested, 5 wt.% $Ru_{50}Pt_{50}/CeO_2$ showed the highest CO yield and satisfactory stability for RWGS reaction. The second best catalytic systems were based on $Ru_{90}Fe_{10}/CeO_2$ and $Ru_{80}Fe_{20}/CeO_2$, which are more attractive from the practical point of view.

Acknowledgments:

I warmly thank my supervisor Dr. Elena Baranova for all her help, encouragement and supervision throughout my M.A.S.c program. Her guidance went a long way toward helping me learn the little I know from heterogeneous catalysis.

I appreciate the assistance of my dear lab mates, Holly Dole and Evans Monyoncho. Their comments and their companionship will be never forgotten. A great thanks goes to Holly for instructing me in the procedure regarding dispersion measurements.

A million thanks goes to Chemical Engineering lab technicians, Louis Tremblay and Gérard Nina, for their continued and enormous help in my laboratory work. I shall never forget their patience and their sincere and prompt assistance in my hour of need throughout my M.A.S.c program.

I would like to acknowledge Dr. Martin Couillard for running scanning transmission electron microscopy (STEM) and annular dark field-scanning electron microscopy (ADF- STEM) over supported and unsupported Ru and Pt nanoparticles. Moreover, I am thankful to Dr. Anis Allagui from Sharja University for carrying out XRD measurements on non-noble metal colloidal nanoparticles.

Many thanks to my dearest friends here in Ottawa, who truly made me feel at home during this journey.

I also am grateful to Dr. Rima Isaifan who kindly was there for me as a mentor and friend during the first semester of my program. My appreciation also goes to Dr. Júlio César Martins da Silva, whom his presence, support and friendship meant a world to me.

Last but not least, my dearest parents; no amount of “thanks” can express my deep love and gratitude. Thanks for instilling me with a passion for learning over the years and thanks again for giving me this amazing opportunity. I simply could not make it through if it was not for you continued love and support.

Table of Contents

Chapter 1: Introduction

Chapter 2: Literature Review

Chapter 3: Catalyst Synthesis, Characterization and Catalytic Set-up

Chapter 4: Characterization of Supported and Unsupported Metal Nanoparticles

Chapter 5: Ionic and Non-ionic Conductive Metal Oxides for RWGS Reaction

Chapter 6: Iron- and Copper-based Nanoparticles for RWGS Reaction

Chapter 7: Platinum- and Ruthenium-based Nanoparticles for RWGS Reaction

Chapter 8: Conclusions and Recommendations

List of Tables:

List of Figures:

Abbreviation	**Definition**
ads	Adsorbed
BET	Brunauer-Emmett-Teller
CAMERE	Carbon dioxide hydrogenation to form methanol
RWGS	Reverse water gas shift
Cat	Catalyst
CCU	Carbon capture and utilization
CCS	Carbon Capture and sequestration
CO_2	Carbon dioxide
EDX	Energy dispersive X-ray spectroscopy
EG	Ethylene glycol
E.g.	For example
EPOC	Electrochemical promotion of catalysts
FF	Fossil fuels
FT	Fischer-Tropsch
GHSV	Gas hourly space velocity
GHG	Greenhouse gas
HTS	High temperature shift
IPPC	Intergovernmental Panel on Climate Change
LTS	Low temperature shift
Me	Metal
MeOH	Methanol
MFC	Mass Flow Controller
MS	Mass spectrometry
MTG	Methanol to Gasoline
NA	Not available
NDIR	Non-dispersive infrared
NPs	Nanoparticles
OSC	Oxygen storage capacity
PEG	Poly Ethylene Glycol
PEM	Proton exchange membrane
PGM	Platinum group metals
PVP	Polyvinylpyrrolidone
RWGS	Reverse water gas shift
SCCM	Standard cubic centimeters
SDC	Samarium-doped ceria
SEM	Scanning electron microscopy
Spec.	Spectrometer
SOFC	Solid oxide fuel cell
Sup	Support
SV	Space velocity
TEG	Tetra Ethylene Glycol
TEM	Transmission electron microscopy
TPB	Triple phase boundary
TOF	Turn over frequencies
TOS	Time-on-stream
TrEG	Triethylene Glycol
WGS	Water gas shift
XPS	X-ray photoelectron spectroscopy
XRD	X-ray diffraction
YSZ	Yttria-stabilized Zirconi\a

Symbol	**Definition**
a.u.	Arbitrary unit
atm	Atmosphere
°C	Degrees Celsius
°	Degree
Ea	Activation energy
E	Molar flow rate
(g)	Gas
h	Hours
k	Kelvin
kcal	Kilo calorie
K_{eq}	Equilibrium constant
N	Reaction order
Oa	Oxygen adatom
X(S)	Oxygen ion from support
ppm	Parts per million
P_x	Partial Pressure of X
W	Weight of catalyst
wt.	Weight
X	Fractional conversion
[ ]	Concentration
2ϴ	Diffraction angle

Nomeclature	**Definition**
cm^2	Centimeter square
Gt	Gigatonnes
h	Hours
k	Kelvin
kcal	Kilo calorie
kg	Kilogram
kPa	Kilopascal
kV	Kilovolt
L	Liters
mg	Milligram
min	Minute
mL	Milliliters
mmol	Millimole
mol	Mole
mW	Milliwatt
m^2	Square meters
nm	Nanometers

Chapter 1

1.1 Introduction

The burning of fossil fuels increases the concentration of green house gases (GHG) and leads to environmental and health hazards. Fossil fuel is still considered as the main resource for the supply of energy in Canada, and therefore it is responsible for generation of large amounts of carbon dioxide (CO_2). It is noticeable that CO_2 contributes over 60 percent to GHGs, which are one of the main causes of global warming. In addition, CO_2 is considered to be responsible for the disruption of the global carbon cycle that can eventually lead to climate change. Carbon cycle is known as a complex cycle through which carbon circulates between different carbon reservoirs such as CO_2 [1].

As reported by the International Panel for Climate Change (IPCC), CO_2 concentration is increasing every year. Over 80% increase in CO_2 level has been reported from the year 2000 to the year 2004 [2]. The climate change caused by CO_2 has severe environmental impacts including melting of ice sheets and consequently rise in the sea levels [3], higher desertification, and ocean acidification because a large portion of emitted CO_2 is released into the oceans [4].

In an attempt to deal with global warming as a worldwide issue, countries committed to decrease their GHG emissions in the long run. In spite of all the integrated strategies for CHG reduction, it is unlikely for the developed carbon emitter industries to have a major contribution in the foreseeable future [5]. CO_2 is regarded as the heart of the global warming crisis. Thus, it is important to set a science-based target for developing new technologies for CO_2 capture and sequestration in the near future.

Numerous technologies have been developed to undertake CO_2 capture and sequestration (CCS) so that the captured CO_2 would be eventually utilized, rather than adding up to the CO_2 levels in the atmosphere. CO_2 storage is mainly referred to keeping it at an appropriate location where it could be used in geological measurements [6]. Although CSS has proved itself as a successful method for atmospheric carbon reduction, but it possesses a number of problems that encourage developing effective CO_2 utilization techniques [7]. For example, CCS cannot be applied to all kinds of carbon emissions since it is mainly suitable for those that occur near safe sites. In addition, this approach is only well suited for large-scale sources of carbon. Furthermore, many risks such as reservoirs leakage and other unknown environmental impacts make this costly approach of much less interest [2].

Unlike CCS, technologies centered on carbon capture and utilization (CCU), proved to be more effective in reducing CO_2 atmospheric levels [8]. This method aims at utilizing CO_2 as a feedstock for the production of high value chemicals and fuels. Availability and the low cost of CO_2 have attracted considerable attention to the utilization of CO_2 as a carbon source. However, CO_2 is a very stable molecule with the enthalpy of formation of -393.51 kJ.mol^{-1}. Therefore, there is a thermodynamic energy obstacle that needs to be overcome in order to activate CO_2 [9]. Using renewable sources (wind, solar, and nuclear energy and etc.) as energy supply, CCU could be considered as a reliable approach for CO_2 mitigation.

The reaction of CO_2 with H_2, also known as CO_2 hydrogenation is one of the effective methods for CO_2 utilization that can lead to the production of a wide range of value-added products [10]. The hydrogenation of CO_2 can be carried out either directly or indirectly to yield different products and fuels. For example, the Sabatier reaction or CO_2 methanation is a CO_2 hydrogenation reaction that directly yields methane [11]. Moreover, the methanol synthesis is another example of direct CO_2 hydrogenation that can result in the formation of methanol (CH_3OH) [12]. In contrast, indirect routes often deal with a multi-stage process and the use of hybrid catalysts active towards different processes. Throughout an indirect hydrogenation, CO_2 would transform to a more reactive intermediate, for example, carbon monoxide (CO) or methanol (CH_3OH) [13]. Products of indirect CO_2 hydrogenation would eventually participate in other reactions to produce the final desirable products.

Figure 1.1 shows a number of direct and indirect CO_2 hydrogenation reactions. It demonstrates the importance of CO that is produced through the Reverse Water Gas Shift (RWGS) reaction. CO can be hydrogenated according to the Fischer-Tropsch (FT) process to result in higher value products such as longer chain hydrocarbons and alcohols. Moreover, CO hydrogenation can also lead to the production of methanol that can be subsequently used in Methanol to Gasoline (MTG) process [14]. In addition, Figure 1.1 also indicates the CAMERE process through which CO_2 is indirectly hydrogenated to produce methanol.

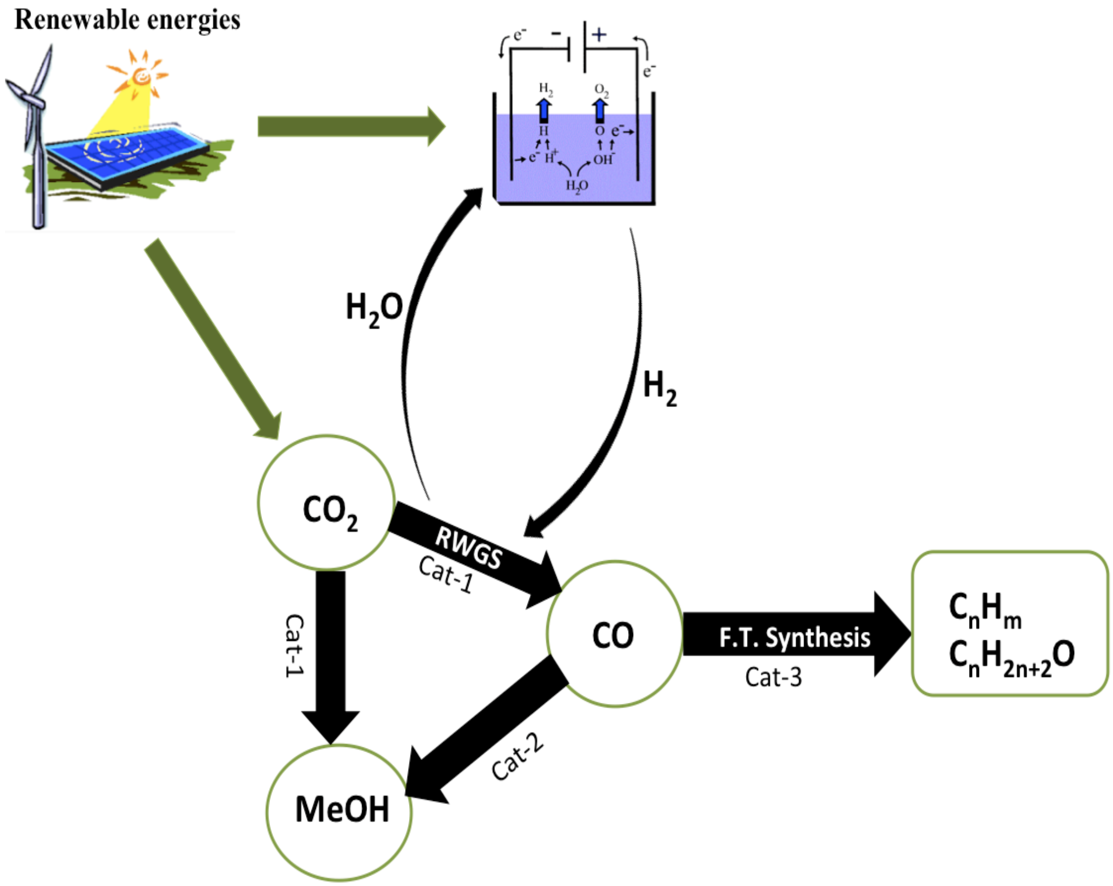

Fig. 1.1: Direct and indirect hydrogenation reactions using H_2 via water electrolysis

In general, H_2 is mainly obtained from fossil sources [15]. Therefore, it is of the greatest concern to supply the hydrogen need using an economical approach. On the other hand, renewable and infinite supplies are required to ensure the sustainability of H_2 production. Biotech-based researches revealed that H_2 could be formed from biomass, green algae as well as cyanobacteria [16]. Nevertheless, electrolysis of water is a more promising approach for H_2 production, in case the renewable sources such as wind or solar energies provide the energy demand [17].

Figure 1.1 demonstrates that the water from the RWGS reaction can be used in the electrolysing unit to form H_2. Therefore, it is evident that both products from the RWGS reaction (CO and H_2O) can be used in order to produce fuels and value-added products. However, it is important to use a renewable source of energy in order to make the whole process sustainable and cost-efficient.

The production of CO through the Reverse Water Gas Shift (RWGS) reaction has attracted renewed attention since CO can be used to produce liquid fuels and hydrocarbons. An interesting feature of RWGS reaction is that it consumes less H_2 compared to other direct CO_2 hydrogenation reactions such as the Sabatier reaction and methanol synthesis [18]. CO_2 hydrogenation reactions powered by renewable energies (e.g. wind, solar and nuclear energies) can be viable solutions for energy saving. Synthetic fuel (mixture of CO and H_2) and other high value products can be further used to produce energy [19]. These approaches are capable of diminishing the need for petroleum-based fuels as well as mitigating CO_2 emissions by a high percentage.

1.2 Motivation:

The growth rate of CO_2 is on the rise and needs to be controlled. Storage reservoirs are finite and their capacity is not sufficient to accommodate CO_2 emissions in the near future [20]. This addresses the unsustainability of the storage techniques. Whereas, CO_2 utilization approaches not only reduce its atmospheric levels, but also open new doors to development of sustainable energy and renewable fuels.

Carbon dioxide is considered as an inexpensive source of carbon. However, it is the most stable carbonaceous material of all that is not desirable in chemical reactions due to its lack of reactivity. In order to induce reactivity, CO_2 can react with H_2 as a reducing agent. Hydrogenation of CO_2 to CO through the Reverse Water Gas Shift (RWGS) reaction is a favourable approach to utilize CO_2. A reliable H_2 supply and thermal energy source as well as appropriate catalysts are required in order to activate CO_2 through RWGS. This reaction is endothermic and the temperature of the reaction can go as high as 900 -1000°C [21]. It is noticeable that less thermal energy would be required with the contribution of heterogeneous catalysis. Moreover, appropriate RWGS catalysts must have high CO selectivity because CH_4 and CH_3OH are two main by-products that could be formed along with CO in direct CO_2 hydrogenation reactions [22]. Hence it can be concluded that the development of suitable catalysts plays a determining role towards the industrialization of RWGS reaction.

To sum it up, it is essential to reduce CO_2 emissions. Canadian coal power plants and other CO_2 emitter industries are required to implement several measures such as CO_2 sequestration and concentration to avoid carrying penalties in the near future. CO can be utilized in many industrial operations including Fisher-Tropsch reaction, metal fabrication, chemical and pharmaceutical manufacturing and electronics. However, it is important to economically optimize RWGS reaction. Therefore, highly active and selective catalysts need to be developed to maximize CO production and simultaneously minimize other direct hydrogenation end products such as CH_4 and CH_3OH.

1.2.1 The Reverse Water Gas Shift (RWGS) Reaction:

CO_2 can be reduced to CO according to the RWGS reaction, Eq. (1.1):

$$CO_2 + H_2 \leftrightarrow CO + H_2O \qquad \Delta H^0_{298} = 41.2 \text{ kJ mol}^{-1} \qquad \text{(Eq. 1.1)}$$

RWGS is an endothermic equilibrium-limited reaction. Thermodynamically, this reaction becomes favourable at high temperatures. In other words, there is a conversion limit imposed by the thermodynamic nature of the RWGS reaction. It is important to note that pressure as another operating factor, has negligible effect on catalyst behaviour up to 950 bar [23]. Therefore, RWGS mainly occurs under atmospheric pressure and high temperatures (> 800°C). Everything considered, it is important to improve the production of CO through RWGS reaction by the help of efficient catalytic systems operating at optimized conditions.

It is noticeable that the equilibrium conversion values of the RWGS reaction are low. For example, only 39% of CO_2 conversion can take place with $H_2/CO_2=1$ at 600°C and this value increases to 65% with $H_2/CO_2=3$ at the same temperature [24]. Therefore, elevating the concentration of H_2 is advantageous to CO_2 utilization since it promotes CO_2 consumption and at the same time assures the formation of synthetic gas (CO/H_2). However, increasing the H_2/CO_2 ratio can considerably alter the selectivity of the RWGS reaction. In other words, RWGS is not the only reaction that needs to be taken into account when using CO_2 and H_2 as reactants. The methanol synthesis reaction (Eq. 1.2) and the Sabatier reaction (Eq. 1.3) are two main reactions that can accompany RWGS reaction [25]. The three main direct CO_2 hydrogenation reactions are shown below:

$H_2+CO_2 \leftrightarrow CO+H_2O$ (RWGS reaction) $\Delta H^0_{298} = +41.3$ kJ.mol^{-1} (Eq. 1.1)
$3H_2+CO_2 \rightarrow CH_3OH+H_2O$ (Methanol synthesis) $\Delta H^0_{298} = -167$ kJ.mol^{-1} (Eq. 1.2)
$4H_2+CO_2 \rightarrow CH_4+2H_2O$ (Sabatier reaction) $\Delta H^0_{298} = -49.5$ kJ.mol^{-1} (Eq. 1.3)

According to thermodynamic considerations, methane is the second main component that can be formed together with CO. Thus, it is important to promote the RWGS reaction using catalytic systems that have high selectivity for CO formation. The RWGS reaction consumes the least amount of H_2 compared to other direct CO_2 hydrogenation reactions. Moreover, it benefits from several advantages such as facile operation, reusability of catalysts, simple reactor design and above all, easy separation of produced chemicals. Furthermore, low H_2 consumption as well as utilization of CO_2 as a low carbon source has made RWGS interesting.

Nevertheless, RWGS reaction is yet challenging because it requires high thermal energy. A commercially favourable RWGS reaction requires a renewable source of energy for providing both heat and hydrogen. Therefore, RWGS is not still feasible on the market on a large scale due to the problems associated with energy supply. The role of catalysts is crucial to facilitate higher reaction yield at lower temperatures. The German Ministry of Research and Education (BMBF) currently funds the commercial RWGS reaction, where H_2 is provided by the thermal decomposition of methane [26].

1.3 Research Objective:

The development of efficient catalytic systems is essential in order to enhance the conversion of CO_2 to CO through the RWGS reaction. Catalytic activity, stability and selectivity should be taken into consideration in order to develop effective catalysts. Throughout this study, metal nanoparticles including copper (Cu), iron (Fe), platinum (Pt) and ruthenium (Ru) as well as conductive and non-conductive metal oxides were studied as catalytic systems for RWGS reaction. Thus, four objectives were pursued:

Objective I: Synthesis and characterization of mono- and bi-metallic nanoparticles of the abovementioned metals

Objective II: Investigation of the catalytic performance of three different types of commercial metal oxides (ionically conductive, mixed ionic-electronic and non-conductive) in RWGS reaction for further use as catalytic support

Objective III: Investigation of the catalytic performance of non-noble metal nanoparticles including Cu, Fe and CuFe supported on active metal oxides for RWGS reaction

Objective IV: Investigation of the catalytic performance of noble metal nanoparticles including Ru, Pt, RuPt, RuFe supported on active metal oxides for RWGS reaction

This thesis is composed of 8 chapters. Chapters 1 and 2 outline the motivation for this thesis as well as a detailed literature review related to the research and above all, recent advances in catalytic systems for RWGS reaction. Chapters 3 and 4 specify the first objective of this research work, which is the synthesis and consequently the characterization of mono-metallic nanoparticles (Cu, Fe, Ru and Pt) and bi-metallic nanoparticles (CuFe, RuFe and RuPt) (Objective I).

Chapter 5 describes the performance of commercial metal oxides in terms of activity, stability and selectivity. Three different kinds of metal oxides (ionically conductive, mixed ionic-electronic and non-conductive) were evaluated in order to investigate the effect of ionic and electronic conductivity on RWGS reaction (Objective II). These conductive metal oxides are subsequently used in chapters 6 and 7 as catalyst supports for the deposition of mono- and bi-metallic nanoparticles.

Chapter 6 presents the catalytic behaviour of supported non-noble metal (Cu, Fe, and CuFe) catalysts (Objective III). Chapter 7 compares the catalytic performance of noble metal nanoparticles including Pt, Ru and RuPt supported on various conductive oxide supports (Objective IV). Furthermore, it intends to investigate the promoting effect of Fe with respect to supported RuFe catalysts (Objective IV). Finally, chapter 8 summarizes the conclusion of findings within this research and presents recommendations for future works.

Chapter 2: Literature Review

2.1 Introduction

A large amount of CO_2 is produced every year because of the burning of fossil fuels, which can be turned back into fuel and value-added chemicals using several CO_2 utilization techniques. In other words, CO_2 utilization brings many economical and environmental benefits. The Reverse Water Gas Shift (RWGS) reaction is one of the important CO_2 utilization methods, which results in the production of reactive carbon monoxide. CO is a valuable chemical that can be used for a range of industrial applications such as the production of synthetic fuel as well as the Fischer-Tropsch process to produce hydrocarbons and alcohols. RWGS reaction can be economically favourable if using a renewable source of energy and also using H_2 from water electrolysis. This could result in the sustainable production of synthetic fuel that can serve the annual energy demand in the transportation sector.

Beside a reliable energy supply, the RWGS reaction requires active, stable and selective catalysts in order to be used in industrial practices. Currently, the German Federal Ministry of Education and Research has put considerable money and effort into developing high-temperature electrolysers and consequently improving the Fischer-Tropsch process that is followed by the RWGS reaction [26]. However, more research is required in order to design efficient catalytic systems for the RWGS reaction for further commercialization.

This thesis studies several catalytic systems in order to enhance the overall conversion of CO_2 to CO through the equilibrium-limited RWGS reaction. It is essentially important to increase the reaction yield at lower temperatures since other direct hydrogenation reactions such as CO_2 methanation might occur. Therefore, the development of RWGS catalysts should be accompanied by studying other potential reactions that might decrease the yield of the reaction. Moreover, the equilibrium constant of the RWGS reaction is low at lower temperatures, e.g. 600°C and below, which gives rise to much lower reaction yields. Efficient metal catalysts and catalyst support should be identified and their properties needs to be optimized and further promoted in order to contribute to economizing the RWGS reaction.

2.2 RWGS Application and Advantage

Carbon dioxide mitigation requires the development of efficient CO_2 utilization techniques. RWGS is one of the best-known catalytic reactions to utilize carbon dioxide, Eq. 2.1:

$$CO_{2(g)} + H_{2(g)} \leftrightarrow CO_{(g)} + H_2O_{(g)} \qquad \Delta H^0_{298} = +\ 41.2\ \text{kJ mol}^{-1} \qquad \text{(Eq. 2.1)}$$

The RWGS reaction is thermodynamically and kinetically favored at high temperatures. However, renewable sources (wind or solar energies) can provide the high thermal input for RWGS reaction. Moreover, low-cost H_2 can be supplied by electrolyzing water using renewable energy sources. Therefore, CO can lead to the production of renewable synthetic gas (H_2+CO) [27]. Carbon monoxide can be hydrogenated according to the Fischer-Tropsch (FT) process to produce liquid hydrocarbons and alcohols. Therefore, synthetic gas can be transformed to liquids to be further refined into gasoline and other desirable products. Combination of RWGS and a consecutive FT process could lead to the production of gasoline, evaluated at 2 dollars per gallon; assuming 30 dollars tax is applied per ton of CO_2 emissions [28], which is lower than the current price of gasoline [29].

It is notable that steam methane reforming (SMR) and dry reforming of methane (DRM) are two important industrial reactions that also lead to the formation of CO, Eq. 2.2 and Eq. 2.3:

$$CH_4 + H_2O \leftrightarrow CO + 3H_2 \qquad \text{(SMR)} \qquad \Delta H^0_{298} = -206\ \text{kJ.mol}^{-1} \qquad \text{(Eq. 2.2)}$$

$$CO_2 + CH_4 \leftrightarrow 2CO + 2H_2 \qquad \text{(DRM)} \qquad \Delta H^0_{298} = -247\ \text{kJ.mol}^{-1} \qquad \text{(Eq. 2.3)}$$

The highly exothermic nature of these two reactions facilitates the formation of CO at lower temperatures compared to the RWGS reaction. However, CH_4 is one of the reactants of SMR and DRM reactions. CH_4 is the main component of natural gas that is considerably more expensive than CO_2. It is notable that CO_2 could be available at no cost or even with financial return using appropriate capture and recycling methods [30]. Therefore, RWGS could be considerably more cost-effective using a renewable source of energy. It has been reported that SMR and DRM consume more energy than they generate [31].

The RWGS reaction can be used for the production of methanol. It is important to note that methanol can be also formed through the direct hydrogenation of CO_2 (32), Eq. 2.4:

$$3H_2+CO_2 \rightarrow CH_3OH+H_2O \quad \text{(Methanol synthesis)} \quad \Delta H^0_{298} = -167 \ \text{kJ.mol}^{-1} \qquad \text{(Eq. 2.4)}$$

It is evident that the direct hydrogenation of CO_2 to methanol requires a large consumption of H_2, whereas the RWGS reaction (Eq. 2.1) demands much less H_2 to produce methanol. Thus, methanol can be formed at lower cost through the RWGS reaction following by CO hydrogenation using the CAMERE process [33]. Methanol can be further used as a feedstock to produce gasoline according to the Methanol to Gasoline (MTG) process, which can subsequently economize the transportation systems [34].

The RWGS reaction possesses several advantages compared to other direct CO_2 hydrogenation reactions, namely methanol synthesis and CO_2 methanation. Considerable hydrogen demand is the first drawback that makes other direct CO_2 hydrogenation reactions less interesting. The CO_2 methanation reaction or Sabatier reaction happens according to the Equation 2.5:

$$4H_2+CO_2 \rightarrow CH_4+2H_2O \quad \text{(Sabatier reaction)} \quad \Delta H^0_{298} = -49.5 \ \text{kJ.mol}^{-1} \qquad \text{(Eq. 2.5)}$$

Although less energy input is required for higher product yield through the Sabatier reaction and methanol synthesis due to their exothermic nature, they face remarkable kinetic obstacle due to the full reduction of CO_2 as opposed to the RWGS reaction. It is noticeable that the reduction of CO_2 to CO only requires the transfer of two electrons (C^{4+} to C^{2+}), while 8 electrons need to be transferred for its full reduction. Therefore less kinetic limitation is expected in the case of RWGS reaction. Moreover, it is evident that the CO_2 methanation reaction results in the production of more amounts of water, which could have an inhibitory effect on the catalyst efficacy and the subsequent reaction yield [35]. Therefore, catalyst deactivation could be accelerated through the CO_2 methanation reaction. In addition, the production of liquid hydrocarbon fuels is more attractive due to nowadays' growing energy issues compared to methane production.

2.3 Hydrogenation of CO_2

Carbon dioxide as an abundant and easily available carbon source can be hydrogenated to produce value-added products such as several chemicals and liquid fuels [24]. In spite of the stable nature of CO_2, thermodynamic pathways make it possible to activate CO_2 through its reduction or reaction with other chemicals. Methanol, synthesis fuel, dimethyl ether, methane and CO and etc. are among the products obtained through reducing CO_2 with hydrogen. Combustion engines can be fuelled by these materials and more importantly, their storage and transportation is facile [36].

Both photo-catalytic and electro-catalytic processes for CO_2 hydrogenation have been investigated expansively, however when it comes to producing higher value-added products, all these techniques fall short to different extents. Moreover, CO_2 can be thermo-chemically activated through which heavier hydrocarbons can be produced [37].

Hydrogen as a high-energy source acts as a reducing agent for CO_2 activation. However, considering the currently high price of hydrogen and issues associated with its storage and transportation, other reliable sources need to be generated. Water splitting through electrolysis has been proposed as a promising approach to achieve this possible.

It is noticeable that CO_2 activation routes fall into three major categories: direct hydrogenation, methanol-mediated and non-methanol methods [38]. Indirect routes might have several steps and can be carried out within different reactors. The RWGS reaction is regarded as an indirect approach for hydrocarbon synthesis, while the Fischer-Tropsch process is a direct approach. Fischer-Trospch reaction can be regarded as a modification of CO_2 transformation to lighter saturated hydrocarbons by the use of tailored metal catalysts. The products can be further used in petroleum industry as feedstock [39].

It is important to investigate the rate of the reaction between H_2, CO_2 and CO and their mixture in CO_2 hydrogenation reactions. It has been reported that CO and CO_2 hydrogenation reactions follow different pathway. Moreover, methane is the dominant product in CO_2 hydrogenation (over 70%) while low yield of methane is low (below10%) in the hydrogenation of CO [40]. However, depending on the catalytic systems, similar product yield can be obtained through both reactions. Iron and copper on alumina have been reported to be active catalysts for both CO and CO_2 catalysts [41]. Generally acknowledged, although more water vapour is produced through CO_2 hydrogenation, but the rate of catalyst deactivation is faster when CO is fed instead [31]. This suggests that the rate of CO_2 conversion is higher than the rate of CO conversion in hydrogenation reactions. Considering merely CO_2 and H_2 as the feedstock, the RWGS reaction as well as the Sabatier reaction and the methanol synthesis are potential routes through which the reaction can proceed.

2.3.1 Methanation of CO_2

The CO_2 methanation reaction can also be used to mitigate CO_2 and CO levels through converting them to methane. A large portion of natural gas is composed of methane (CH_4). CH_4 is widely used in power plants to produce heat and energy. The large-scale production of methane via CO_2 hydrogenation is known as the Sabatier reaction [42]. Carbon dioxide needs to be fully reduced in order to produce CH_4. Beside high H_2 consumption, considerable amount of heat will be produced because of the exothermic nature of the Sabatier reaction (Eq. 2.5). Heat removal techniques should be considered to resolve this issue. This also implies that the increase in the temperature can suppress the production of methane to the point that only little CH_4 yield is observed above 600°C. Although high H_2 concentrations noticeably favour the CH_4 formation, temperature is a more decisive factor as to which product forms [43]. Therefore, it is suggested that beyond 600°C, RWGS acts as the dominant reaction. All in all, high H_2/CO_2 ratios increase overall CO_2 conversion and at the same time increase CH_4 yield, while high temperatures considerably enhance the CO yield.

Catalytic methanation of CO_2 has been conducted over various metals especially those of groups 8-10 [42]. Among these, nickel-based catalysts proved themselves as the most active catalytic systems for systems for methane production. The low price of Ni and its high activity makes it highly of interest in the CO_2 methanation reaction; however, metal sintering is a dominant phenomenon, which leads to low stability [44]. Ruthenium is another active catalyst towards the formation of CH_4 [45]. However, it has been reported that the methanation activity of Ru and Ni is mainly dependent on metal-support interaction. Titania (TiO_2) is reported to be an effective support for Ni and Ru in the CO_2 methanation reaction [46]. Alumina also proved as an efficient support for Ru and Ni in the production of methane [47].

2.3.2 CO_2 Hydrogenation to Methanol

Carbon monoxide hydrogenation was regarded as the main route for the catalytic production of methanol until Chinchen et al. found that CO_2 is a far better alternative to be hydrogenated for this purpose [48]. CO_2 can be directly hydrogenated to methanol using the Equation 2.4. It also can be formed through indirect CO_2 hydrogenation reaction. CAMERE process is the commercial-scale route of methanol production that takes place in two different stages [32]. Therefore, the reactants first go through the RWGS reaction using $ZnAl_2O_4$-based catalysts, then the products of the first step will be fed into another reactor to produce methanol over Cu-ZnO based catalysts [49]. Methanol synthesis is a technique for CO_2 mitigation. It has also wide-ranging applications such as in direct methanol fuel cells.

A major problem in CO_2 hydrogenation to methanol is the low selectivity of the catalytic systems to form methanol [50]. This is because of the presence of other potential concomitant reactions such as CH_4 formation, which is thermodynamically more favourable as well as the RWGS reaction that is kinetically more suitable. It is noticeable that higher pressures and lower temperatures favour the formation of methanol. In view of thermodynamics, RWGS is the dominant reaction at higher temperatures and moreover, it does not require high pressures for improved reaction yields.

Notably, industrial catalysts for methanol formation are similar to that of RWGS reaction [32]. Copper-based catalysts are desirable for industrial practices in terms of catalytic activity and selectivity for the formation of methanol. Copper/ZnO-based catalysts have proved to be of high catalytic performance towards both RWGS and methanol production [51] [52] [48]. A kinetic study by Saito et al. over Cu/ZnO-based systems proved that both methanol and CO could be formed through similar pathways. At low CO_2 conversion, methanol and CO are two dominant components that are likely to be formed simultaneously. The formate mechanism is thought as the dominant pathway for CH_3OH formation [53].

2.3.3 The Fischer-Tropsch Synthesis

The fischer-Tropsch (FT) is an indirect CO_2 hydrogenation reaction that can lead to the production of several valuable chemicals and fuels depending on the catalyst used as well as the reaction conditions such as temperature and pressure [54]. For example, at moderate temperatures and at pressures lower than 100 bar, methane production is favored compared to higher hydrocarbons [55].

Throughout this process linear paraffin and α olefins can be formed according to the Equations 2.6 and 2.7 [56], respectively:

$$(2n+1)H_2+nCO \rightarrow C_nH_{(2n+2)}+nH_2O \qquad \text{(Eq. 2.6)}$$

$$2nH_2+nCO \rightarrow C_nH_{2n}+nH_2O \qquad \text{(Eq. 2.7)}$$

It is notable that although high products yield is an aim to achieve, but it is accompanied by higher water formation, which has an inhibitory effect on the catalyst activity. Introduction of oxygen into the by-products of the FT process can result in the formation of various organic compounds such as ketones, aldehydes and alcohols according to the Equation 2.8:

$$2nH_2+nCO \rightarrow C_nH_{(2n+2)}O+(n-1)H_2O \qquad \text{(Eq. 2.8)}$$

The Fischer-Tropsch reaction can be carried out in high and low temperature modes. Low temperature FT process is better suited for the formation of high molecular weight products along with the constituents of diesel. High temperature FT occurs at above 300 °C through which lighter hydrocarbons can be obtained [57]. Due to the currently high consumption of fossil fuels and the limited petroleum-based supplies, the main research on FT process is devoted to produce fuels. In view of viability, FT process currently more effective than other non-fossil fuel based sources if the oil price exceeds $30 USD/barrel ($48/Barrel is the price at time of writing) [58].

Metals such as iron, nickel, cobalt, palladium and platinum have proved to be active metals in the FT process [59][60]. It is notable that the catalytic support plays a crucial role on the FT activity of the abovementioned metals. Vannice et al. reported that alumina affects the metal activity as per the order: Ru > Fe > Co > Pd > Pt, which is in accordance with the order of the molecular weight of the formed products [61]. This illustrates the important role of the catalyst on product distribution. Therefore, the performance of a FT catalyst depends not only on its activity, but also appropriate product distribution. Ruthenium, for example, offers the best catalytic performance and product distribution because it facilitates the formation of higher hydrocarbons at high pressures (>1000bar) and low temperatures (<100°C) [62]. However, Ru is approximately 31,000 times more expensive than iron [63]. Despite the good catalytic activity of iron in the FT process, high amounts of water can result in its oxidation to magnetite (Fe_3O_4) and therefore make iron inactive for FT process. Magnetite has been reported as the most active phase of iron in the RWGS reaction [64].

Table 2.1: Relative metal prices [63]

Metal	Price Ratio
Iron	1
Cobalt	230
Nickel	250
Ruthenium	31,000
Platinum	682,000

2.4 Mechanisms of the RWGS Reaction

Many studies have been undertaken on the design and development of catalytic systems in the RWGS reaction; however, the mechanism of this reaction is yet controversial. Nevertheless, many corroborate the existence of two potential mechanisms, namely the redox mechanism and the formate decomposition mechanism.

According to the redox mechanism, CO_2 and H_2 would dissociatively adsorb on the surface of the catalyst and subsequently surface CO, H and surface oxygen species would be formed. Further desorption of carbon monoxide and H_2O leads to the formation of the products. This mechanism occurs according to the following scheme:

$$CO_{2(g)} \rightleftharpoons CO_a + O_a$$
$$CO_a \rightleftharpoons CO_{(g)}$$
$$H_{2(g)} \rightleftharpoons 2H_a$$
$$H_a + O_a \rightleftharpoons OH_a$$
$$H_a + OH_a \rightarrow H_2O_a$$
$$H_2O_a \rightleftharpoons H_2O_{(g)}$$

The redox mechanism for the RWGS reaction [65]

The redox mechanism suggests alternate oxidation and reduction of the surface sites through which oxygen adatoms (O_a) would appear on the surface of the catalyst. Hence, this route can be also regarded as "oxygen adatom mechanism".

Another important mechanism of the RWGS reaction is the formate mechanism, which can be modeled using the following scheme:

$$H_{2(g)} \rightleftharpoons 2H_a$$
$$CO_{2(g)} + H_a \rightleftharpoons HCOO_a$$
$$HCOO_a \rightleftharpoons CO_a + OH_a$$
$$OH_a + H_a \rightleftharpoons H_2O_a$$
$$H_2O_a \rightleftharpoons H_2O_{(g)}$$

The formate decomposition mechanism for the RWGS reaction [66]

Some studies revealed that there is a correlation between the concentration of formate intermediate and the rate of carbon monoxide formation. Thus, it is thought that formate affects CO production. In addition, the mechanism of formate decomposition cannot be investigated using redox-based kinetics [66]. Therefore formate mechanism is believed to be the dominant route for the reactions that do not study the redox ability of the catalytic systems.

Many efforts were put into explaining the shortcomings of these two mechanisms, which resulted in assuming that these two might occur simultaneously. However, there is not ample evidence to corroborate this statement [67].

Although redox and formate decomposition have been extensively studied among all the possible mechanisms, there is another potential route through which carbonate species follow the same pathway as formate decomposition mechanism. This mechanism is regarded as dissociative mechanism, which can be illustrated according to the following model:

$$2OH^{-}_{a} \rightleftharpoons H_2O_{(g)} + O^{2-}_{a}$$

$$CO_{2(g)} + O^{2-}_{a} \rightleftharpoons CO_3{}^{2-}_{a}$$

$$CO_3{}^{2-}_{a} + H_{2(g)} \rightleftharpoons CO_a + 2OH^{-}_{a}$$

$$H_{2(g)} \rightleftharpoons 2H_a$$

$$2H_a + O_a \rightleftharpoons H_2O_a$$

The associative/carbonate mechanism for RWGS reaction [68]

In the case of carbonate mechanism for RWGS reaction, it is proposed that surface oxygen can react with CO_2 and form carbonate. Goguet et al. investigated this mechanism on a Pt/CeO_2 system and suggested that the formation of carbonate determines the rate of the RWGS reaction [69].

2.5 Different Factors Affecting CO_2 Conversion in RWGS

2.5.1 Catalyst

Although the thermodynamic natures of the forward and the reverse shift reactions are different, studies proved that catalysts active for the forward shift reaction, usually exhibit good activity for the reverse shift reaction. This proved to apply to a majority of catalysts active for the forward Water Gas Shift reaction [70]. As a result, Water Gas Shift (WGS) active catalytic systems have been expansively studied under the RWGS reaction conditions. Low equilibrium conversions especially at moderate temperatures (200-600°C) makes catalysts an integral part of the RWGS reaction. It has been reported that there is a negligible homogenous contribution to CO_2 conversion in the RWGS reaction below 800°C [71]. However, the product yield is noticeably increased in the gas phase in the temperature range of 875-1050°C without the help of any catalytic systems in RWGS reaction. Tingey et al. reported that the homogenous RWGS reaction mainly occurs above 800°C and it proceeds through another reaction route, namely chain-reaction mechanism [72].

Copper-based catalysts such as Cu/ZnO are regarded as industrial RWGS catalysts [73]. Moreover, Fe-based catalysts supported on SiO_2 and V_2O_5 showed very promising results in commercial applications of the RWGS reaction [50] [74]. However, Cu- and Fe-based RWGS catalysts are required to be stabilized in terms of structural and thermal stability. Incorporation of alkaline metals such as K, Mg, Na and Ca has been frequently reported to promote Cu and Fe metals in RWGS reaction [75]. Conventional shift catalysts including iron, cobalt, copper and nickel have been studied extensively using different catalytic supports in the RWGS reaction. Ni/CeO_2, for example, showed improved RWGS activity and CO selectivity, while Ni/Al_2O_3 had a considerably high CH_4 selectivity. Therefore, RWGS catalytic systems are studied with respect to the interaction between the metal and the support. Moreover, noble metals including Pt, Pd, Ru and etc. were also used extensively studied in RWGS catalysis due to their high catalytic activity . However, it is noticeable that the RWGS activity of these metals is mainly dependent on the catalyst support. Reducible catalyst supports such as TiO_2 and CeO_2 play leading roles in promoting the RWGS activity of these metals [76] [77].

2.5.2 Reactant Composition

Investigation into the RWGS reaction as well as other CO_2 hydrogenation reactions, namely CO_2 methanation and methanol synthesis, gives rise to the fact that H_2 concentration plays a crucial role in determining the final product yield. It is generally believed that increasing H_2/CO_2 ratio increases the CO_2 conversion, however it considerably impacts the reaction yield and mechanism [18]. Increasing the H_2 feed concentration is considered as one of the approaches to boost CO production at higher temperatures (500°C and higher). This has been used over Cu/SiO_2 in commercial RWGS applications [66]. Nevertheless, high H_2 concentrations noticeably result in lower CO yield at lower temperatures. Many studies proved that $H_2/CO_2=1$ is a suitable reactant composition in the RWGS reaction [78]. The CO_2 methanation reaction is the main potential hydrogenation reaction that can accompany the

RWGS reaction. Figure 2.1 clearly shows the effect of the reactant composition on CO_2 conversion and CH_4 selectivity over Cu/SiO_2 in the RWGS reaction.

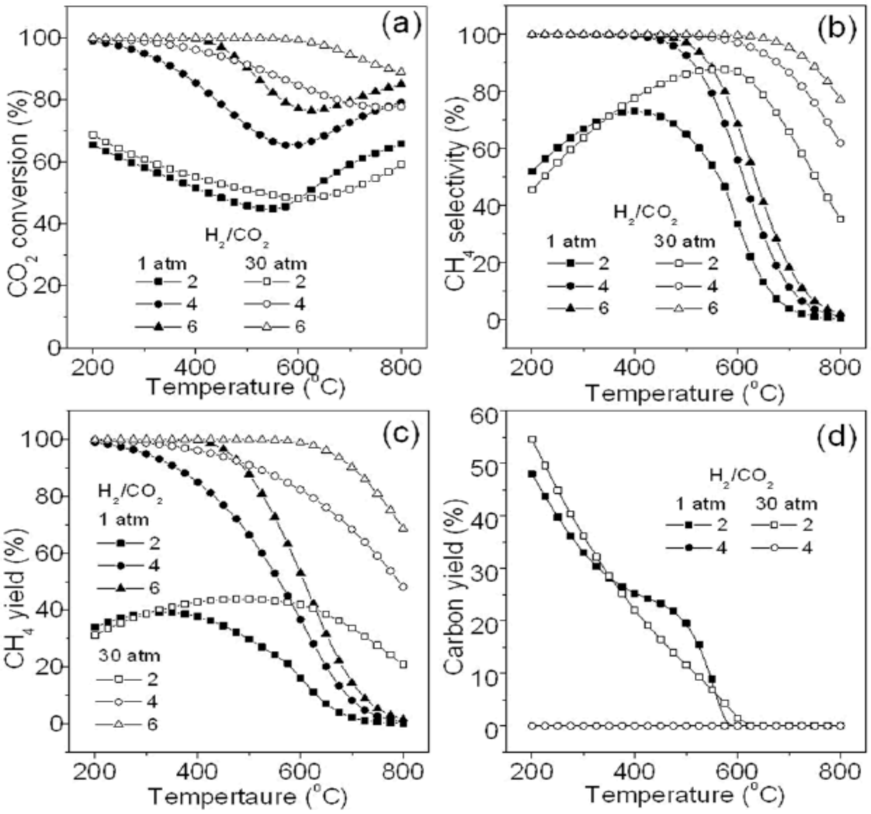

Fig. 2.1: CO_2 conversion and CH_4 selectivity at varying H_2/CO_2 ratios and pressures over Cu/SiO_2 [43]

In order to increase the catalyst activity in RWGS reaction, an ideal operating condition such as low H_2/CO_2 ratios from 1 to 2 is required. High temperatures and appropriate H_2/CO_2 ratio is essential for high CO yield. It should be noted that increasing the feed concentration could also result in heat and mass transfer limitations, which would further lower the reaction yield [79].

2.5.3 Effect of Temperature and Pressure

The endothermic nature of the RWGS reaction requires high thermal input in order to elevate CO formation. The equilibrium constant (K_{eq}) is remarkably low at moderate temperatures (<500°C) and it increases at higher temperatures. Figure 2.2 shows the equilibrium constant as a function of temperature at atmospheric pressure and indicates the low equilibrium constant at $H_2/CO_2=1$ in the RWGS reaction.

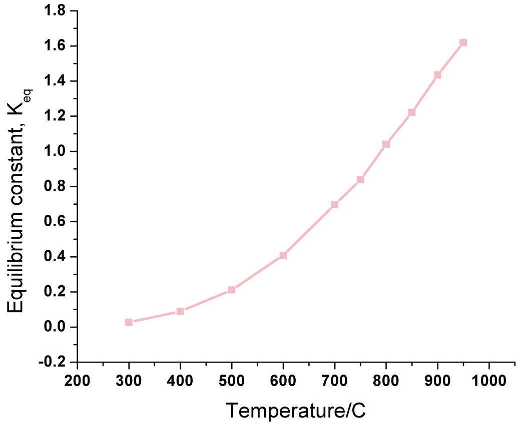

Fig 2.2: Equilibrium constant as a function of temperature in the RWGS reaction. Calculations are done using Aspen HYSYS for RWGS reaction at $H_2/CO_2=1$ and P= 1atm

It has been later discussed in this chapter that temperature considerably affects the reaction yield in CO_2 hydrogenation reactions. In general, lower temperatures (500°C and below) favour the formation of undesirable products such as methane and methanol in the RWGS reaction [74].

Considering the reaction pressure, improved RWGS catalytic performance has been reported at pressures ranging from 1- 30 atm. [18]. However, the pressure of 1 atm proved to be effective for promoting the RWGS reaction and most of the studies on RWGS have been carried out under atmospheric pressure [80]. An explanation for the efficacy of the RWGS reaction at atmospheric pressure could be related to the reactants composition, which is mostly used as $H_2/CO_2=1$. This implies that the total number of moles introduced into the

RWGS reactor is equivalent to those produced. Therefore, pressure is not an influential factor in promoting RWGS reaction.

2.5.4 Kinetics and Residence Time

In order to investigate the best operating conditions for increasing CO_2 conversion to CO in RWGS reaction, the main step is to determine the most favorable kinetic factors. In other words, the reaction needs to be kinetically monitored throughout the RWGS reaction. This necessitates selecting a suitable synthetic approach for smaller catalyst particle size as well as the best particle quantity and gas hourly space velocity (GHSV), to eliminate transfer and diffusion hindrances. According to the RWGS mechanisms, this reaction is fast-paced. This dictates that high residence time might result in lower CO yields. On the other hand, increasing the total feed flow rate leads to lowering the residence time and therefore reducing the reaction yield. It is significant to optimize the total gas flow rate and reactants residence time to achieve higher CO_2 conversion.

2.6 Catalysts for RWGS Reaction

2.6.1 Fe- and Cu-based Catalysts

Iron and copper catalysts have been extensively studied in the RWGS reaction. The reasonable price and good activity of Cu and Fe led to their commercialization in RWGS catalysis. In industrial RWGS reactions, Cu is mainly used in $Cu\text{-}ZnO\text{-}Cr_2O_3$, Cu, $Zn\text{-}Mn\text{-}Cr_2O_3$ and, most importantly $Cu\text{-}ZnO\text{-}Al_2O_3$ catalysts [81]. $Cu\text{-}ZnO\text{-}Al_2O_3$ is the main Cu-based commercial catalyst in RWGS reaction. However, it is essential for Cu and Fe catalysts to become stabilized in the RWGS reaction [69]. Cu has a low melting point (1083°C), which addresses the need for generating Cu-based samples of higher temperature tolerance to avoid sintering and subsequent deactivation [82]. Beside an effective stabilizer, many studies have been focused on proving the catalytic activity of Cu and Fe using appropriate catalyst supports. For example, Cu/CeO_2 systems proved to reach the equilibrium conversion in the RWGS reaction [83].

In the case of Cu catalysts, their RWGS activity has been found to be directly proportional to the surface area of Cu-based catalysts. Hence, stabilization of the copper surface area needs to be investigated either by the addition of stabilizers such as silica, chromia, zinc oxide [84] or metal dopants such Fe. Iron is regarded as the most effective metal dopant in stabilizing Cu catalysts. It is notable that Fe by itself has higher thermal stability as opposed to Cu. One of the very interesting features of Cu is its considerably high selectivity towards CO, rather than CH_4 [85]. Therefore, developing size-controlled Cu nanoparticles as well as use of appropriate promoters allows for effective cu-based systems in RWGS reaction [86][87]. Studies proved that Fe is a good dopant for the stabilization of Cu systems. Figure 2.3 shows the promoting effect of Fe in stabilizing Cu/SiO_2 catalysts in RWGS reaction [66].

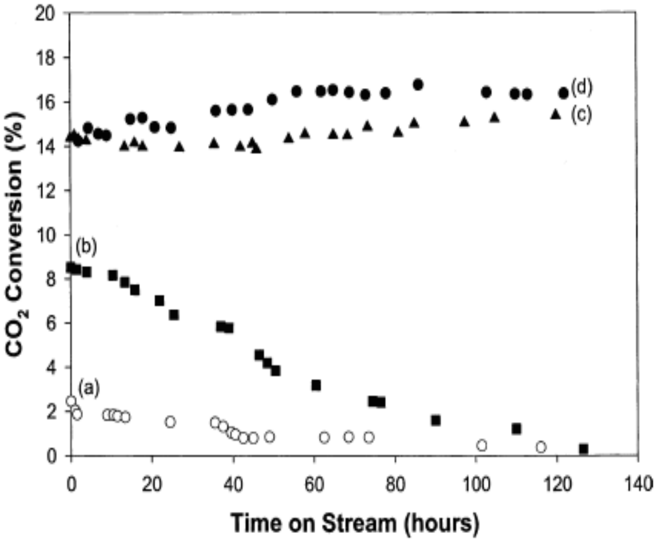

Fig 2.3: Time-on-stream (TOS) behaviour of (a) 0.3% Fe/SiO_2, (b) 10% Cu/SiO_2, (c) Cu-Fe/SiO_2 (Cu/Fe= 10:0.3), and (d) Cu-Fe/SiO_2 (Cu/Fe = 10:0.8) at 600°C. $H_2/CO_2 = 1$, F = 100 mL.min^{-1} [66]

Fe-based RWGS catalysts also require to be stabilized, particularly in terms of structure. Addition of a stabilizer such as chromia (Cr_2O_3) is considered as an integral step of developing Fe-based RWGS catalysts. Incorporation of Cr^{+3} leads to the structural and textural stability of Fe and therefore prevents the metal sintering. Chromia is highly effective in stabilizing Fe and it led to the commercialization of Fe-Cr catalysts for RWGS reaction. However, its further oxidation, results in the formation of CrO_3 (Cr^{+6}) that has a carcinogenic nature. The development of Fe-based catalysts containing no Cr traces has been widely undertaken by using other effective alternatives including V_2O_5. [88] Mg, Mn, Co, Cu [89] and Ce, Ca, Zr and Al [90].

Moreover, it is of the greatest concern to identify the active phases of Fe in RWGS reaction. It has been reported that Fe by itself, exhibits no selectivity to RWGS reaction, whereas, it suitably catalyzes the hydrocarbon formation reactions including the CO_2 methanation and Fischer-Trospch (FT) process [91]. It is worth noting that not all iron oxide phases are active for WGS reaction [92]. Magnetite (Fe_3O_4) and hematite (Fe_2O_3) are considered as the most active phases of iron for catalyzing the shift reactions [93]. The high catalytic activity of Fe_3O_4 in RWGS is mainly attributed to its accessible oxidation states, which facilitates the charge transfer. Magnetite can be formed through the Partial reduction of hematite.

In industrial practice, Fe-based RWGS catalysts needs to be preceded by a pre-reduction reaction at 300-450°C according to Equations 2.9 and 2.10:

$$3Fe_2O_3 + H_2 \leftrightarrow 2Fe_3O_4 + H_2O \qquad \Delta H^0_{298}= -16.3\ kJ/mol, \qquad (Eq.\ 2.9)$$

$$3Fe_2O_3 + CO \leftrightarrow Fe_3O_4 + CO_2 \qquad \Delta H^0_{298}= +24.8\ kJ/mol \qquad (Eq.\ 2.10)$$

It is noticeable that the excessive reduction of Fe_3O_4 might form metallic iron and it should be prevented. This necessitates the demand for heat removal and introduction of appropriate amount of H_2 as the reducing agent. Therefore, introduction of high amounts of H_2 should be avoided in RWGS reaction over Fe-based catalysts. The highly exothermic reaction of Fe_3O_4 reduction to metallic Fe occurs as the following equation, Eq. 2.11:

$$Fe_3O_4 +4H_2 \leftrightarrow 3Fe+4H_2O \qquad \Delta H^0_{298}= -149.4\ kJ/mol \qquad (Eq.\ 2.11)$$

All things considered, Fe-based RWGS catalysis is particularly centered on developing magnetite nanoparticles. It has been reported that the synthesis of smaller Fe nanoparticles, e.g. sub-10 nm, leads to the formation of magnetite [42].

2.6.2 Platinum Group Metal (PGM) Catalysts

Renewed interest has been taken into studying RWGS reaction over platinum group metals. Platinum group metals (PGM) refer to the six precious transition metals including platinum (Pt), palladium (Pd), Gold (Au), rhodium (Rh), ruthenium (Ru), and osmium (Os).

Many studies have shown that the catalytic activity of PGMs in RWGS reaction is strongly dependent on the nature of the catalytic support and subsequently the metal-support interaction. Therefore, the catalytic activity of PGMs for RWGS reaction can noticeably vary depending on the type of the support. For example, the catalytic activity of PGMs supported on Fe_2O_3 is in order: Ru > Pt > Ir > Pd > Rh [91]. In another study, Tabakova et al. reported that activity of the supports changes in the order $Fe_2O_3 > ZrO_2 > ZnO$ as for Au nanoparticles in RWGS reaction [94]. In a comparative investigation, cerium oxide proved itself as a better support as opposed to alumina for Pt metals [95] [96]. It has been reported that Au dispersed on TiO_2, Fe_2O_3, ZrO_2 (94) (97), Pt over ZrO_2 [64] and Ru supported on Fe_2O_3 and La_2O_3 [23] show the best RWGS activity. CeO_2 showed promising results in the activity of all PGMs.

Numerous findings corroborate that the activity of PGMs can be remarkably enhanced by use of partially reducible oxide supports, namely ceria (CeO_2), iron III oxide (Fe_2O_3), titania (TiO_2) and zirconia (ZrO_2) [98]. Noble metal-based catalysts supported on reducible oxides are believed to be bi-functional catalysts because both the metal and the support cooperate and promote the RWGS reaction [99] [100]. Therefore, the metal-support interaction is a major factor in the catalytic performance of noble metal-based catalysts in RWGS reaction. A comprehensive study by Thinon et al. on different metals supported on reducible oxides is shown in Table 2.2, which outlines the effect of metal-support interaction as well as the metal loading on the RWGS activity of catalysts.

Table 2.2: Activation energies and catalytic activities (at 300°C) of Pt, Au and Cu based catalysts in RWGS reaction [101]

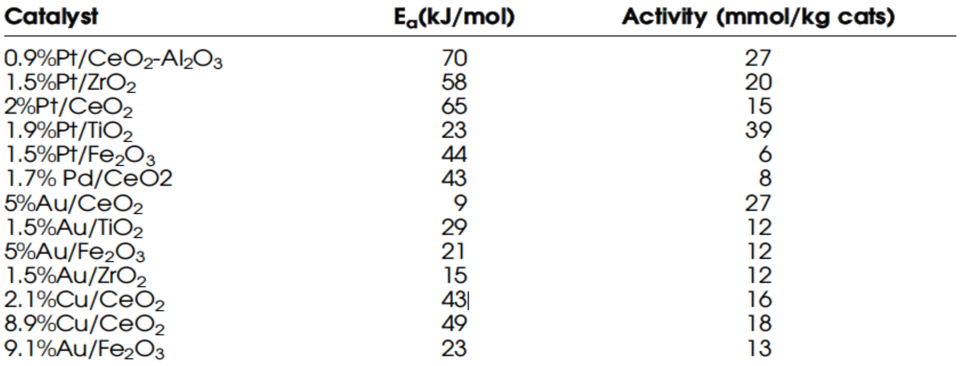

Catalyst	E_a(kJ/mol)	Activity (mmol/kg cats)
0.9%Pt/CeO_2-Al_2O_3	70	27
1.5%Pt/ZrO_2	58	20
2%Pt/CeO_2	65	15
1.9%Pt/TiO_2	23	39
1.5%Pt/Fe_2O_3	44	6
1.7% Pd/CeO2	43	8
5%Au/CeO_2	9	27
1.5%Au/TiO_2	29	12
5%Au/Fe_2O_3	21	12
1.5%Au/ZrO_2	15	12
2.1%Cu/CeO_2	43	16
8.9%Cu/CeO_2	49	18
9.1%Au/Fe_2O_3	23	13

Ruthenium-based catalysts also show promising activity in RWGS reaction. However, it is very important to note that Ru is highly selective towards CH_4 production [102]. Therefore, it is crucial to identify effective catalytic supports to enhance the performance of Ru towards RWGS reaction. Many studies focus on developing active Ru-based systems in RWGS reaction. Holladay et al. claimed that Ru showed high RWGS activity, reaching 97% of equilibrium conversion at 800°C, using ZrO_2-CeO_2 as the support [103]. In another attempt, Ru/V_2O_3 showed high activity in RWGS reaction [104]. Further enhancement of the catalytic activity of noble metals can be achieved through synthesizing bi-metallic systems. Pt-Ru alloys have been used to catalyze hydrocarbon oxidation and reforming for H_2 production as well as water splitting [105]. They also showed good results in RWGS reaction. Wenqian et al. reported a considerable reduction in CH_4 selectivity of Ru with respect to the Ru-Pt/CeO_2 catalyst [102].

Nonetheless, the high cost of PGMs has ruled out their application in RWGS industrial practices. As a result, PGMs have gained more attention in compact catalyst beds such as automotive convertors and especially in fuel cell applications. The catalysts applied in fuel cells need to be non-incendiary, durable in rapid heating and cooling cycles and free of pre-treatment processes such as pre-reduction. PGMs own all these characteristics. However, decreasing the metal content and further improvement of the catalytic activity are two main factors to be considered regarding precious metals.

2.7 Synthesis of Nano Catalysts

Wet impregnation method is one of the most widely used and acceptable catalyst synthesis approaches [106]. This method comprises dissolving the powder in a solution of the metal salt, followed by drying and calcination. Although this approach is regarded as a facile route but it exhibits some disadvantages, which encourage the development of other synthesis techniques [107]. An example of a major disadvantage is the processing medium that is an aqueous solution, which gives rise to metal aggregation. This indeed restricts the control over particle size and distribution that is not desirable in terms of catalytic activity and stability [108]. Moreover, some catalyst supports can lose their activity as a result of impregnation/calcination procedure. It is established that the calcination of ceria-supported metal catalysts results in little oxygen transfer from ceria to the metal because of their exposure to air at elevated temperatures. It is noticeable that oxygen mobility is one of the important catalytic features for some reactions such as oxidation-reduction reactions [109]. Surface "redox mechanism" is reported to be one of the main routes through which RWGS reaction proceeds [110] (see chapter 2, section 2.4). Therefore, the impregnation technique might lead to poor performance of catalytic systems including ceria-based catalysts [111].

The Polyol synthesis method is another technique for the synthesis of nano-sized metals that proved to be effective for many catalytic systems [112]. For example, it is a very efficient technique for the production of metal catalysts that are susceptible to O_2 treatment, because exposure to O_2 would result in their surface segregation [113]. The method involves using a polyol (e.g. ethylene glycol, triethylene glycol and etc.) as a solvent, which acts as a stabilizer as well as a reducing agent and it can be easily removed at low temperatures (160°C) [114].

2.7.1 Polyol Synthesis Method

The polyol method is a liquid-phase synthesis that leads to the formation of nanoparticles. Varied range of polyols including ethylene glycol (EG) to longer chain polyols, e.g., triethylene glycol (TrEG), tetraethylene glycol (TEG), and so forth up to polyethylene glycol (PEG) can be used in this technique. Polyols are water-comparable media that have higher boiling point compared to water and are capable of reducing metal salts and stabilizing their resultant nanoparticles. Thus, they can provide synthesis temperatures as high as 320°C [115]. EG, for example, is a powerful reducing agent that has a boiling point of approximately 197°C that has been used extensively in polyol reduction synthesis. Therefore, polyol method is an adaptable and flexible synthesis approach.

Polyol synthesis method offers several advantages and is known as an optimum method for the formation of noble metal-based nanoparticles [116]. For example, the polyol method proved to be a suitable technique for the synthesis of size-controlled Ru and Pt colloids (0.7 – 4 nm), using ethylene glycol as the solvent [117]. It has been reported that the use of high temperatures could result in surface segregation in Ru and particularly Pt nanoparticles [37]. However, polyol method can facilitate the formation of Ru- and Pt-based nanoparticles at low temperatures (160°C) [117]. Moreover, it is reported that polyol-synthesized nanoparticles are very suitable for direct deposition on catalyst supports, compared to other nanoparticle synthesis methods [118].

Nevertheless, this method has some shortcomings in the formation of size-controlled nanoparticles of non-noble metals. For instance, it has been reported that EG is reductive enough for the synthesis of size- and shape-controlled nanoparticles of noble metal [119], while its reducing power is not enough for the formation of Fe-based nanoparticles, namely magnetite (Fe_3O_4) [120]. In other words, the formation of Fe_3O_4 nanoparticles requires higher synthesis temperatures (> 200°C) and hence, polyols with higher boiling point, e.g., triethylene glycol facilitate their formation. It is important to note that he reduction potential of the longer chain polyols is remarkably higher as a result of suitable synthesis temperatures as well as their coordinative features [115]. The need for more reductive solvents is mainly attributed to the highly electropositive nature of the Fe^{II} and Fe^{III} [121]. It has been reported that EG mainly supports the formation of elemental iron [122]. It is noticeable that Fe_3O_4 is the most active phase of iron oxide for the RWGS reaction, whereas metallic iron promotes the CO_2 methanation reaction [64].

2.8 Catalyst Supports for RWGS Reaction

Catalytic supports are one of the principle components in heterogeneous catalysis. Stabilization of metal active sites and subsequently the prevention of sintering is the primary role of the supports that comes into play especially at elevated temperatures [123]. Although catalyst supports, e.g. alumina (Al_2O_3), carbon (C), titania (TiO_2) and ceria (CeO_2), are mainly used as substrates for metal deposition, they may exhibit several properties that could lead to the improved catalytic performance in the RWGS reaction. For example, support's reducibility [76] [124], ion or electron conductivity [125] [126], oxygen mobility [127] [128] and surface area [129] can greatly determine the overall catalyst performance.

In the early 1970s, the possibility of using catalytic supports as conductors was suggested [130]. This idea was mainly based on some observations such as the conductivity of yttria-stabilized Zirconia (YSZ) due to an applied potential. Further investigations have confirmed the existence of ion conductivity in the absence of applied current. On the other hand, it was found that the conductivity could be induced by thermal energy rather than electrical energy [131]. Ceria-based ceramics and titania, for example, exhibit the similar behaviour.

Reducible supports play an important role in the RWGS reaction [132]. The reducibility of the support can promote the reaction through the redox (oxidation-reduction) mechanism as a result of undergoing different oxidation and reduction cycles. CeO_2, for example, is considered as a reducible support that has shown good promoting effects on the catalytic activity of several metals including Cu, Pt [133]. Oxygen Storage Capacity (OSC) in oxide supports facilitates the storage and subsequent release of oxygen anions (O^{2-}). Addition of dopants can further induce higher oxygen vacancies to reducible supports [134]. Examples include samarium (Sm^{3+})-doped ceria and lanthanum (La)-doped ceria that have higher oxygen vacancies compared to ceria [95].

2.8.1 Metal-Support Interaction (MSI) Effects

It has been established that catalytic activity is mainly investigated through studying the metal and the support as a whole. Therefore, it is very significant to identify the interaction between the metal catalyst and the support. The main role of a catalyst support is to spread out the active sites. However, the support can have different chemical and electronic properties on its surface and at the interface of the active metals, which can lead to the promotion of the catalytic reactions.

The metal-support interaction can be affected by the nature of the support [135] [136], content of the metal [137] [138] and the catalyst synthesis method [139]. The nature of the support is considered as one of the most important factors in determining MSI. For example, it has been reported that the metal-support interaction is weak in the case of non-conductive supports, e.g., Al_2O_3, SiO_2, carbon and etc. However, many studies have shown a strong MSI for catalysts supported on reducible oxides, namely CeO_2, TiO_2, YSZ and etc. [140]. It has been observed that the deposition of PGMs, namely platinum, ruthenium, palladium and etc. on reducible and partially reducible supports can lead to a strong MSI [141].

Strong metal-support interaction can be attributed to the effect of the support on the electronic properties of the metal catalysts [142]. Electron exchange between the support and the metal can modify the catalytic performance through increasing the electron density on the metal. Oxide supports such as samarium-doped ceria (SDC), ceria (CeO_2) and titania (TiO_2) are considered as mixed ionic-electronic conductive (MIEC) materials. In a study conducted by Kim et al., the activity of Pt nanoparticles is noticeably higher over TiO_2 compared to Al_2O_3 in RWGS reaction. The enhanced catalytic performance of Pt/TiO_2 has been attributed to the charge transfer between the metal and the support, which results in a strong MSI [76].

2.8.2 Ionically-conductive Oxides

Ionic conductive metal oxide supports have received renewed attention in high temperature applications such as RWGS reaction in the past few decades [143] [144]. ceria (CeO_2), samarium (Sm^{3+})-doped ceria (SDC), yttria-stabilized zirconia (YSZ), titania (TiO_2) and iron III oxide (Fe_2O_3) pertain to this group of metal oxides [126] [145]. High temperature tolerance (1000°C and higher) of this type of oxides is another important factor that gives rise to their use in the RWGS reaction.

Ionic conductivity is believed to be dependent on the structure of the metal oxides, which facilitates ion transfer either through vacancies in crystal structure or through series of interstices [146]. Ionic conductivity is mainly attributed to the structural defects including the Frenkel disorder and the Schottky disorder [147]. Oxygen ion (O^{2-}) conductivity has a considerable promoting effect on RWGS reaction. It leads to the progress of the RWGS reaction, since it facilitates the oxidation-reduction cycles. It is noticeable that the redox mechanism is believed to be one of the main mechanisms in RWGS catalysis.

Doping can have a major promoting effect on the reducibility of conductive supports. As a result of doping, new energy levels within band gaps would be generated. As for ceria, the ionic conductivity is strongly dependent on the incorporation of rare earth dopants namely Sm, Gd, Dy, Nd and Er. Among these dopants, Sm^{3+} (10 mol% or higher) demonstrates higher conductivity [137]. It has been reported that Sm and Gd induce higher ionic conductivity to CeO_2, as opposed to Dy, Nd and Er. Ceria facilitates CO_2 adsorption and more importantly pure ceria exhibits no selectivity towards CO_2 methanation as confirmed by some studies [148].

Samarium (Sm^{3+})-doped ceria (SDC) has been extensively investigated in solid oxide fuel cells (SOFC). YSZ is also an ion conducting material, which has been used in SOFC as well as shift reactions [149]. It is notable that the ionic conductivity of ceria alone at 750°C compares with that of YSZ at 1000°C [27]. Therefore, SDC is expected to be more conductive as opposed to YSZ. It has been reported (Fig. 2.4) that the RWGS activity of Ni/SDC at 700°C is 10-15% higher compared to Ni/YSZ [150].

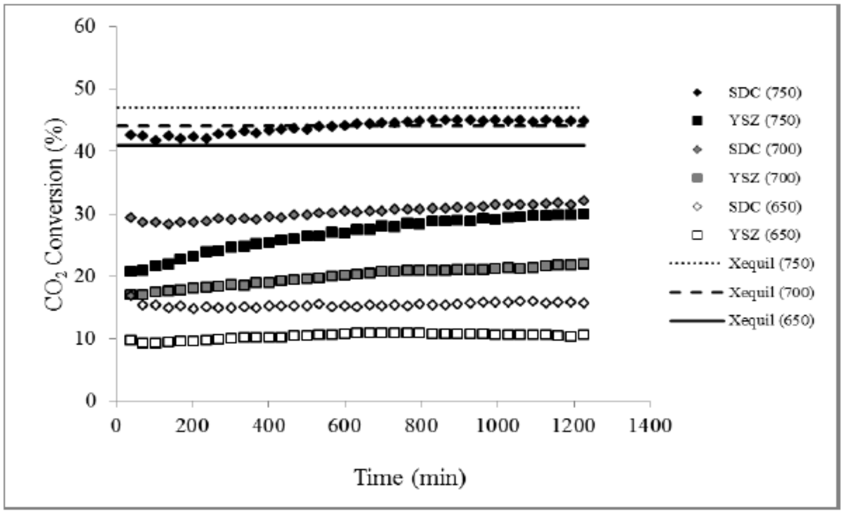

Fig. 2.4: CO_2 conversion in RWGS reaction over Ni supported on SDC and YSZ at varying temperatures, H_2/CO_2= 1, GHSV = $70 hr^{-1}$ [150]

2.8.2 Mixed Ionic-electronic Conductive Oxides

Mixed-conductive supports are materials wherein both O^{2-} and electron mobility can be observed. Electron conductivity is attributed to the delocalized domains in the valence band or localized domains in which electron exchange can be thermally induced [151]. It is noticeable that there is no correlation between the ion and the electron conductivity. Ion conductivity is mainly defined by the crystal structure, whereas electron conductivity depends on the electronic band gap [146]. For instance, YSZ shows little to no electronic conductivity in both oxidizing and reducing atmospheres, whereas it exhibits good ionic conduction [152].

Ceria-based ceramics and titania (TiO_2) are metal oxides demonstrating both ionic and electronic conductivity [153]. Electron hopping between $Ti^{+3}$and Ti^{+4} in titania and Ce^{3+} and Ce^{4+} in ceria account for electron conduction and facilitates the redox ability of these materials [154]. It has been reported that the energy required for defect formation is considerably low in nano-crystalline CeO_2-based ceramics, which accounts for higher electronic conductivity. Similar findings hold true for TiO_2 [155]. Numerous studies show that mixed-conducting oxides are effective catalytic supports in RWGS reaction due to generating new active sites [69].

2.8.3 Non-conductive Oxides

Many metal oxides do not demonstrate any conductivity. Examples include gamma-alumina (γ-Al_2O_3) [156]. It has been reported that γ-Al_2O_3 alone shows little to no activity towards RWGS reaction [157]. However, γ-Al_2O_3 as a catalyst support improves the metal dispersion and its subsequent stabilization as a result of its high surface area [158]. ZnO is another non-conductive oxide that has been used extensively in shift reactions. ZnO is a basic oxide that can be utilized to neutralize acidic species such as alumina and avoid the formation of dimethyl ether (DME) [83]. It has been found that these oxides might be non-conductive as a result of their grain boundaries. For example, the grain boundaries of ZnO are free of electrons and therefore it shows no electronic conduction [159]. Moreover, the structure of the non-conductive oxides is responsible for the absence of ionic conductivity.

2.8.4 Conclusions

All things considered, ionic conducive oxides are active towards the RWGS reaction. However, addition of other metals such as Cu, Fe and Pt can induce a synergic effect and further promote their RWGS activity. SDC, CeO_2 and YSZ have oxygen mobility and increasing the temperature can enhance their conductivity. SDC shows higher oxygen vacancies compared to YSZ and CeO_2. Hence, it can be deduced that SDC could be a better support in RWGS reaction. However, this hypothesis needs to be investigated within this research. Moreover, it has been reported in the literature that non-reducible oxides mainly improve the metal dispersion, but do not have a strong interaction with the metal catalysts.

Chapter 3: Catalyst Synthesis, Characterization and Catalytic Set-up

3.1 Synthesis of Cu- and Fe-based Nanoparticles

Copper and iron nanoparticles were synthesized using a polyol synthesis method (see Chapter 2, section 2.7). Triethylene glycol (TrEG) was selected as a suitable polyol for the synthesis of mono- and bi-metallic Cu- and Fe-based nanoparticles. The catalyst preparation procedure consists of the dissolution of metal precursor salts in 50 mL of TrEG (hygroscopic 99.8%, Acros Organics). Therefore, 0.3121 gr of copper (II) nitrate ($Cu(NO_3)_2$) (hydrate 99.999%, Alfa Aesar) was mixed with 30 mL TrEG in a round bottomed flask and was agitated for 1hr at ambient temperature in order to fully dissolve. The resulting solution was mixed with 20 mL solution of 0.254M NaOH (EM Science, ACS grade)/TrEG in order to raise the Ph of the solution to 11-12. Subsequently, the mixture was heated to 280°C under reflux and magnetic stirring inside a heating mantle for 1 hr. The color of the final mixture was hanna and the final Ph was 8.

The same procedure was implemented for the formation of Fe nanoparticles, except that 0.0187 gr of iron (III) nitrate ($Fe(NO_3)_3$) (nanohydrate, Fisher Scientific) was mixed with a mixture of 20 mL of TrEG and 30 mL of 0.254M/NaOH. According to the observations, the concentration of NaOH had to be higher for obtaining the same initial Ph (11-12), because higher basicity was required in order to reduce the electropositive Fe^{3+} species. Addition of higher concentration of NaOH gave rise to increasing the initial PH to 11. Following this, the Fe-containing mixture was refluxed under the same conditions as described for Cu. The resulting mixture became black in color and the final Ph was measured as 7.

The bimetallic colloids of CuFe with different compositions, namely 50 at.% Cu/ 50 at.% Fe (nominally $Cu_{50}Fe_{50}$) and 95 at.% Cu/ 5 at.% Fe (nominally $Cu_{95}Fe_5$) were prepared using the same approach. 0.3089 gr of the Cu salt ($Cu(NO_3)_2$, hydrate 99.999%, Alfa Aesar) and 0.032 gr of the Fe salt ($Fe(NO_3)_3$, nanohydrate, Fisher Scientific) were used to synthesize $Cu_{95}Fe_5$ nanoparticles. As for the synthesis of $Cu_{50}Fe_{50}$ colloid, 0.463 gr of the same Cu salt and 0.926 gr of the same Fe salt were used. The salts were added simultaneously to 50 mL solution of NaOH/TrEG and the concentration of NaOH varied in order to obtain an initial PH of 11-12. The final PH of the bi-metallic colloidal solutions was between 7-8 after reflux.

Then the colloidal solutions were cooled to room temperature under continuous stirring. The colloidal particles were kept in TrEG solution prior to their deposition on a catalyst support.

3.2 Synthesis of Ru- and Pt-based Nanoparticles

The formation of mono- and bi-metallic Ru- and Pt-based nanoparticles using polyol method has been previously reported (160) (117) (161). Ethylene glycol (EG) was used as the solvent (see Chapter 2, section 2.7).

0.2191 gr of $RuCl_3$ (anhydrous, Strem Chemicals) was mixed with 50 mL of EG solution containing 0.08M NaOH for the synthesis of Ru colloid. The Pt colloid was prepared by dissolving 0.4512 gr of $PtCl_4$ (99.9% metal basis, Sigma Aldrich) in 50 mL of EG solution. Then each EG solution was mixed for 1 hour at room temperature. The mixtures were subsequently refluxed for three hours at 160°C. Both of the resulting solutions were dark brown in color.

The bi-metallic RuPt colloid (50 at.% Ru/ 50 at.% Pt) was synthesized by following the same approach as described above; except that 0.0777 gr of $RuCl_3$ and 0.1285 gr of $PtCl_4$ were used and added simultaneously to 50 mL of EG.

Moreover, two bi-metallic Ru-Fe colloids with nominal compositions of $Ru_{90}Fe_{10}$ (90 at.% Ru/ 10 at.% Fe) and $Ru_{80}Fe_{20}$ (80 at.% Ru/ 20 at.% Fe) were synthesized in ethylene glycol under the same conditions. However, the amount of $RuCl_3$ varied from 0.1867 g to 0.1598 g for $Ru_{90}Fe_{10}$ and $Ru_{80}Fe_{20}$, respectively; with corresponding $Fe(NO_3)_3$ amounts of 0.149 g and 0.236 g.

The initial PH of all solutions varied from 10-11 and was dropped to 8 after the synthesis.

The colloidal solution were cooled to room temperature under stirring and were stored in EG before the addition of the support.

3.3 Nanoparticle Deposition on Conductive Supports

In order to deposit the nanoparticles on catalyst supports, 500 mg of each commercial support, namely ionically conductive oxides including YSZ (TOSOH), Fe_2O_3 (Sigma Aldrich) and mixed ionic-electronic conductive (MIEC) oxides including CeO_2 (Fuel Cell Materials) and SDC (Fuel Cell Materials) were weighed and added to a beaker. Subsequently, appropriate amount of the colloidal solution was added to the beaker containing the support and 20 mL of deionized water. Then the mixtures were under stirring for 48 hrs. For example, for the total Ru loading of 1 wt.% over CeO_2, 1.890 mL of the Ru colloidal solution with concentration of 2.1398 was added to a beaker containing 500 mg of CeO_2 support and 20 mL of deionized water. Then the mixture was under agitation for at least 48 hrs. Following that, the supported metal solution was transferred to a 45 mL centrifuge tube. The supported metal solution was centrifuged and washed with deionized water for at least three times. Subsequently, the catalyst was dried using a freeze dryer at – 46°C, under a pressure of ~ 0.2 mbar. The dried powder was crushed prior to use.

3.4 Physicochemical Characterizations of Nanoparticles

3.4.1 Scanning Transmission Electron Microscopy of Colloidal Nanoparticles

The scanning electron microscopy (STEM) was conducted on a FEI Titan 80-300 TEM at 300kev. Annular dark-field (ADF) images were acquired with a Fishione detector. They provided a contrast between different regions due to a difference in the atomic number (Z) and thickness of them. The values for convergence and collection angles were 17 and 60 mrad, respectively. In order to prepare the TEM specimens, the catalyst powders were sonicated in ethanol. One droplet of the solution was placed onto a 200 mesh TEM copper grid coated with a lacey carbon support film (Ted Pella) and was dried in air afterwards. Ru and Pt catalysts were identified as the bright features in the ADF-STEM images.

3.4.2 X-ray Diffraction of Colloidal Nanoparticles

X-ray diffraction (XRD) measurements were carried out over colloidal Cu and Fe solutions using a Bruker D8 Advance X-ray diffractometer that used a CuKa X-ray source (40 kV, 40 mA). The focused beam geometry had a divergence slit of 2/3 degree with a scan speed of 0.17 deg.min^{-1}. Data were taken for the 2θ range of 35 to 55 degrees and a step of 0.06 degree.

3.4.3 Infrared (IR) Spectroscopy of Colloidal Nanoparticles

A Fourier Transform infrared (FTIR) spectrometer (Cary 630 FTIR Spectrometer, Agilent Technologies) was used to determine the IR spectra of adsorbed CO on the colloidal nanoparticles of PGMs, namely Pt, Ru and $Ru_{50}Pt_{50}$.

First, a reference spectrum is measured on ethylene glycol without the presence of the colloids. Afterwards, a droplet of the colloidal metal solution was placed on the crystal. The spectrum was measured with the resolution 4cm^{-1} and a scan speed of 20 kHz. The measurements where carried out under the atmospheric pressure and ambient temperature.

3.4.4 Dispersion Measurements:

The CO titration method was used as a technique to implement dispersion measures on the supported Ru and Pt nanoparticles [161-163]. This procedure is preceded by a two-hour pre-reduction step at 300°C using H_2 (Linde, 99.99%). Afterwards, CO adsorption was carried out through introducing a gaseous mixture of CO and He (Linde, 1000 ppm CO in He) at the total flow rate of 15 ml.min^{-1} at 140°C in order to saturate the catalyst surface with CO. Feeding He as the purging gas at 100 mL.min^{-1} follows each CO adsorption step. Subsequently, the adsorbed CO was oxidized via flowing pure oxygen (Linde, 99.997%). Therefore, CO_2 was formed and further analyzed using an online non-dispersive infrared (NDIR) CO_2 analyzer (Horiba VA-3001). The measurements were taken on the assumption that CO/Pt and CO/Ru ratios are 1 and 2.3, respectively. Various purging periods ranging from 5 to 20 min were examined. The amount of adsorbed CO was calculated by extrapolation at time zero.

3.5 Catalytic Set-up:

The catalytic performance of all commercial and synthesized catalysts was evaluated in RWGS reaction in the temperature range of 300-600°C under atmospheric pressure. In order to measure the catalytic activity, a total 50 mg of the catalyst powder was placed into a 35 mL tubular fixed bed reactor. The reactant mixture was composed of 2 kPa H_2 (Linde, 100%), 2 kPa CO_2 (Linde, 99.99%), and balance He (Linde, 100%). It is important to note that the total pressure of the reaction was 100 kPa. The total gas flow rate was 100 mL.min^{-1} for RWGS reaction. The gaseous reactants first flowed through mass flow controllers (MFC, mks Instruments) and then they were introduced to the quartz reactor. The product gases were analyzed using a non-dispersive infrared CO analyzer (Horiba VIA-510) and subsequently a quadropole mass spectrometer (QMS, Ametek Proline DM 100). Prior to each measurement, QMS was purged with helium in order to eliminate all impurities. All the gases with a molecular weight up to 50 atomic mass units were identified using QMS.

Each set of experiments was repeated for three temperature cycles to ensure the stability and reproducibility of the catalytic measurements. All measurements were carried out starting from 300°C and each temperature was maintained for 30-45 min to ensure the steady-state conversion was reached.

The yield of CO was determined using the following equation, Eq. 3.1:

$$\text{Yield of CO (\%)}=\frac{[CO]_{OUT}}{[CO_2]_{IN}\ X\ 100\%} \qquad \text{(Eq. 3.1)}$$

Although the mass of the catalyst was held constant at 50 mg for all catalytic measurements, the gas hourly space velocity (GHSV) differed depending on the catalytic supports because each had a different bulk density (8.5 g.mL^{-1} for SDC and 3.95 g.mL^{-1} for γ-Al_2O_3). The GHSV values were measured using Equation 3.2:

$$\text{GHSV (hr}^{-1}\text{)} = \frac{\text{F xd}_{support}}{\text{W}_{support}} \quad \text{(Eq. 3.2)}$$

Where F is the total flow rate in mL/hr, d is the bulk density of the support in g/mL and W is the weight of the support in g. Therefore, the GHSV ranges from 473999.919h^{-1} to 1020000.51h^{-1} for γ-Al_2O_3-supported and SDC-supported catalysts, respectively; meaning that the reactants residence time in the reactor is greater in the case of catalysts supported on γ-Al_2O_3.

The CH_4 selectivity of the catalysts was measured using the mass spectrometer. The peak maximum values obtained from of the mass spectra were used in order to calculate the amount of unreacted CO_2 as well as the methane yield. The CH_4 selectivity was calculated using the Equation 3.2:

$$CH_4 \text{ selectivity (\%)} = \frac{CH_4(out)}{CO_2(feed) - CO_2(out)} \times 100\% \quad \text{(Eq. 3.3)}$$

Fig 3.10 shows the schematic diagram of the catalytic RWGS test station.

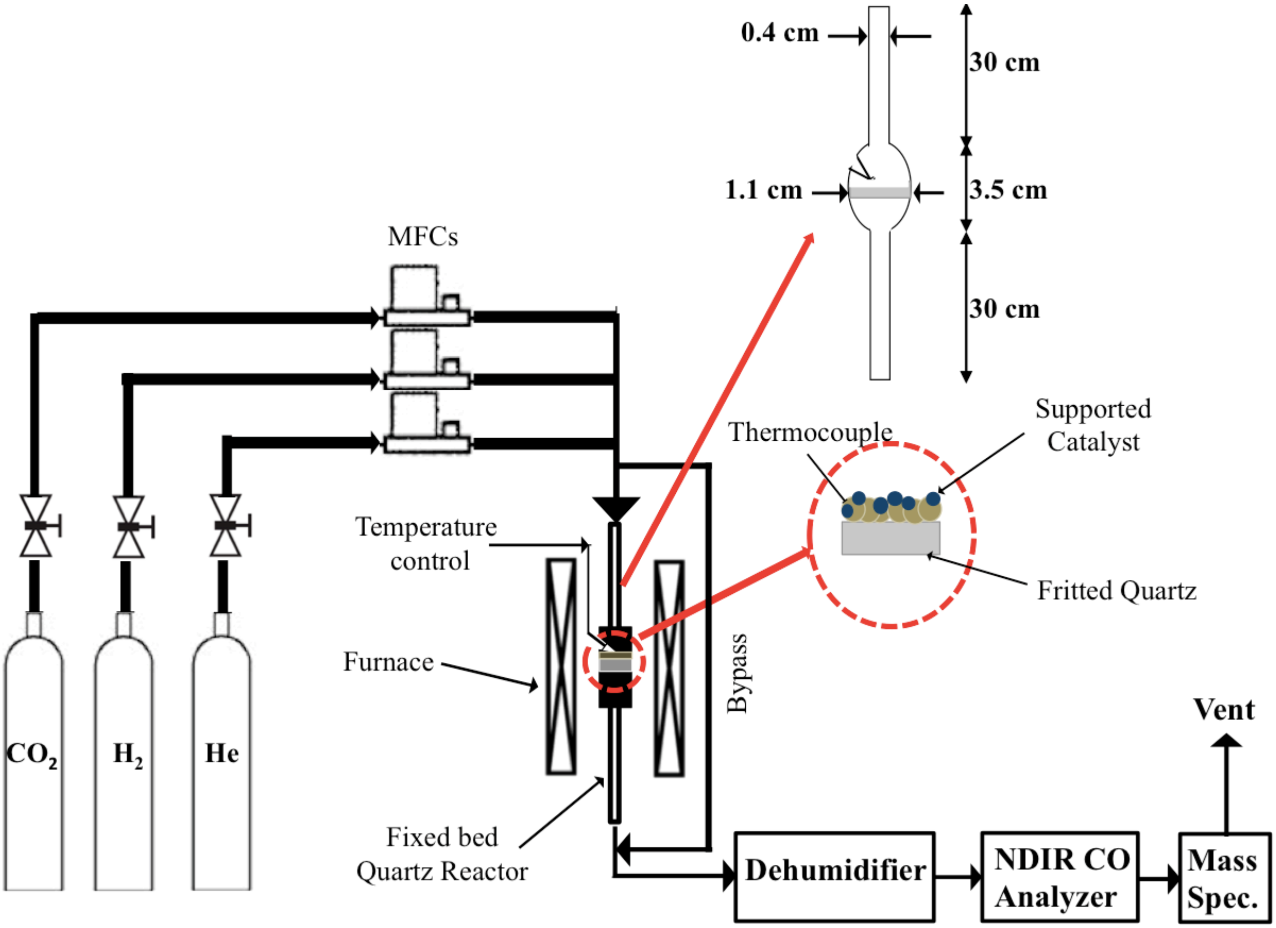

Fig 3.10: Schematic diagram of RWGS test station

Chapter 4: Characterization of Supported and Unsupported Metal Nanoparticles

4.1 Characterization of Cu- and Fe-based Colloidal Nanoparticles

The X-ray diffraction spectra of Cu and Fe colloids are shown in Figures 4.1 and 4.2, respectively.

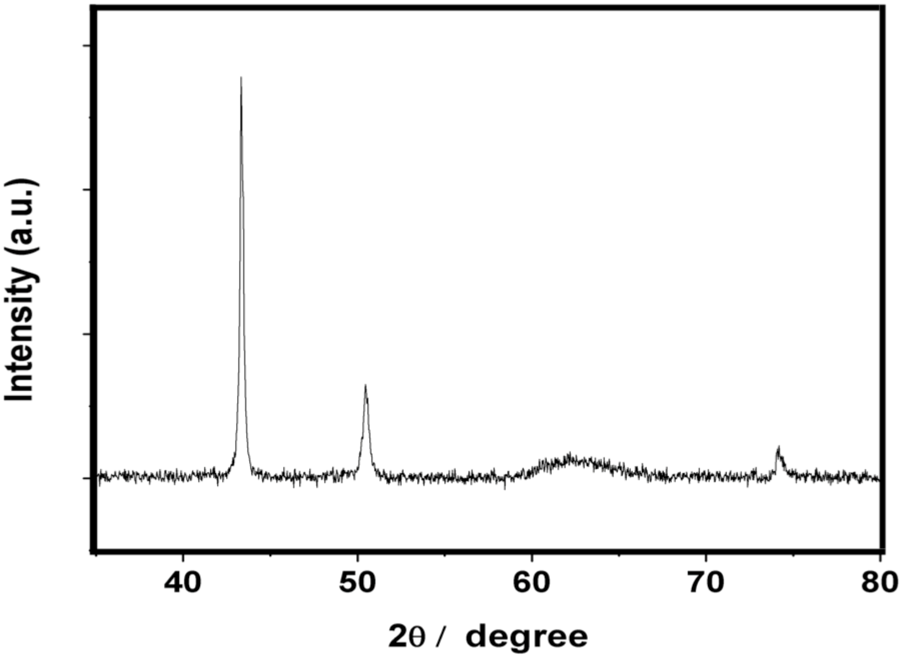

Fig 4.1: X-ray diffraction pattern for Cu nanoparticle colloids

Figure 4.1 evidences three peaks at 2θ values of 43.32, 50.43 and 74.01 deg, corresponding to (111), (200) and (220) planes. The high peak shown at (111) reflection corresponds to pure Cu. The experimental values for diffraction angles of the Cu colloid are in agreement with the standard diffraction angles for nano-sized Cu [164]. Therefore, Cu nanoparticles were successfully produced in triethylene glycol using a modified polyol synthesis method. No other impurities were detectable in the XRD pattern of Cu.

The crystallite size of the nanoparticles was estimated using the Debye-Scherrer formula, Eq. 4.1:

$$D=\frac{0.9\,\lambda}{\beta\cos\theta} \qquad \text{(Eq. 4.1)}$$

"λ" is the wavelength of X-ray (0.1541), "β" is FWHM (full width at half maximum), "θ" is the diffraction angle in radian and "D" is particle diameter. Using this formula, the average size of the Cu nanoparticles was 25 nm.

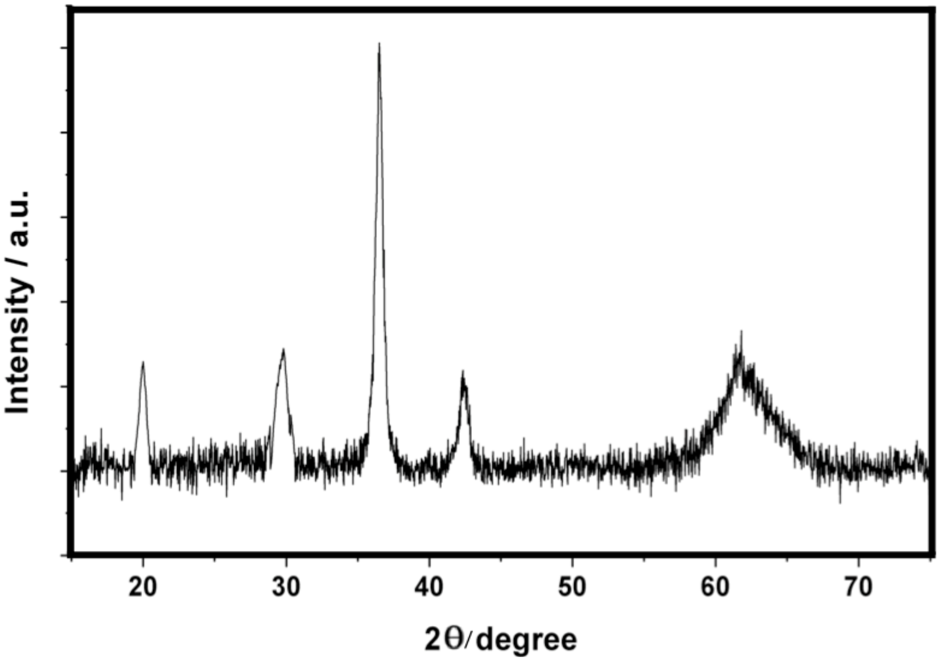

Fig. 4.2: X-ray diffraction pattern of the prepared Fe nanoparticle colloids

Figure 4.2 shows the XRD pattern of Fe colloids synthesized in triethylene glycol. The peaks were identified at 2θ values of 19.981, 29.010, 36.44, 42.192 and 61.268 corresponding to (111), (220), (311), (400) and (440) planes. It is noted that the diffraction angles are consistent with the standard patterns for magnetite (Fe_3O_4). All the peaks are related to Fe_3O_4 and no other impurities are visible. Moreover, the black color of the resultant Fe colloidal solution of further verifies the presence of magnetite phase.

The average crystallite size (D) is estimated using the Debye-Scherrer (Eq. 4.1). Furthermore, the interplanar spacing (d_{hkl}) is determined using Bragg's law (Eq. 4.2) and the value of the lattice parameter (α) is calculated using Eq. 4.3:

$$d_{hkl} = \frac{\lambda}{2\, sin\theta} \quad \text{(Eq. 4.2)}$$

$$d_{hkl} = \frac{\alpha}{\sqrt{h^2+k^2+l^2}} \quad \text{(Eq. 4.3)}$$

The values of α, d_{hkl} and D are summarized in Table 4.1.

Table 4.1: Crystallite size, d spacing and lattice parameter of the prepared Fe_3O_4 nanoparticle colloids.

d-spacing (Å)	Lattice parameter (Å)	Crystallite size from XRD (nm)
2.47	8.26	8.3

The d_{311} of 2.47 Å and α_0 of 8.26 are lower than the values reported for bulk magnetite ($\alpha_0 = 8.394$ and $d_{311} = 2.531$) indicating that another phase of magnetite, namely γ-Fe_3O_4 (d_{311} = 2.517 and $\alpha_0 = 8.347$) is formed [165]. It has been reported that γ-Fe_3O_4 is the first oxidized phase of magnetite [166]. Structural irregularities of synthesized magnetite could account for its further oxidation to γ-Fe_3O_4 [167]. The XRD pattern of Fe (Fig. 4.2), shows that the peaks are broader compared to those obtained for Cu. This indicates that the particle size of Fe is smaller compared to Cu. The average particle size of Fe_3O_4 nanoparticles is estimated to be 8.3.

4.2 Characterization of Ru- and Pt-based Catalysts

4.2.1 As-prepared Ru- and Pt-based Colloidal Nanoparticles

FT-IR measurements were carried out to determine the particle size of noble metal-based nanoparticles synthesized in ethylene glycol. It has been found that there is a correlation between the particle size and the IR spectra of CO adsorbed (CO_{ad}) in the case of

Ru- and Pt-based colloidal nanoparticles. It is noticeable that the CO gets adsorbed on the surface of the colloids during synthesis using polyol method and no further pre-treatment has been performed. The particle size of Ru, Pt and nominally $Ru_{50}Pt_{50}$ colloids were estimated using the IR spectra of CO_{ad}. [117]. Figure 4.3 demonstrates the FTIR spectra of Ru colloid.

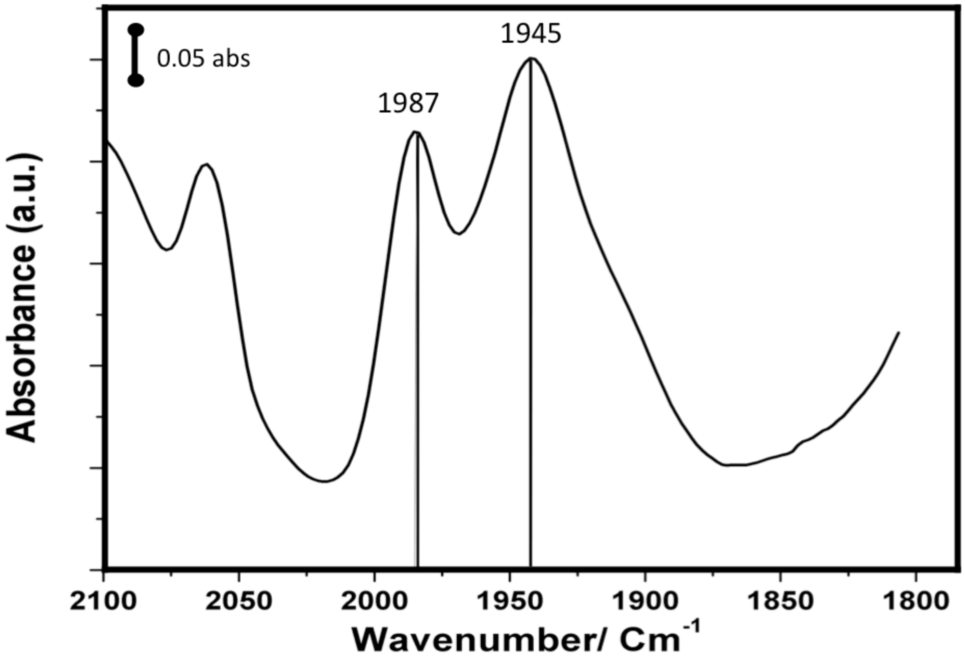

Fig. 4.3: FTIR spectra of Ru colloid synthesized in ethylene glycol

IR spectroscopy results for Ru colloid (Fig. 4.3) indicate two distinct bands at frequencies 1945 and 1987 cm^{-1}, corresponding to the typical bridged bonded CO_{ads} of Ru nanoparticles [168]. The 2-folded bridged band of adsorbed CO is expected to shift to higher frequencies (>1948 and 1990 cm^{-1}) for Ru particles larger than 2.8 ± 1 nm [117]. However, the two corresponding CO bands shown in Figure 4.3 are evident at frequencies 1945 and 1987 cm^{-1}. Therefore, the average particle size of Ru nanoparticles is smaller than 2.8 ± 1 nm. The Ru particle size was further measured via scanning transmission electron microscopy (STEM). Figure 4.4 shows the STEM images of Ru colloid.

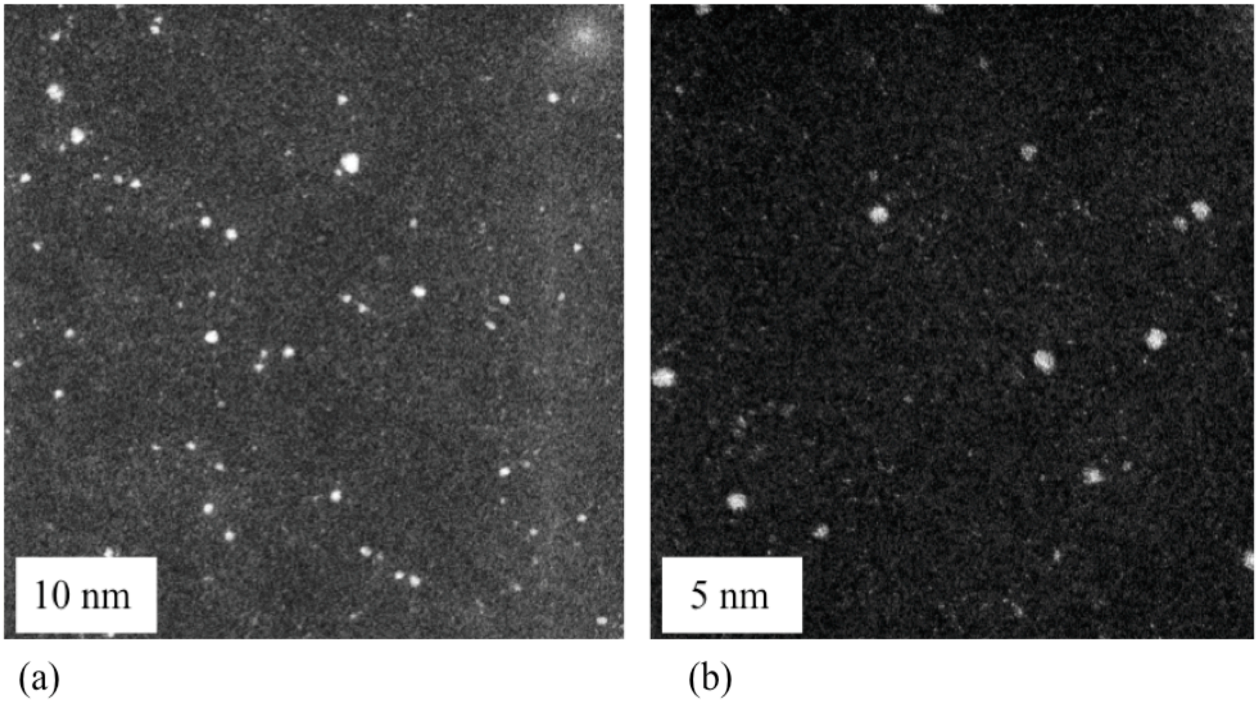

Fig. 4.4: STEM images of Ru colloid

The average particle size of Ru nanoparticles was measured to be 1.1 nm using ADF-STEM. Thus, the Ru particle size estimated using FTIR study (< 2.8 ± 1 nm) is close to the size measured from STEM (1.1 nm). However, the Ru particle size is marginally overestimated in IR measurement compared to STEM. The obtained Ru particles appear to be spherical and are well defined (Fig. 4.4).

Figure 4.5 shows the results of IR spectroscopy of Pt colloids. The position of the pronounced CO band observed in the range of 2010 to 2015 cm^{-1} can be correlated to Pt particle size. The adsorbed CO band tends to shift towards frequencies higher than 2050 cm^{-1} for particles larger than 2.5 ± 0.5 nm [117].

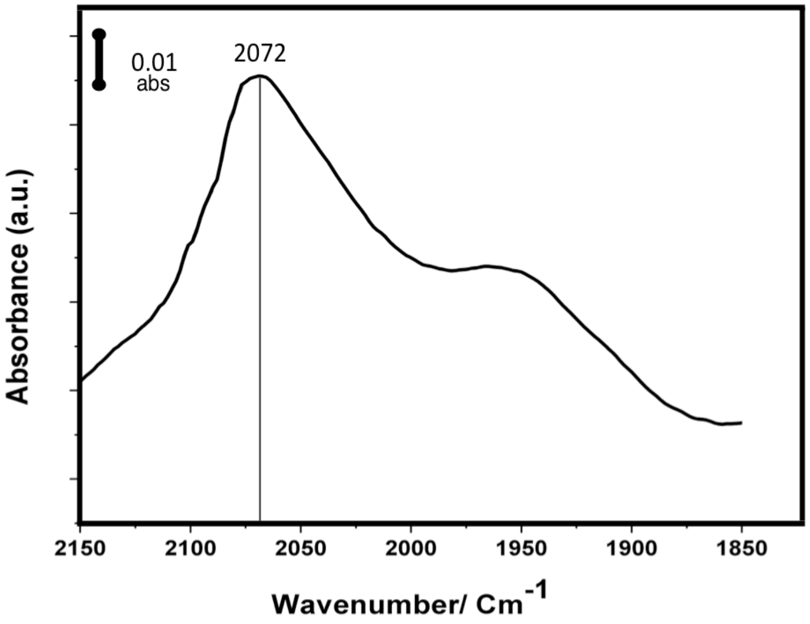

Fig. 4.5: FTIR spectra of Pt colloids synthesized in ethylene glycol

A noticeable peak can be observed at 2072 cm^{-1}. Therefore, the Pt colloidal particle size is expected to be close to 2.5 ± 0.5 nm. TEM measurements on Pt colloids were also carried out to measure the Pt particle size.

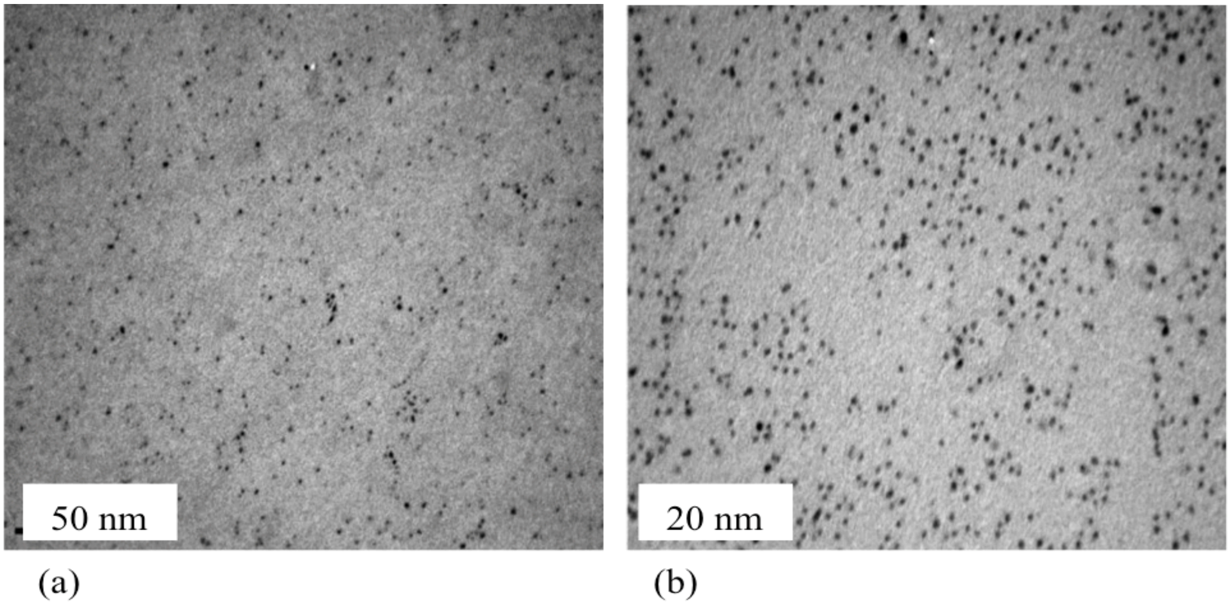

Fig. 4.6: TEM images of Pt colloid

According to TEM measurements, the average particle size of Pt colloids was estimated to be 1.9 nm. This value is less than one order of magnitude different from the value estimated from IR measurements (2.5 ± 0.5 nm). Resultant Pt nanoparticles are well defined and are dominantly spherical.

The approximate size of $Ru_{50}Pt_{50}$ colloid was also estimated using FTIR measurements. The IR spectra for the bi-metallic Ru and Pt colloid are expected to appear in the range of 1955- 2057 cm^{-1} and are depicted in Figure 4.7.

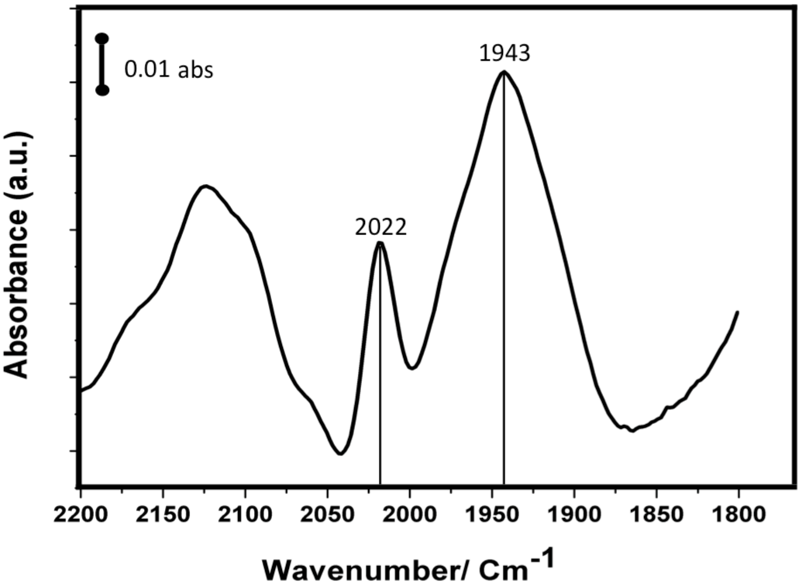

Fig. 4.7: FTIR spectra of Ru/Pt bimetallic colloids synthesized in ethylene glycol

As shown in Figure 4.7 the pronounced band visible at 2022 cm^{-1} is generated due to CO stretch on Ru/Pt step sites. Moreover, a shift towards lower frequencies is expected for larger Pt domains over Ru substrates [169]. The peak observed at the frequency of 1943 cm^{-1} is reportedly related to the bridged bands seen for Ru. There is an inverse relationship between the intensity of the band at 2022 cm^{-1} and the particle size for Ru/Pt colloids. Considering the frequency and peak intensity of the adsorbed CO spectra (Fig. 4.7), the particle size of $Ru_{50}Pt_{50}$ can be estimated in the range of 1.6 ± 0.5 nm [117].

4.2.2 Ru- and Pt-based Supported Nanoparticles:

Figure 4.8 shows the STEM micrographs of 1 wt.% Ru supported on CeO_2. The STEM confirms the uniformity and sphericity of the supported Ru nanoparticles. Furthermore, it is evident that nanoparticles are finely dispersed on the support and no major agglomeration is visible. The average particle size of 1wt.%Ru/CeO_2 was measured as 1.1 nm from TEM. Therefore, it is similar to the particle size of colloidal Ru.

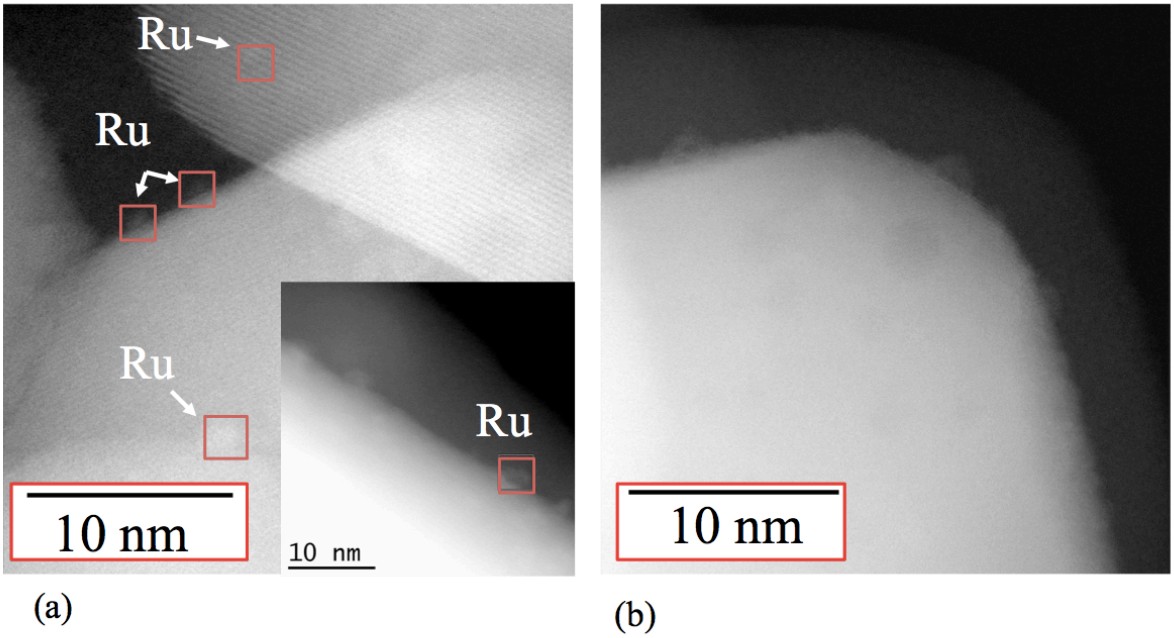

Figure 4.8: STEM images of 1 wt.% Ru/CeO_2

Figure 4.9 shows the STEM micrographs of 5 wt.% Pt/CeO_2. The average size of 3.8 nm is calculated from STEM measurements. It is noticeable that the average particle size decreases by almost two orders of magnitude with increasing the Pt content to 5 wt.%, whereas the particle size of CeO_2-supported 1 wt.% Pt was similar to that of Pt colloids (1.9 nm). The increase in the particle size can be attributed to the relatively high metal loading of Pt that results in decreasing the metal dispersion and gives rise to particle agglomeration.

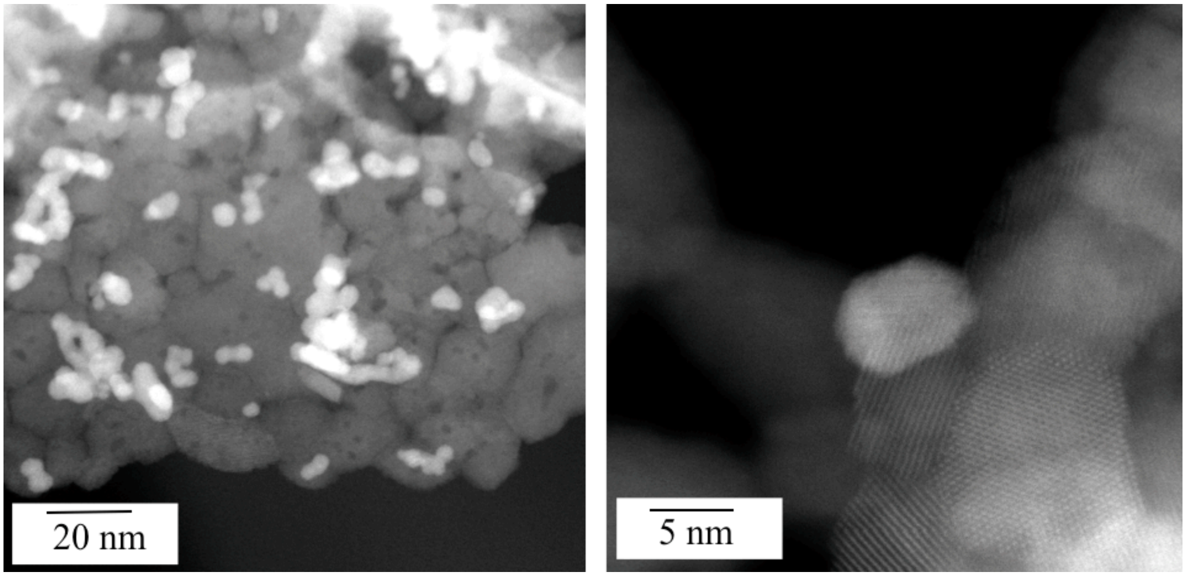

Fig. 4.9: STEM images of 5 wt.% Pt/CeO_2

4.2.3 Dispersion Measurements

The metal dispersion values of 5 wt.% Ru and Pt nanoparticles supported on CeO_2 and SDC were measured using the CO titration technique. Ru and Pt dispersion values and corresponding sizes are reported in Table 4.2. The estimated sizes were calculated using Eq. 4.4:

$$d_{nm} = \frac{600\,.\,M_w}{\rho\,.\,dispersion\,(\%).\;a\,.\,N_a} \qquad \text{(Eq. 4.4)}$$

Mw, ρ, α, N_α, and d_{nm} respectively represent metal molecular weight, metal density, atomic surface area of the metal, Avogadro's number, and d_{nm} indicates the average particle diameter [170].

Table 4.2: Metal dispersion and size of supported Ru and Pt catalysts

Catalyst metal	Colloidal particle size from TEM (nm)	Supported catalyst	Dispersion from CO titration method (%)	Supported particle size (nm)*
Ru	1.1	5 wt.% Ru / CeO_2	21	2.7
		5 wt.% Ru / SDC	13	3.3
Pt	1.9	5 wt.% Pt / CeO_2	43	3.1
		5 wt.% Pt / SDC	22	3.6

* From Eq. (4.4)

According to the results summarized in Table 4.2, the specific surface area of the support plays an important role in determining the dispersion of Ru and Pt nanoparticles. It is noted that the metal dispersion of Ru and Pt catalysts supported on CeO_2 (SSA = 30-50 m^2/g) is higher compared to those supported on SDC (SSA = 35 m^2/g). Furthermore, Table 4.2 indicates that regardless of the colloidal particle size of Ru and Pt nanoparticles, the particle sizes of SDC-supported Ru and Pt catalysts are larger than those supported on CeO_2, implying that the extent of metal agglomeration is higher for SDC-supported catalysts.

Chapter 5: Ionic and Non-ionic Conductive Oxides for RWGS Reaction

5.1 Introduction

Metal oxides exhibit several properties that made them interesting in heterogeneous catalysis. Moreover, they are considered as typical substrates for metal catalysts. The oxide supports can be ionically conductive, e.g., yttria-stabilized zirconia, 8mol.% Y_2O_3-ZrO_2 (YSZ), mixed ionic-electronic conductive (MIEC), e.g. CeO_2 and non-ionic conductive, e.g. Al_2O_3 and SiO_2 [171]. With respect to conductive metal oxides (YSZ, CeO_2, Sm-doped CeO_2, etc.), their high ion conductivity at elevated temperatures (350^{o}C) allow their use as solid-electrolytes in solid oxide fuel cells (SOFCs) and high temperature electrolyzers [125]. Utilization of solid electrolytes opens new doors in heterogeneous catalysis [172] [173] [161].

This section aims to identify the most active oxide material for the RWGS reaction, so that they can be further used as substrates for the dispersion of the selected metal nanoparticles. Another key goal of this chapter is to investigate the effect of ion and electron conduction in the RWGS reaction under the operation conditions described in Chapter 3. The performance of each metal oxide as well as carbon support was examined in terms of activity, selectivity and stability towards the RWGS reaction.

Hereinafter, detailed information regarding the commercial conductive and non-conductive supports, namely gamma-alumina (γ-Al_2O_3), carbon black (C), cerium IV oxide (CeO_2), samarium-doped ceria (SDC), yttria-stabilized zirconia (YSZ), titanium dioxide (TiO_2), and hematite (Fe_2O_3) is provided.

5.1.1 Properties of Commercial Metal Oxides

Gamma-alumina (γ-Al_2O_3): γ-alumina is extensively used as catalytic support at the industrial scale because it improves the metal dispersion as a result of its high surface area [174]. However, in applications requiring high temperatures (e.g. 600°C and higher), such as the RWGS reaction, γ phase of aluminum oxide readily transforms to metastable θ-Al_2O_3. Therefore, thermal stability improvement of γ-alumina for high-temperature applications is essential. In the present work γ-Al_2O_3 from Alfa Aesar was tested and its selected properties are shown in Table 5.1.

Table 5.1: Selected properties of γ-alumina

Property	**Value**
Grain size, micron	1-3
Density, g/cm^3	3.95
Melting point, °C	2072
Specific Surface Area, m^2/g	120

- From supplier

Carbon black (C): Carbon serves as both a catalyst and catalyst support for hydrogenation reactions due to its high porosity and specific surface area. Carbon black is a popular support material in electro-catalysis for fuel cells due to its high surface area and electronic conductivity. Among the three popular phases of carbon as catalytic support; namely carbon black, activated carbon and graphite, activated carbon has received more interest [175].

Improved metal dispersion is obtainable over C-supported catalysts. Additionally carbon black is classified as a non-ionically conductive material due to the volatile surface oxygen species [176]. Carbon black Vulcan XC-72R from Cabbott Corp. was tested in this chapter and its properties are summarized in Table 5.2.

Table 5.2: Selected properties of carbon black

Property	**Value**[*]
Density, g/cm^3	1.7-1.9
Melting point, °C	2550
Specific Surface Area, m^2/g	254

- From supplier

Cerium IV oxide (CeO_2): Ceria as a mixed ionic-electronic conductive (MIEC) ceramic exhibits high stability in the cubic fluorite phase without the need for additives. The ionic conductivity is due to the presence of oxygen vacancies in its crystal structure. Addition of dopants such as gadolinium and samarium leads to increased oxygen mobility [177]. CeO_2 from Fuel Cell Materials was tested in the form of powder and its properties are shown in Table 5.3.

Table 5.3: Selected properties of CeO_2

Property	**Value***
Grain size, nm	15-30
Density, g/cm^3	7.132
Melting point, °C	2600
Specific Surface Area, m^2/g	30-50

- From supplier

Samarium-doped ceria (SDC): Samarium-doped ceria (Sm_2O_3 - CeO_2) has the highest ionic conductivity among ceria-based ceramics at in the temperature range of 500-700°C (178). Moreover, incorporation of trivalent Sm^{3+} ions leads to higher thermal and textural stability in ceria [125]. The SDC from Fuel Cell Materials (FCM) was tested and its properties are shown in Table 5.4.

Table 5.4: Selected properties of Sm_2O_3 (15mol%)- CeO_2

Property	**Value***
Grain size, nm	30-50
Density, g/cm^3	8.5
Melting point, °C	3140
Specific Surface Area, m^2/g	35

- From supplier

Yttria-Stabilized Zirconia (YSZ): YSZ is a zirconium-based ceramic wherein "yttria" (Y_2O_3) is incorporated to stabilize the crystal structure of "zirconia" (ZrO_2). Doping zirconia with yttria leads to the replacement of Zr^{4+} with Y^{3+} resulting in higher oxygen vacancies and as a result higher ion (O^{2-}) conduction. YSZ from TOSOH was used in this thesis with the properties summarized in Table 5.5.

Table 5.5: Selected properties of Y_2O_3 (8mol%)-ZrO_2

Property	**Value***
Conductivity at 300°C, mS/cm	1-3
Density, g/cm^3	5.9
Melting point, °C	2680
Specific Surface Area, m^2/g	13

- From supplier

Titanium Oxide (TiO_2): TiO_2 is a MIEC material and its physiochemical characteristics give rise to its extensive use in the field of heterogeneous catalysis. Relative high surface area and chemical stability of TiO_2, are two important features that support its extensive use in high temperatures applications such as the RWGS reaction [179]. TiO_2 from Alfa Aesar were tested towards RWGS reaction and the relevant properties are given in Table 5.6.

Table 5.6: Selected properties of TiO_2

Property	**Value***
Grain size, micron	< 40
Density, g/cm^3	4.23
Melting point, °C	1843
Specific Surface Area, m^2/g	35-65

- From supplier

Hematite (Fe_2O_3): Iron III oxide is the most chemically stable phase of iron over a wide range of Ph values [180]. It has been used extensively in heterogeneous catalysis and was tested here for RWGS. The Fe_2O_3 powder was purchased from Sigma Aldrich and its properties are shown in Table 5.7.

Table 5.7: Selected properties of Fe_2O_3

Property	**Value***
Grain size, micron	< 5
Density, g/cm^3	5.240
Melting point, °C	1538
Specific Surface Area, m^2/g	> 100

- From supplier

5.2 Catalytic Performance of Metal Oxides and Carbon Towards the RWGS Reaction

5.2.1 Catalytic activity

The RWGS reaction was investigated in the temperature range of 300 to 600°C. Reproducibility of the results was ensured by repeating each catalytic run for at least three times. Reaction yields were measured after the steady-state condition was reached. Initially, blank catalytic experiments with an empty reactor were carried out to determine the homogenous gas-phase contribution within the reaction temperature range. Experimental procedures are described in details in Chapter 3.

Figures 5.1 and 5.2 show carbon monoxide yield as a function of temperature for various materials as well as a blank reactor. The equilibrium conversion curve was calculated using Microsoft Excel. Therefore, thermodynamic calculations (using ΔH, ΔG, K_{eq} and etc.)

were performed in order to determine the equilibrium conversion at H_2/CO_2 ratio of 1. Without a catalytic material (empty reactor) there is little to no reaction occurring in the gas phase up to 600°C. Figure 5.1 represents the yield of CO as a function of temperature for non-conductive supports: gamma-alumina and carbon.

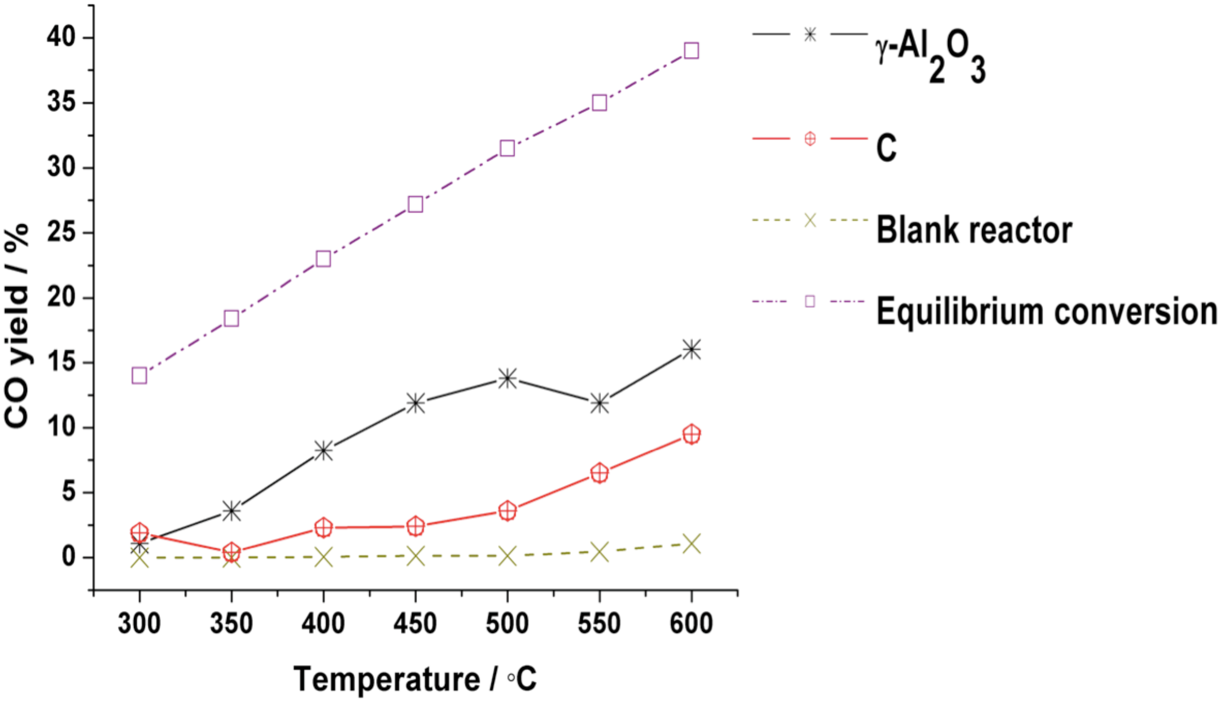

Fig 5.1: CO yield as a function of temperature over gamma-alumina and carbon black. Space velocity = 473999.919 h^{-1}, P_{H2}=P_{CO2}= 2kPa, balance He, F = 100 $mL.min^{-1}$

Figure 5.1 shows low CO yield over carbon black (C) and gamma-alumina (γ-Al_2O_3). Not only C exhibited poor catalytic activity, but also its highly variable nature of both pore and surface structure gave rise to irreproducibility of the measurements. Low reproducibility of the catalytic runs was also seen in the case of γ-Al_2O_3. Both of these non-conductive supports exhibit high specific area; however, on their own they show low activity for RWGS reaction. This finding is in agreement with the literature data [181]. Figure 5.2 presents CO yield as a function of temperature of MIEC and ionically conductive metal oxides.

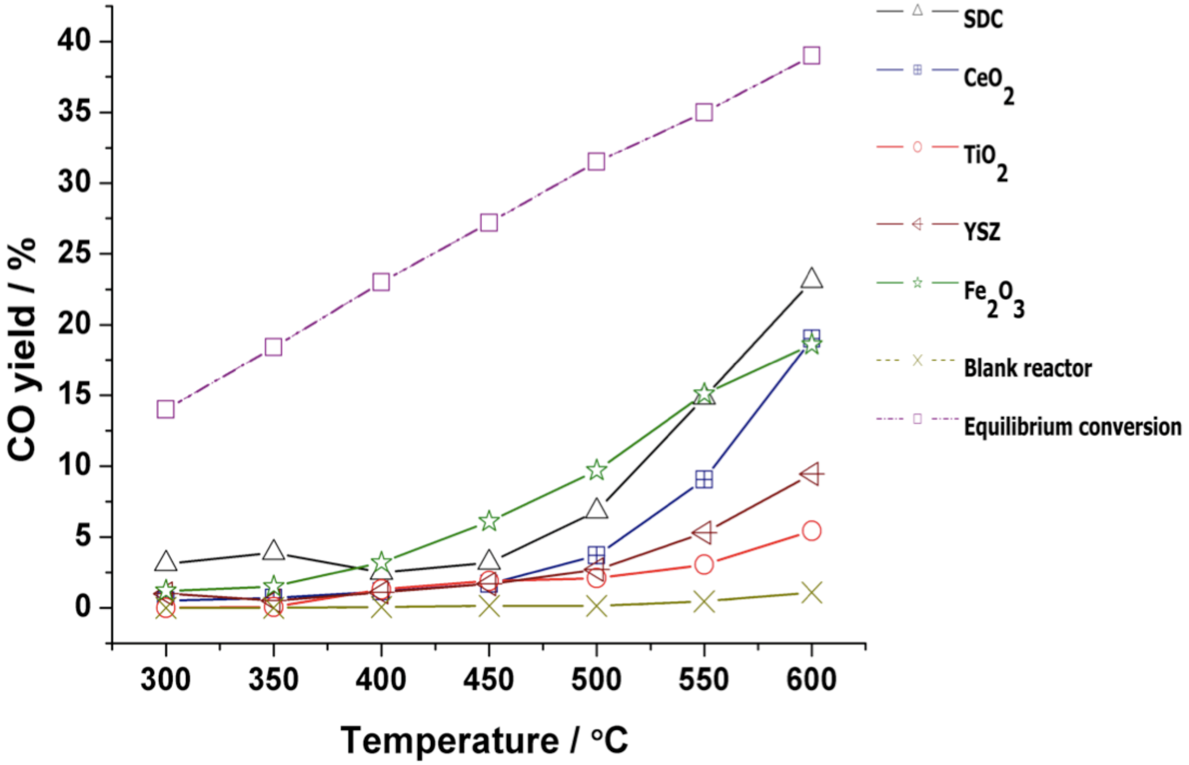

Fig 5.2: CO yield as a function of temperature for various metal oxides, as indicated in the figure. Space velocity = 1020000.51h$^{-1,}$ P$_{H2}$=P$_{CO2}$= 2kPa, balance He, F = 100 mL.min^{-1}

It is noted (Fig. 5.2), CO yield is negligible over all materials up to 450°C and then increases with temperature. SDC demonstrates a superior performance at 600°C compared to other supports followed by Fe_2O_3 > CeO_2 > YSZ > TiO_2.

Incorporation of Sm^{3+} as a lower-valent-cation dopant in CeO_2 facilitates the generation of more oxygen vacancies as a result of charge balancing and consequently improves ionic conductivity. It is noticeable that no other metal oxide dopant has outperformed samarium oxide (Sm_2O_3) in terms of promoting ionic conductivity in ceria [182]. Therefore, SDC exhibits higher reducibility compared to CeO_2.

However, it is important to investigate the potential correlation of reducibility with RWGS activity. It has been reported that reducibility leads to the promotion of the RWGS reaction towards the redox mechanism, which is believed to be one of the main mechanisms through which RWGS reaction proceeds [110] [76]. Moreover, the RWGS reaction mainly undergoes the redox mechanism over bare metal oxides [183]. Equations 5.1 present the redox mechanism in RWGS reaction:

$$CO_{2(g)} \rightleftharpoons CO_a + O_a$$
$$CO_a \rightleftharpoons CO_{(g)}$$
$$H_{2(g)} \rightleftharpoons 2H_a$$
$$H_a + O_a \rightleftharpoons OH_a$$
$$H_a + OH_a \rightarrow H_2O_a$$
$$H_2O_a \rightleftharpoons H_2O_{(g)}$$

(Eq.s 5.1): The redox mechanism in RWGS reaction

Successive redox cycles contribute to the production of CO and H_2O via the RWGS reaction. Catalytic contribution of ceria-based metal oxides can be attributed to promoting another pathway for the generation of oxygen adatoms (O_{ad}) and subsequently oxygen vacancies as illustrated in the following reactions [184], Eq. 5.2 and Eq. 5.3:

$$2CeO_2 \rightarrow O_{ad} + Ce_2O_3 \qquad \text{(Eq. 5.2)}$$
$$Ce_2O_3 + 1/2O_2 \rightarrow CeO_2 \qquad \text{(Eq. 5.3)}$$

Therefore, higher activity of SDC can be attributed to its higher reducibility compared to other evaluated metal oxides. It can be deduced that high ion conduction followed by increased oxygen mobility favors the RWGS reaction.

The results of CO yield over the conductive oxides (Fig. 5.2) demonstrate that ceria is also a suitable oxide material for promoting the RWGS reaction. The grain size of ceria is reported to be a determining factor on its both electron and ion conductivity [151]. Lower electronic conductivity and higher ionic conductivity have been observed for CeO_2 with smaller grain size. Considering pure CeO_2, electronic conductivity is expected to decrease for grain sizes below 100 nm [185]. It is notable that CeO_2 powders employed within this thesis work were between 30-50 nm. Therefore, the effect of the ionic conductivity of the ceria used in this work is expected to be higher, compared to its electronic conductivity. The improved RWGS performance of CeO_2 can be also attributed to its ionic conductivity.

Figure 5.2 indicates that CeO_2-based materials, namely SDC and CeO_2 as basic and reducible oxides, lead to high CO_2 conversion at 500°C and beyond. This also holds true for the rest of the conductive oxides but to a lesser extent. It is noted that there is a noticeable improvement in the catalytic performance of conductive metal oxides at 500°C and higher, whereas the CO yield is relatively slight below 450-500°C. Therefore, it can be inferred that ion conductivity is significantly a temperature dependent behaviour. This finding is in agreement with the literature data [182]. Interestingly, it has been reported that as of 600°C and beyond there is no further change occurring in the ion conduction of SDC [186].

It has been reported that the electronic conductivity of SDC is negligible at low temperatures in reductive environments [186]. However, the values for electronic conductivity of ceria-based oxides in hydrogen were reported to be 3-4 times higher than that of ionic conductivity at 500°C [187]. In addition, another group found that the measured values for electron conductivity are higher than that of ion conductivity as of 400°C to 800°C in the case of SDC and CeO_2 [186]. Therefore, electronic conductivity is not noticeable at low temperatures; however, at high temperatures (400°C and higher) its value is reported to be higher, compared to ionic conductivity. This can be also an explanation for the improved RWGS performance of SDC and CeO_2 at high temperatures.

High CO yield over Fe_2O_3 (Fig. 5.2) can be attributed to its partial reduction to magnetite (Fe_3O_4) as a result of introducing diluted hydrogen. Rapid electron exchange between Fe^{2+} and Fe^{3+} within the lattice of magnetite and therefore the generation of oxygen vacancies is the main reason for the good performance of magnetite in RWGS reaction [188]. However, over-reduction of Fe_2O_3 can result in the formation of metallic Fe (Fe^0) that is a suitable substrate for CO_2 adsorption and therefore, promoting the CO_2 methanation reaction. Moreover, it has been reported that Fe_2O_3 stabilize as FeO (Fe^{2+}) at high temperatures, which is an inactive phase of iron oxide towards RWGS reaction [189]. The decrease in CO yield over Fe_2O_3 at 550°C and higher, could be associated with the formation of either Fe^{2+} or Fe^0. Nonetheless, Fe_2O_3 demonstrated a suitable catalytic activity towards RWGS reaction (Fig. 5.2) and outperformed CeO_2 under the same reaction conditions.

TiO_2 demonstrates (Fig. 5.2) lower catalytic activity compared to the other conductive metal oxides. It is notable that TiO_2 exhibits both ion and electron conduction. However, conductivity of TiO_2 did not majorly come into play since it underperforms all the conductive supports including YSZ in the temperature of interest. Note that YSZ showed a better performance compared to TiO_2, despite the fact that YSZ exhibits no electronic conductivity.

5.2.2 Stability Measurements:

Thermal stability is one of the key evaluation criteria that a suitable RWGS catalyst must satisfy. Figure 5.3 shows the performance of C and γ-Al_2O_3 for three consecutive catalytic cycles from 300 to 600°C.

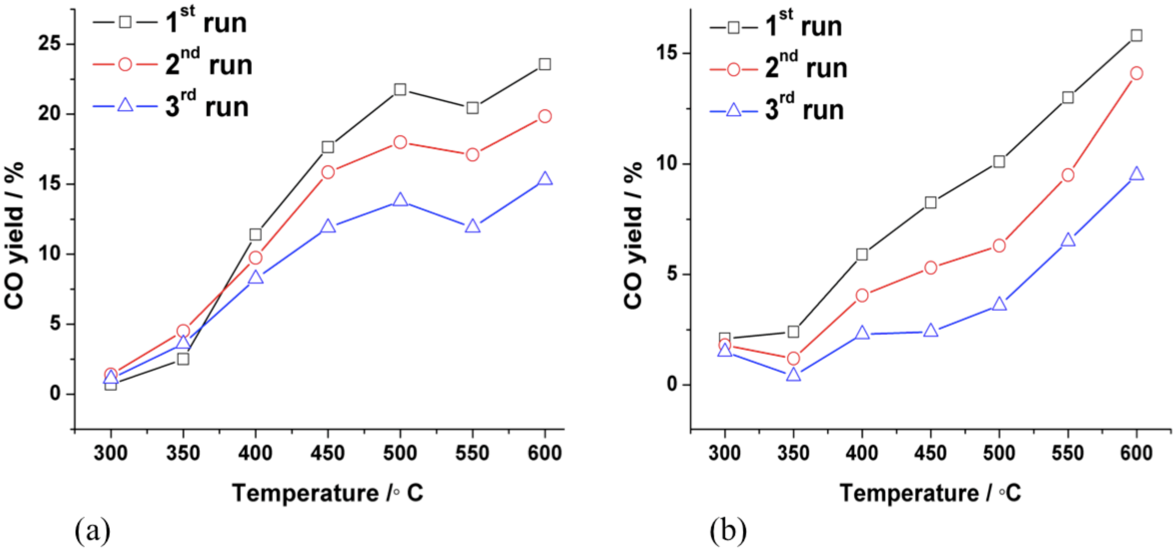

Fig. 5.3: Stability of (a) gamma-alumina and (b) carbon black in three consecutive catalytic runs. Space velocity = 473999.919 h^{-1}, P_{H2}=P_{CO2}= 2kPa, balance He, F = 100 ml.min^{-1}

The light-off curves shown in Figure 5.3 indicate that the catalytic measurements of gamma-alumina and carbon black show little stability and reproducibility particularly at high temperatures, whereas the catalytic runs observed for all other supports denoted high stability and reproducibility. According to Figure 5.3, the best CO yield can be observed during the first temperature cycles. Low stability of γ-Al_2O_3 and C is distinctly evident from 350-400°C. This is in agreement with the results of Oberlander et al. [190].

Figure 5.4 presents the three consecutive catalytic measurements of SDC and CeO_2.

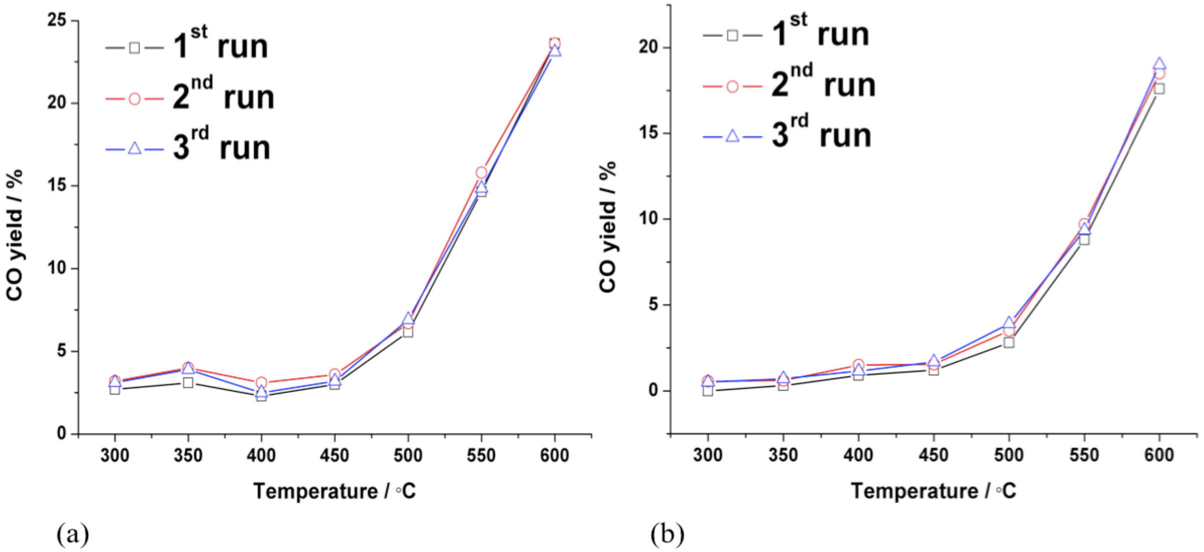

Fig. 5.4: Stability of (a) SDC and (b) CeO_2 in three consecutive catalytic runs. Space velocity = 473999.919 h^{-1}, P_{H2}=P_{CO2}= 2kPa, balance He, F = 100 ml.min^{-1}

The catalytic stability of SDC, CeO_2, YSZ and Fe_2O_3 was also evaluated using transient experiments for 24 hours at 550°C. The corresponding results are shown in Figure 5.5. Except for Fe_2O_3, no deactivation of other supports occurred after 24 hours.

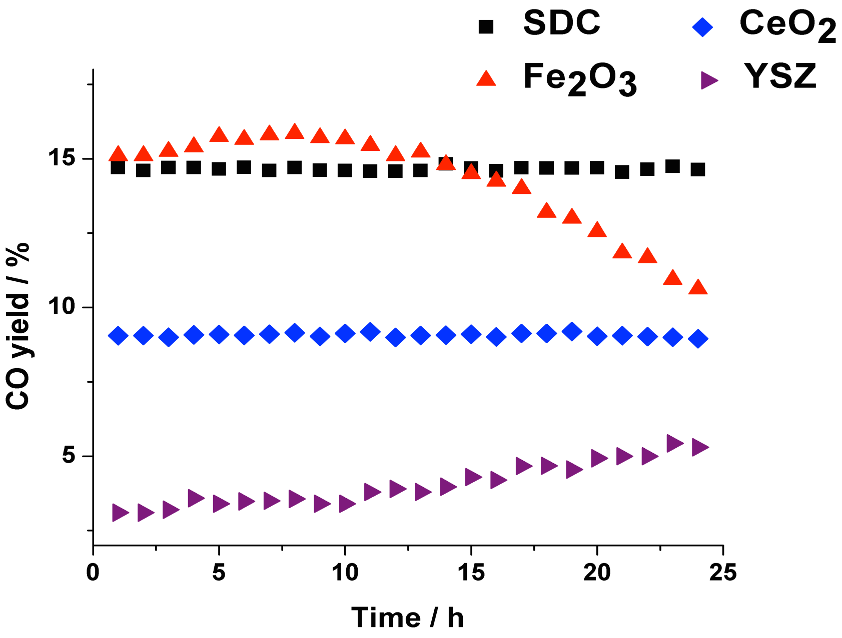

Fig. 5.5: Time-on-stream (TOS) behaviour over SDC, CeO_2, YSZ and SDC at 550°C, space velocity = 1020000.51h^{-1}; P_{H2}=P_{CO2}= 2kPa, balance He, F = 100 mL.min^{-1}

Good catalytic stability of ceria-based oxides (SDC and CeO_2) can be explained by taking their ion conduction into consideration. It has been reported that the ion conductivity of ceria-based oxides in a reductive environment, does not decrease as a result of repeated cooling and heating cycles [186]. This statement further acknowledges the veracity of our time-on-stream observations at 550°C. Evidently, our results indicate high stability of SDC and CeO_2. YSZ also indicates a good stability and hence, improvement in catalytic performance was observed over time. The stability of these materials at high temperature is also well known from solid oxide fuel cell literature where these oxides are used as solid electrolytes at temperatures as high as 900°C [125].

Hematite (Fe_2O_3) shows an excellent chemical stability [191]. In H_2 environments, Fe_2O_3 transforms to magnetite (Fe_3O_4) at 250°C and higher. Fe_3O_4 is the most active phase of iron in the RWGS reaction but its long exposure to reductive environments leads to its stabilization in the form of FeO_2 [192]. Moreover, it has been reported that iron stabilizes as Fe^{2+} in a variety of gas mixtures including CO_2 and H_2. In addition, exposure of Fe_2O_3 to high temperatures for a 24h period can lead to the formation of fully reduced iron (Fe^0) and also Fe-carbides that could result in a dramatic reduction in CO yield [193]. Thus, the yield of CO over Fe_2O_3 at 550°C (Fig. 5.5) shows an increasing trend over time for the first twelve hours followed by a dramatic decrease to almost two third of its initial activity during the next twelve hours.

Moreover, in the case of conductive oxides, the time needed for reaching equilibration at each new temperature within 300°C - 600°C was approximately 45 min, whereas the steady state is reached within a longer period for non-conductive oxides, namely gamma-alumina and carbon black.

5.2.3 Selectivity to Methane Formation:

Methane is the main by-product that can be generated alongside CO during RWGS reaction (see Chapter 1, section 1.2). Therefore, it is important to monitor CH_4 formation during the RWGS reaction. This was done using Mass Spectrometer (MS) as described in details in Chapter 3, section 3.5.

Results showed that He, CO_2, H_2, CO, H_2O and CH_4 were the only components identified in the mass spectrum of metal oxides. Figure 5.6 presents the mass spectrum of SDC at 600°C.

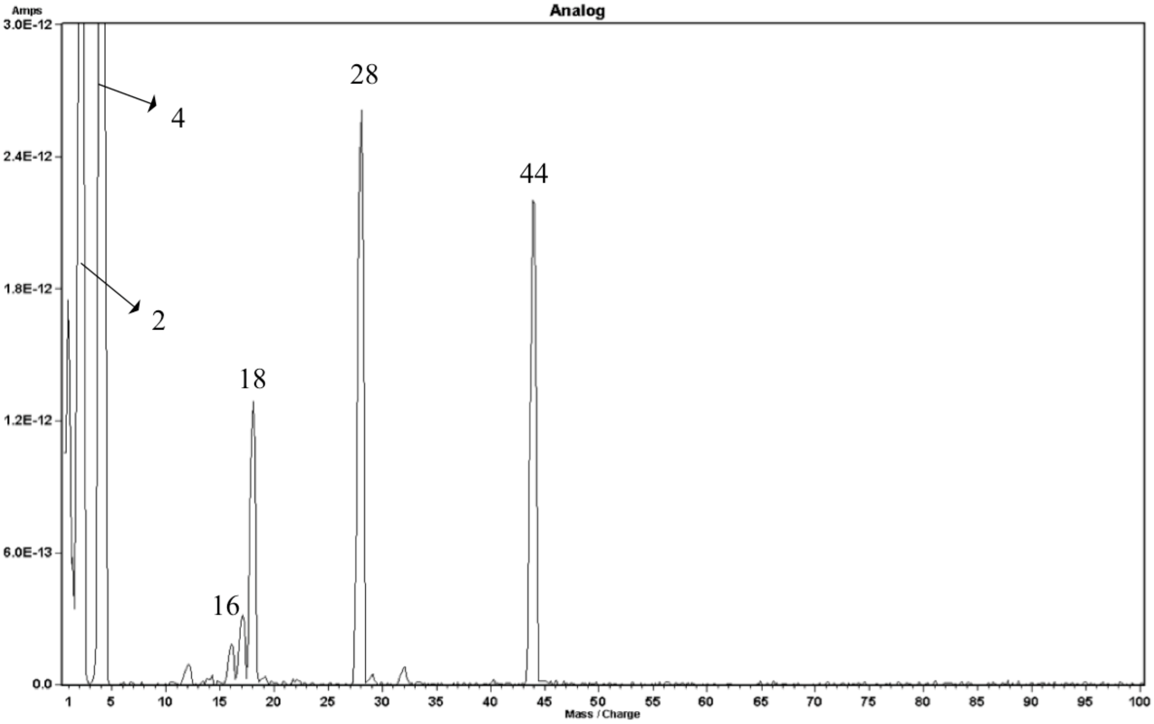

Fig. 5.6: Mass spectrum of SDC at 600°C in RWGS reaction. Space velocity = 1020000.51h^{-1}; P_{H2}=P_{CO2}= 2kPa, balance He, F = 100 mL.min^{-1}

The peaks identified at mass-to-charge (m/z) ratios of 2, 4, 16, 18, 28 and 44 correspond to H_2, He, CH_4, H_2O, CO and CO_2, respectively. It is important to note that the reactants were fed stiochiometrically in order to hamper CH_4 yield, which increases when H_2 amount increases and is favoured at high H_2/CO_2 ratios, e.g. $H_2/CO_2 = 4$.

It was found that CO and CH_4 were the main products formed in the temperature range of 300 to 600°C over metal oxides. Results presented in Figure 5.7 show CH_4 selectivity at varying temperatures.

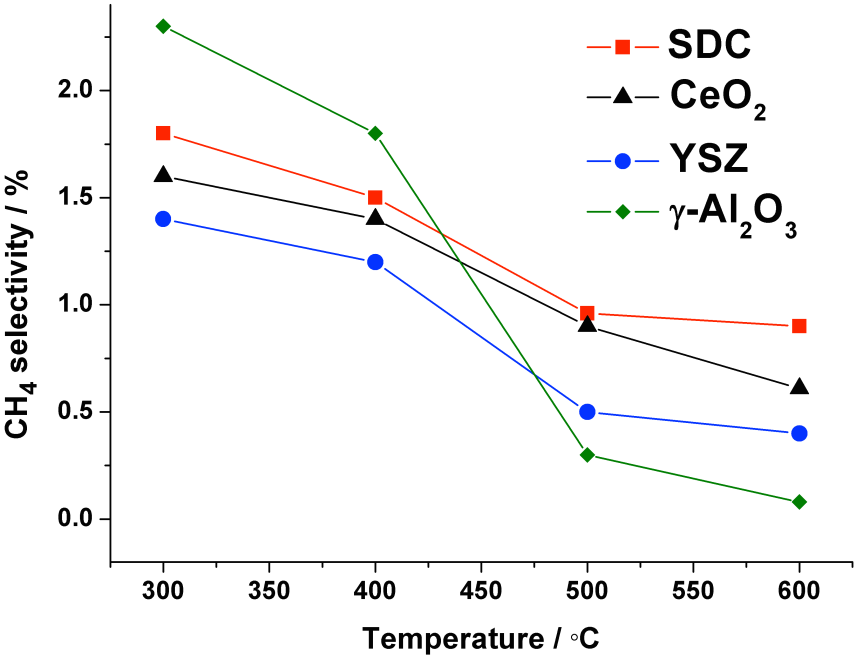

Fig. 5.7: Methane selectivity over conductive and non-conductive metal oxides from 300 to 600°C. Space velocity = 473999.919 h^{-1}; P_{H2}=P_{CO2}= 2kPa, balance He, F = 100 $mL.min^{-1}$

It is established that the extent of CO_2 adsorption indicates the CO_2 methanation activity of metal oxides [194]. Al_2O_3 does not show methanation activity by itself, but it is a very suitable substrate for the irreversible adsorption of CO_2 [195]. It has been reported that SDC and CeO_2 are not efficient promoters for the CO_2 methanation reaction [196]. Although ceria-based oxides are efficiently capable of CO_2 reduction, according to density functional theory calculations, CO_2 adsorption is not favoured on all CeO_2 facets except [110] [197]. As for 8mol% Y_2O_3-ZrO_2 (YSZ), existence of less reactive hydroxyl groups in YSZ compared to Y_2O_3, results in the lower strength of YSZ for CO_2 chemisorption; considering that CO_2 adsorption takes place upon its substitution with OH^- groups [198]. Therefore, higher CH_4 selectivity of γ-Al_2O_3 at lower temperatures (Fig. 5.7) can be explained by its higher affinity for the adsorption of CO_2 molecules.

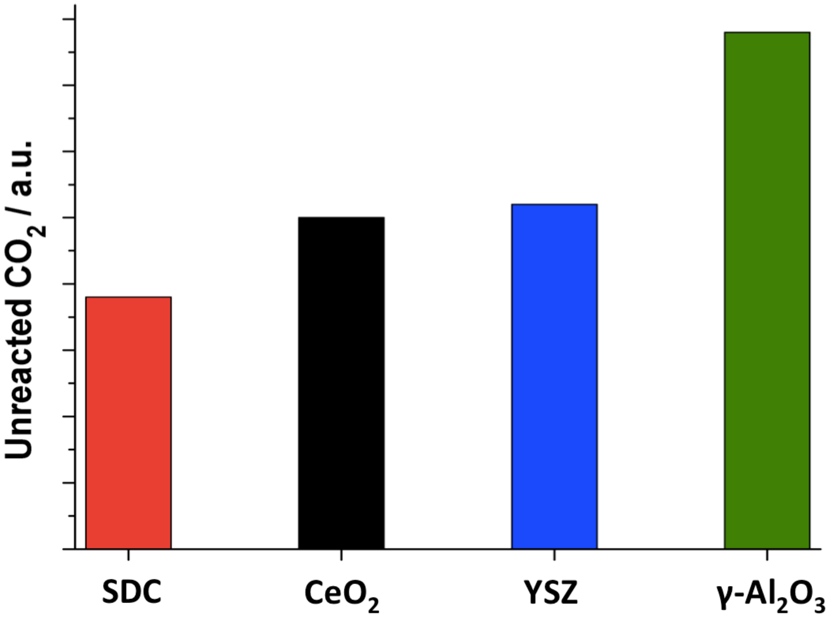

Fig. 5.8: Comparison of unreacted CO_2 at 600°C over conductive and non-conductive metal oxides. Space velocity = 473999.919 h^{-1}; P_{H2}=P_{CO2}= 2kPa, balance He, F = 100 ml.min^{-1}

As expected from thermodynamic viewpoint and as observed experimentally, the higher temperatures remarkably increase CO_2 conversion and CO formation in RWGS reaction. The noticeable decrease in the intensity of CH_4 and CO_2 mass spectra beyond 500°C, indicates the high selectivity of the reaction towards CO formation (Figures 5.7 and 5.8). Due to the exothermic nature of the CO_2 methanation reaction, higher methane yield is observed at lower temperatures (below 350°C), whereas higher temperatures clearly favour CO production.

Figure 5.8 shows that the CO_2 conversion was more over SDC compared to other oxides at 600°C, which indicates that SDC had more catalytic activity. Therefore, the amount of unreacted CO_2 observed over SDC is lower. The CO_2 to CO conversion at 600°C increases (Fig. 5.8) in the order of SDC > CeO_2 >YSZ > γ-Al_2O_3. It has been reported that YSZ promotes the methanation reaction up to 240°C, but at higher temperatures, methanation activity of YSZ is low [199]. Hence, it shows lower CH_4 selectivity compared to other metal oxides at higher temperatures.

5.2.4 Effect of H_2/CO_2 Ratio on CO Yield

The Effect of H_2/CO_2 Ratio on CO Yield was studied over conductive supports. Figure 5.9 represents the yield of CO as a function of temperature at two different partial pressures of H_2, i.e., H_2 to CO_2 ratio of 1 and 4. Increasing H_2 partial pressure considerably impacts CO_2 conversion and subsequently CO yield. According to Figure 5.9, regardless of the nature of the support, CO yield increases as of 450°C, which indicates that RWGS is the dominant reaction.

Results the measurements indicate that at lower temperatures (400°C and below), increase in H_2 concentration noticeably favours the CO_2 methanation reaction. Note that increased CO_2 conversion has been observed as a result of feeding higher H_2 concentrations. The RWGS catalytic results of CeO_2 and YSZ (Fig. 5.9) show higher methanation activity compared to SDC at 350°C and 400°C at $H_2/CO_2 = 4$, because of the decrease in CO yield. It can be deduced that at lower temperatures and higher H_2/CO_2 ratios, where CH_4 formation is thermodynamically favourable, SDC shows higher selectivity to CO.

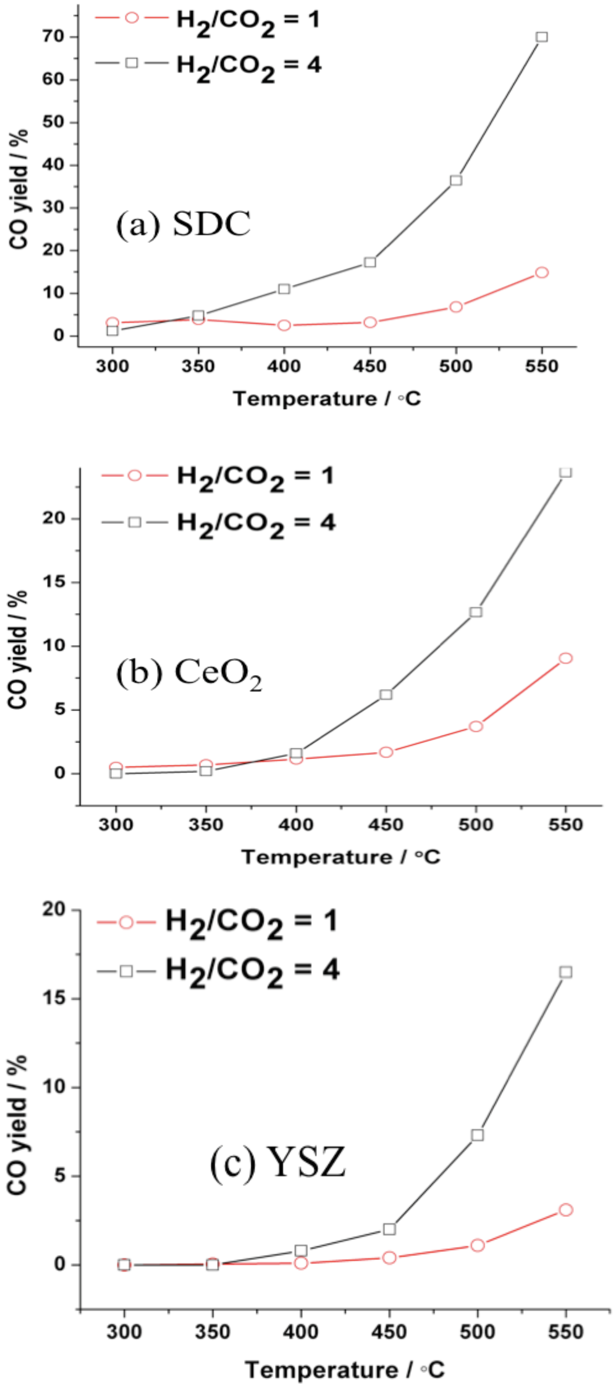

Fig. 5.9: CO yield as a function of temperature over (a) SDC, (b) CeO_2, and (C) YSZ at two different H_2/CO_2 ratios (1 and 4). Space velocity = 1020000.51h^{-1}, F = 100 mL.min^{-1}

5.3 Conclusions:

The catalytic performance of non-conductive and conductive metal oxides has been investigated for RWGS reaction in order to select the most suitable catalyst support for deposition of nanostructured metal catalysts. It was found that there is a difference in the behaviour of non-conductive conventional oxides (C and γ-Al_2O_3) and the oxides demonstrating oxygen mobility (e.g. SDC, YSZ and CeO_2). However, the stand-alone performance of metal oxides indicate that although none of the conductive materials approached equilibrium up to 600°C, they were capable of increasing the yield of CO considerably from 500°C and beyond. SDC as the best-performing metal oxide enhanced the reaction yield to 23% at 600°C. It is notable that the equilibrium conversion at 600°C is 39%.

SDC is not only the most active oxide in favour of RWGS reaction, but also in terms of methanation activity, SDC shows the least activity towards CH_4 formation in the temperature range of 300 - 600°C as opposed to other oxides. Moreover, the amount of unreacted CO_2 was the lowest at all reaction temperatures in the case of SDC, which indicates higher CO_2 conversion. These parameters altogether, made SDC the best-performing metal oxide in terms of activity, stability and selectivity in RWGS reaction.

According to the discussions and observations, conductivity comes into play with increasing temperature, which implies that ion and electron conductivities are temperature-dependent behaviours. Moreover, no definitive agreement could be made regarding the promoting effect of ionic conductivity compared to that of electronic, because they were both initiated at about 400 - 500°C. However, due to the absence of ion conductivity lower than 500°C, low CO yield indicates a negligible contribution from electronic conduction. Thus, below 500°C, neither ionic nor electronic conductivities are significant to promote the RWGS reaction.

The low catalytic activity and stability of γ-Al_2O_3 and C is an agreement with the literature. The RWGS catalytic activity over the investigated materials decreases in the order: SDC > Fe_2O_3 > CeO_2 > YSZ > TiO_2 > γ-Al_2O_3 > C. Fe_2O_3 as a conductive oxide exhibits a similar catalytic activity to that of SDC. However, the time-on-stream behaviour of Fe_2O_3 at 550°C shows poor catalytic stability, while SDC has high stability. Based on the results the following materials SDC, CeO_2, YSZ and Fe_2O_3 were chosen to serve as catalyst supports in the following chapters.

Chapter 6: Iron- and Copper-based Nanoparticles for RWGS Reaction

6.1 Introduction

The purpose of the present chapter is to develop and study Cu- and Fe-based catalysts for RWGS reaction using ionic and mixed-ionic electronic conductive (MIEC) metal oxides as supports. Moreover, this chapter aims at investigating the promotional effects of the ion (O^{2-}) conductivity of metal oxide supports on the performance of Fe and Cu nanoparticles. As described in details in Chapter 5, reducible metal oxides, namely samarium-doped ceria (SDC), ceria (CeO_2) and yttria-stabilized zirconia (YSZ) demonstrate good catalytic activity towards RWGS reaction, and higher the reducibility, the higher CO yield was observed. Therefore, the nanostructured mono-metallic Cu and Fe as well as bi-metallic Cu_xFe_{1-x} (x = 50 and 95 at.%) were synthesized and deposited on the most active supports from Chapter 5, namely SDC, CeO_2 and YSZ and the catalysts were studied for the RWGS reaction.

Copper surfaces are active in WGS reaction, and hence Cu is employed extensively as an effective shift catalyst particularly at low temperatures [200]. Moreover, as shown in Chapter 2, several studies proved that Cu is also an active site for catalyzing the high temperature RWGS reaction, when it is stabilized against “aging” at high temperatures. Cu is an appropriate adsorption site for CO_2 molecules, therefore Cu-based catalysts promote the RWGS reaction via the redox mechanism through oxidation of Cu^0 by CO_2 and subsequent reduction of Cu(I) by H_2 [201] [200].

However, the requirement of high temperatures for higher CO yields necessitates developing thermally stable Cu-based RWGS catalysts since they are susceptible to thermal sintering. Metallic Cu alone deactivates rapidly when exposed to high temperatures due to loss of surface area [202]. Furthermore, many studies indicate that Cu/CeO_2 systems have lower activity and stability in the presence of CO_2 and H_2 [203]. This addresses the need for employment of a stabilizer.

Many studies have been undertaken to stabilize copper at high temperatures. Stabilizing effects of manganese and alkali metals such as potassium (K) have been extensively studied. For instance, addition of potassium of 1.9% is claimed to increase CO_2 adsorption and facilitate formate decomposition over Cu/SiO_2 [204]. Fe is another promising stabilizer that showed better promoting results in Cu-based catalysts. As reported by Chen et al., incorporation of trace amounts of Fe is adequate in order to induce high catalytic activity to Cu/SiO_2 catalyst up to 120h at 600 °C [200]. In another study, higher stability and catalytic activity was reported for Cu-Fe/ZrO_2 catalysts due to the incorporation of Fe [205]. In addition, iron oxide is regarded as an active catalyst in RWGS catalysis [97].

In the present chapter, monometallic Cu and Fe and bimetallic catalysts with nominal compositions of $Cu_{95}Fe_5$ (95 at.% Cu - 5 at.% Fe) and $Cu_{50}Fe_{50}$ (50 at.% Cu - 50 at.% Fe) were synthesized using the polyol method as described in details in Chapter 3. Mono-metallic Cu and Fe were subsequently deposited on samarium-doped ceria (SDC), yttria-stabilized zirconia (YSZ) and cerium oxide (YSZ) supports, whereas the bi-metallic $Cu_{95}Fe_5$ and $Cu_{50}Fe_{50}$ nanoparticles were deposited on SDC. The loading of all mono- and bi-metallic Cu and Fe nanoparticles was nominally 5 wt.% when dispersed on the supports. These systems were put to the test in the temperature range of 300 -600°C. Stability measurements were performed at 550°C for a 48-hour period.

Synthesis of magnetite (Fe_3O_4) nanoparticles and their use in RWGS reaction is one of the novel features of this work as it is catalytically the most active phase of iron. It has been reported that the activity of unsupported Fe_3O_4 is better than that of metallic iron supported on γ-Al_2O_3 [206]. However, sintering is the main drawback that inhibits the catalytic activity of Fe_3O_4 at high temperatures over time [207]. Therefore, its structural stability needs to be improved through adding a stabilizer for long-term RWGS experiments.

6.2 Effect of the Support on CO yield over Cu and Fe_3O_4 nanoparticles

Prior to RWGS test, all supported catalysts were first pre-reduced at 450°C in a flow of 5 wt.%H_2/He for 1hr. The pre-reduction has a major effect on the catalytic activity of Fe-oxide based catalysts, since it can induce the partial reduction of Fe_2O_3 to Fe_3O_4 and further promotion of Fe-based catalysts [208]. XRD measurements shown in Chapter 4 confirmed the existence of iron nanoparticles in magnetite (Fe_3O_4) phase with a crystallite size of 8.3 nm and no visible impurities. Thus, Fe nanoparticles employed in this work mainly exist in the form of Fe_3O_4. Interestingly, magnetite is the most active and stable iron oxide phase in

RWGS and WGS reactions [206]. Moreover, XRD measurements show the formation of Cu nanoparticles with the average particle size of 25 nm.

Figure 6.1 presents the CO yield as a function of temperature over Cu and Fe_3O_4 nanoparticles dispersed over conductive oxide supports. As described in a detailed manner in Chapter 5, the good catalytic performance of conductive oxides namely SDC, CeO_2 and YSZ was attributed to their ion conduction and reducibility.

As can be seen, the yield of CO depends on the type of the support. Notably, catalytic activities of SDC-supported Fe_3O_4 and Cu are clearly higher, while no significant enhancement is evident in activity of supported Fe_3O_4 and Cu catalysts over CeO_2 and YSZ. Enhanced catalytic performance of SDC-supported Fe_3O_4 and Cu catalysts, in particular at low temperatures, can be ascribed to the higher oxygen conductivity of SDC than that of other investigated oxide supports. Higher ion conductivity of SDC gives rise to an increase in oxidation and reduction cycles of Fe_3O_4 and Cu. In addition, earlier catalytic activity of SDC-supported Fe_3O_4 and Cu can be attributed to higher bulk oxygen conductivity of SDC and therefore its facile oxygen ion (O^{2-}) diffusion at lower temperatures. This is particularly noticeable in the case of Fe_3O_4 nanoparticles. Increased activity of Fe_3O_4/SDC can be related to the metal-support interaction. It has been reported that there is a strong interaction between Fe-based oxides and oxide supports as a result of structural similarities [209]. Moreover, RWGS reaction proceeds through the redox mechanism over magnetite nanoparticles [210]. Thus, higher activity of SDC-supported magnetite can be attributed to the stronger interaction of SDC and Fe_3O_4, which could be related to the high oxygen ion (O^{2-}) mobility in SDC as well as electron exchange between both oxides.

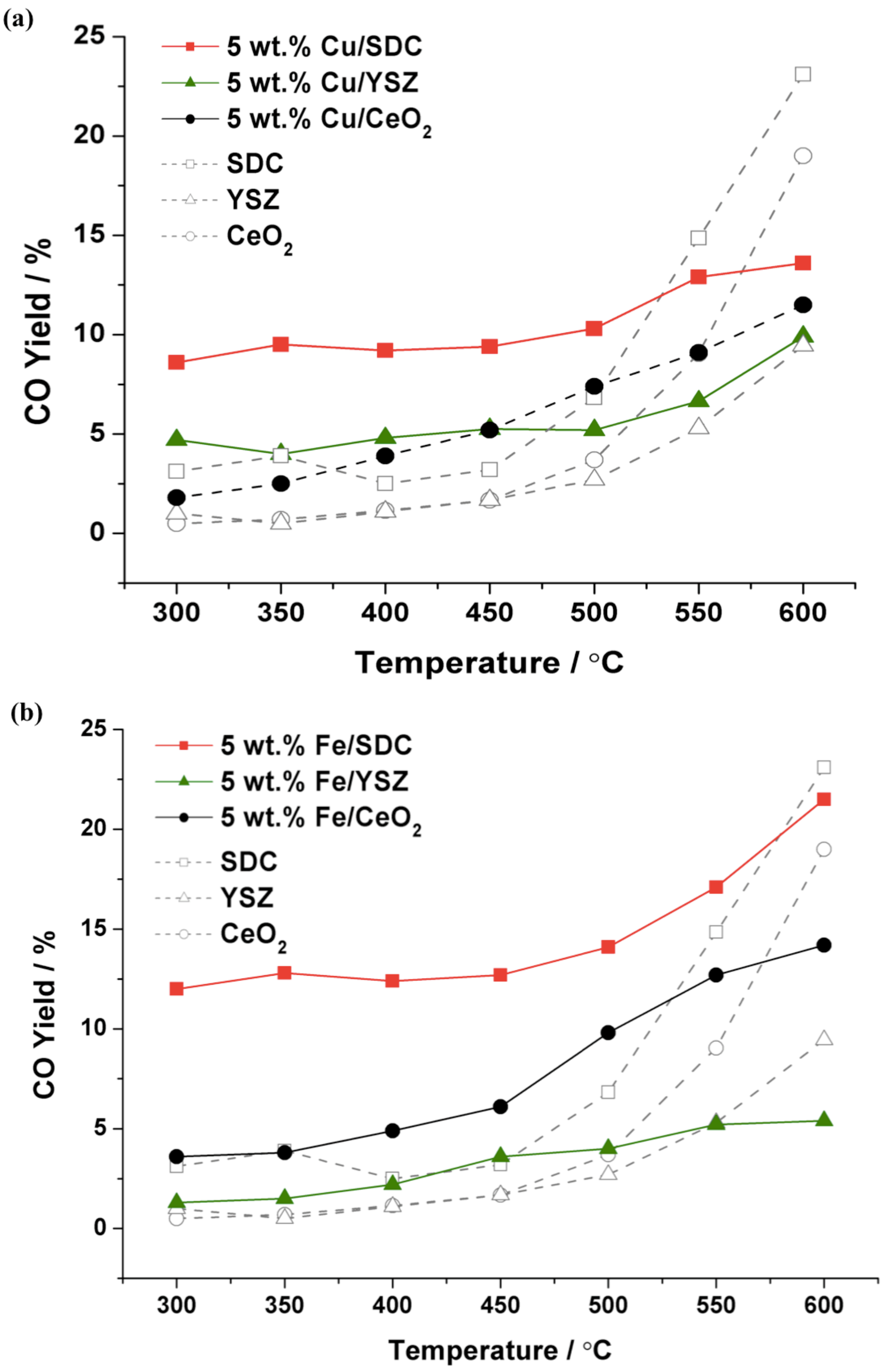

Fig. 6.1: CO yield over Fe_3O_4 and Cu nanoparticles supported on YSZ, CeO_2 and SDC. Dashed lines represent CO yield over blank YSZ, CeO_2 and SDC. Space velocity = 1020000.51h^{-1}; P_{H2}=P_{CO2}= 2kPa, balance He; F = 100 mL.min^{-1}

Magnetite as the most stable and active bulk phase of iron exhibited better performance compared to Cu as displayed in Figure 6.1. Easily accessible oxidation states of cations (Fe^{3+} and Fe^{2+}) in Fe_3O_4 can explain the higher catalytic activity of supported Fe catalysts as opposed to Cu catalysts. It is noted that the reducibility of the support is a determining factor in the catalytic activity of Cu and Fe_3O_4. Figure 6.1 demonstrates that the catalytic activity increases with the reducibility of the support increasing, as the promotion effect of the oxide supports is in the sequence of SDC > CeO_2 > YSZ. As for Cu catalysts, it has been reported that there is a strong interaction between copper and partially reduced ceria species in RWGS reaction [211]. Note that redox mechanism is the main route that Cu catalysts undergo in the RWGS reaction [204]. The redox mechanism over Cu-based catalysts in the RWGS reaction can be shown in the following scheme [212]:

$$CO_2 + 2Cu \rightarrow Cu_2O + CO$$

$$H_2 + Cu_2O \rightarrow Cu^0 + H_2O$$

Therefore, increased catalytic activity of Cu/SDC can be associated with the promotion of the reaction through the redox mechanism as a result of successive redox cycles occurring over the catalyst. As regards Fe-based catalysts, it is noticeable that they mainly stabilize as Fe^{2+} in CO/CO_2 gas streams and this could be responsible for their shorter lifetime, considering that Fe^{2+} cannot easily undergo redox cycles in WGS and RWGS reactions [193]. Addition of a support with high oxygen conductivity such as SDC can facilitate the re-oxidation of Fe^{2+}-stabilized species to more active iron oxide phases such as magnetite (Fe_3O_4) and hematite (Fe_2O_3). The decrease in the catalytic activity of Fe_3O_4/SDC observed at 550°C can be attributed to the excessive reduction of Fe_3O_4 to metallic Fe and therefore, lower CO yields. Thus, it is important for Fe-based particles to maintain their magnetite phase in order to be active in RWGS reaction.

All things considered, metallic copper and ion mobility in Fe_3O_4 as well as oxygen vacancies in conductive supports can be taken responsible for the better catalytic activity of Cu- and Fe_3O_4-loaded catalysts when compared to bare metal oxide supports at lower temperatures (300 - 550^{o}C). However the maximum yield achieved was only 20% at 600^{o}C for Fe_3O_4/SDC, which is far away from the requirements of the good catalysts; considering that the equilibrium conversion is 39% at 600°C. In order to improve the performance and stabilize Cu from deactivation, bi-metallic $Cu_{95}Fe_5$ and $Cu_{50}Fe_{50}$ catalysts deposited on SDC were studied next.

Figure 6.2 shows the activity of Fe_3O_4 and Cu over SDC for three consecutive catalytic measurements.

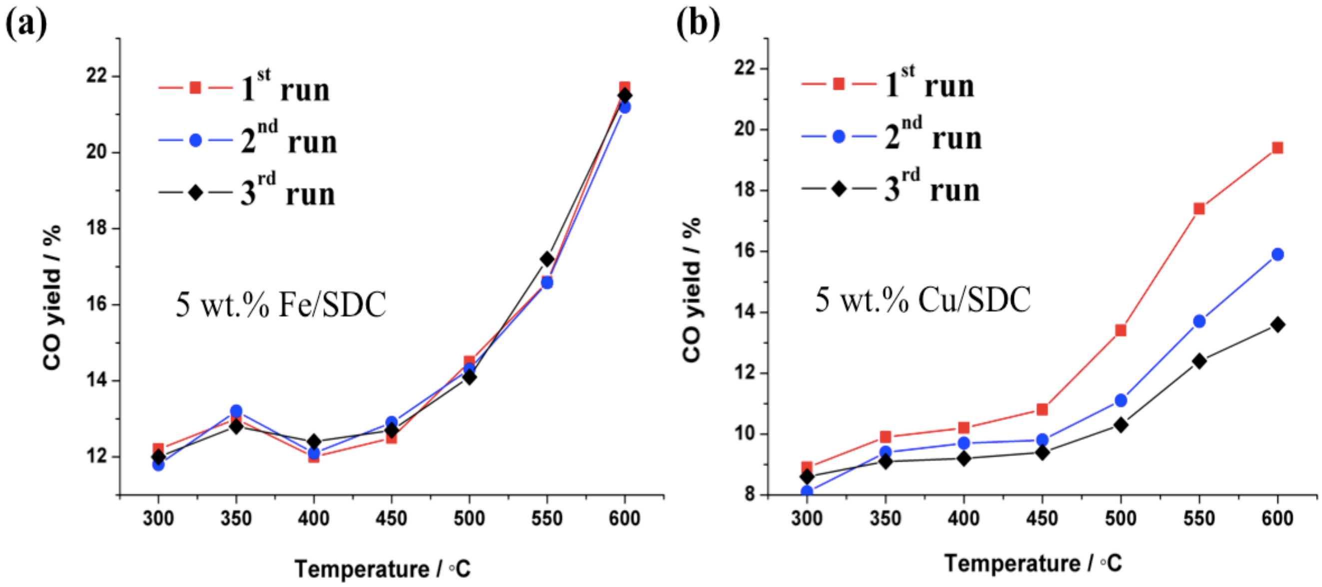

Fig. 6.2: Stability of 5wt.% (a) Fe and (b) Cu nanoparticles over SDC in three consecutive catalytic runs. Space velocity = 1020000.51h^{-1}, P_{H2}=P_{CO2}= 2kPa, balance He, F = 100 mL.min^{-1}

The SDC-supported Cu catalyst by itself had a poor catalytic stability, showing ~ 10% of reduction in CO yield in the third run at 600°C. Thermal sintering can be responsible for deactivation of Cu. Moreover, surface oxygen species from the support and CO_2 can oxidize Cu and stunt the progress of the reaction through the redox mechanism. On the other hand, figure 6.2 demonstrates the good stability of Fe_3O_4/SDC. This indicates that the Fe_3O_4 phase was maintained throughout the consecutive catalytic measurements and therefore no difference in the catalytic activity can be observed.

6.3 Activity and Stability of Bi-metallic Cu_xFe_{1-x} (x = 95 and 50 at.%) Catalysts Deposited on Samarium-doped Ceria

Bimetallic Cu-Fe nanoparticles of two different compositions ($Cu_{50}Fe_{50}$ and $Cu_{95}Fe_5$) were prepared as described in Chapter 3 and were supported on SDC. Figure 6.3 summarizes the results of the reaction experiments at different temperatures over the $Cu_{50}Fe_{50}$ and $Cu_{95}Fe_5$ as well as Cu and Fe_3O_4 dispersed on SDC.

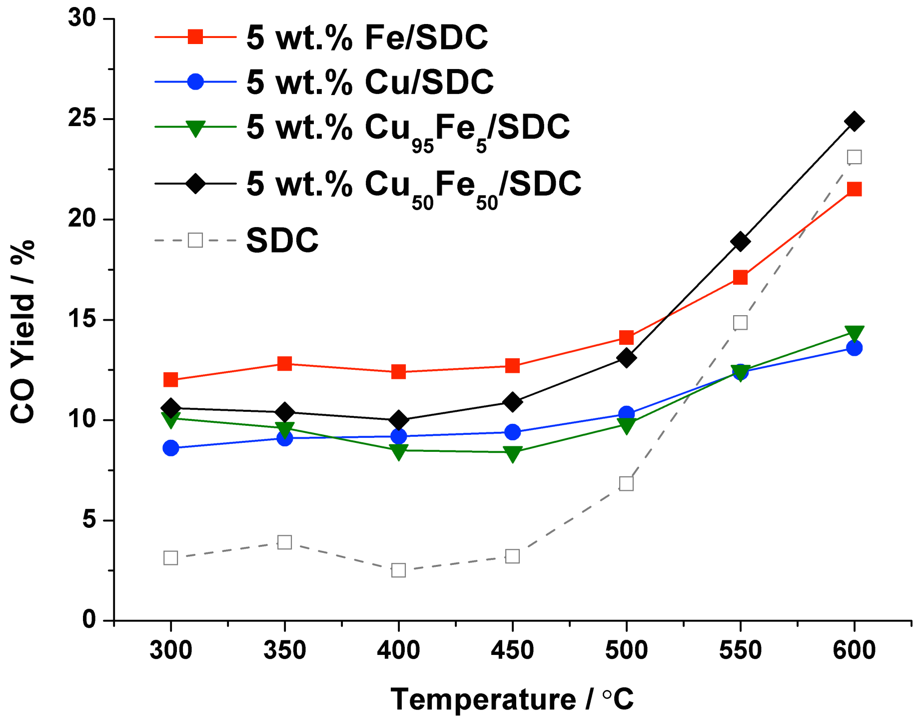

Fig. 6.3: CO yield over Fe, Cu, $Cu_{95}Fe_5$ and $Cu_{50}Fe_{50}$ nanoparticles deposited on SDC. Dashed line represents the yield of CO over blank SDC. Space velocity = 1020000.51h$^{-1,}$ P_{H2}=P_{CO2}= 2kPa, balance He, F = 100 mL.min^{-1}

Figure 6.3 demonstrates that Fe_3O_4 nanoparticles supported on SDC show higher CO yield than $Cu_{50}Fe_{50}$/SDC catalysts up to 500°C, whereas $Cu_{50}Fe_{50}$/SDC has the highest activity at 550°C and higher. This indicates the higher thermal stability of $Cu_{50}Fe_{50}$ compared to Fe_3O_4. Moreover, increased catalytic activity of $Cu_{50}Fe_{50}$ above 550°C can be also attributed to the synergistic effect of Cu and Fe nanoparticles in $Cu_{50}Fe_{50}$, which can prevent the over-reduction of Fe_3O_4 as well as over-oxidation of Cu. It is noted that (Fig. 6.3)

$Cu_{95}Fe_{50}$ showed the same activity as the mono-metallic Cu. Thus, it can be concluded that CO yield is directly proportional to Fe_3O_4 loadings for Cu-Fe catalysts.

Figure 6.4 represents the light-off curves of $Cu_{50}Fe_{50}$ nanoparticles dispersed on SDC. It is notable that the third run is the backward cycle with temperature decreasing from 600 to 300°C.

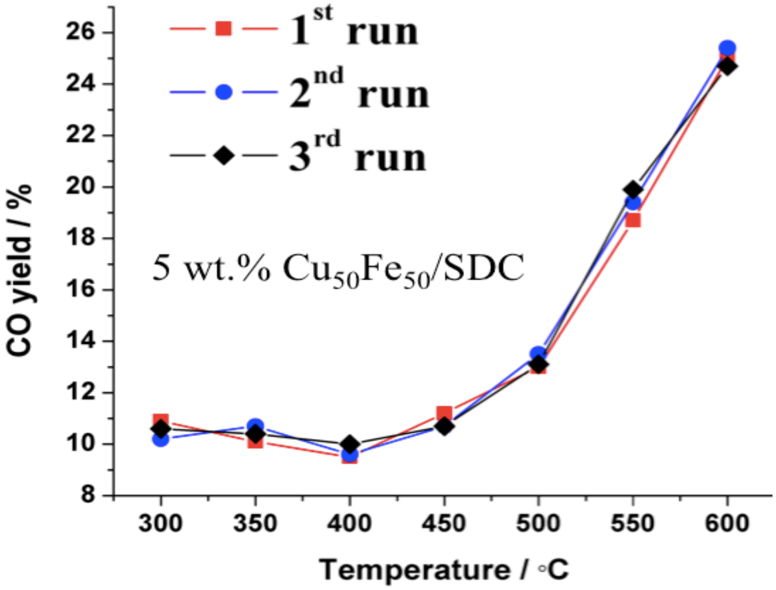

Fig. 6.4: Stability of 5wt.% $Cu_{50}Fe_{50}$ nanoparticles supported on SDC in three consecutive catalytic runs. Space velocity = 1020000.51h^{-1}, P_{H2}=P_{CO2}= 2kPa, balance He, F = 100 mL.min^{-1}

Figure 6.4 clearly shows the role of Fe in stabilizing Cu nanoparticles. It indicates that due to the addition of Fe_3O_4 to Cu, higher and constant catalytic activity was observed after three successive catalytic runs, while Cu/SDC showed a considerable deactivation (Fig. 6.2). Interestingly, $Cu_{50}Fe_{50}$ and $Cu_{95}Fe_5$ catalysts were stable to several reaction runs, indicating that 5 at. % of Fe was adequate to stabilize Cu nanoparticles.

SDC-supported Fe_3O_4, Cu and $Cu_{50}Fe_{50}$ catalysts were also evaluated for 48-hour time-on-stream stability experiments for RWGS reaction at 550°C as shown in Figure 6.5.

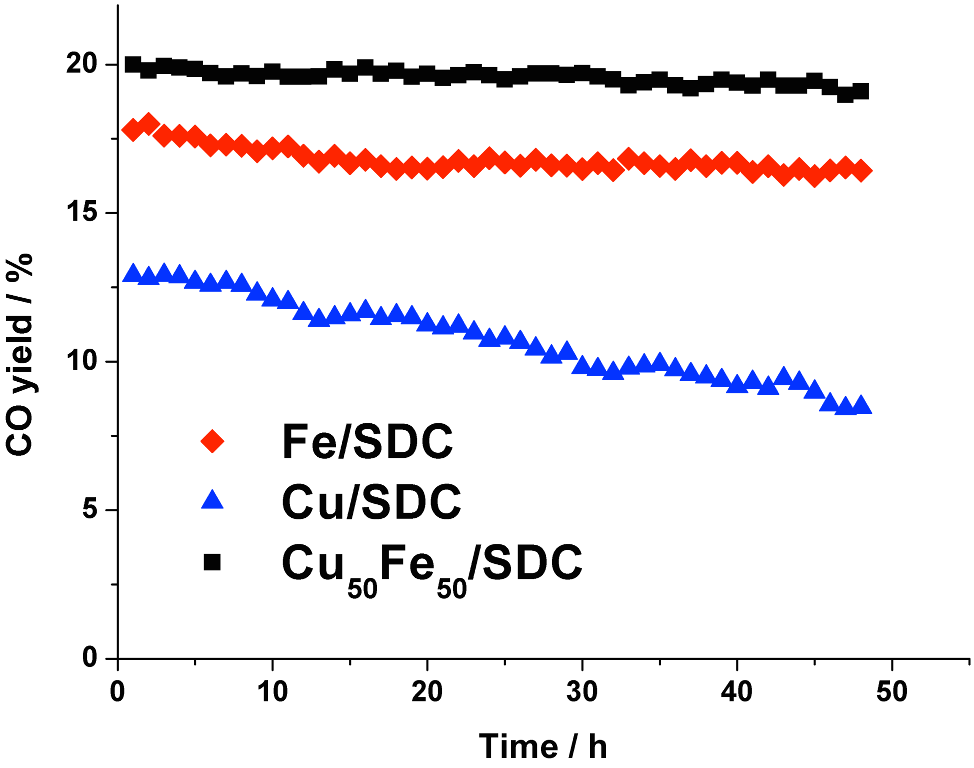

Fig. 6.5: Time-on-stream behaviour of 5 wt.% Fe_3O_4, Cu, and $Cu_{50}Fe_{50}$ supported on SDC at 550°C. Space velocity = 1020000.51 h^{-1}, $P_{H2}=P_{CO2}$= 2kPa, balance He, F = 100 $mL.min^{-1}$

Supported Cu/SDC catalyst considerably deactivated at 550°C with reaction time. The deactivation of Cu indicates a multistage process with deactivation rapidly elevating after 10 hours. As for Fe_3O_4/SDC, the initial CO yield was ~18% and this value dropped to ~ 16% within 20 hrs. Thereafter the catalytic activity was stable with an error of ±1% for the next 28hrs. The decrease in the catalytic activity of Fe_3O_4/SDC can be attributed to the reductive environment of the RWGS reaction that could result in the excessive reduction of Fe_3O_4.

As shown in Figure 6.5, $Cu_{50}Fe_{50}$/SDC exhibited higher stability over a 48-hour period compared to Cu/SDC and Fe/SDC. A slight decrease in CO yield from ~20% to ~19% can be noted over $Cu_{50}Fe_{50}$ after 48 hours of reaction at 550°C. Increased thermal stability of $Cu_{50}Fe_{50}$ compared to Cu can be assigned to the addition of Fe, which has a higher melting point (1535°C) compared to Cu (1083°C). Moreover, the close contact between Fe to Cu nanoparticles prevents Cu from sintering [213]. In addition, Fe has a great propensity for oxidation and hence, the oxygen species released on Cu would interact with Fe rather than Cu resulting in enhanced stability of $Cu_{50}Fe_{50}$. It is important to note that the oxidized Cu species eventually result in catalyst deactivation in RWGS reaction. Moreover, the rate of the formation of oxidized copper (Cu_2O) is higher than that of its reduction by H_2 [200]. Thus, the content of oxidized Cu is on the rise with reaction time and can be lowered by the addition of Fe. Everything considered, despite the slightly higher catalytic activity of Fe/SDC up to 550°C, $Cu_{50}Fe_{50}$/SDC had a superior performance in terms of catalytic stability compared to Fe and Cu catalysts supported on SDC.

6.4 Methane Production

SDC-supported Fe_3O_4, Cu and $Cu_{50}Fe_{50}$ were compared in terms of CH_4 selectivity in the range of 300 – 600°C at H_2/CO_2 ratio of 1. Figure 6.6 shows CH_4 selectivity of these catalysts measured using on-line mass spectrometer.

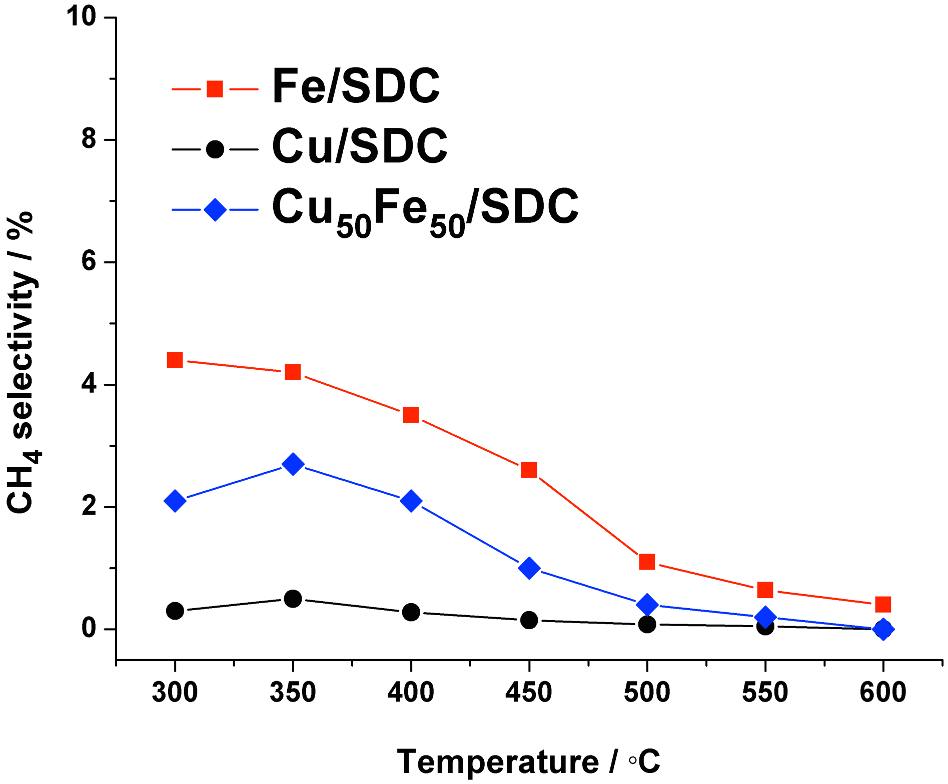

Fig. 6.6: Selectivity to CH_4 as a function of temperature over 5 wt.% Fe_3O_4, Cu and $Cu_{50}Fe_{50}$ catalysts supported on SDC. Space velocity = 1020000.51 h^{-1}; $P_{H2}=P_{CO2}$= 2kPa, balance He, F = 100 mL.min^{-1}

The analysis demonstrated that CH_4, as the main by-product of the RWGS reaction, was formed over Fe_3O_4/SDC and $Cu_{50}Fe_{50}$/SDC catalysts, especially below 500°C. Moreover, the intensity of H_2 peak on MS spectra over Fe_3O_4/SDC was lower compared with other evaluated catalysts below 500°C. This is attributed to higher H_2 consumption due to the formation of CH_4 in of SDC-supported Fe_3O_4 catalyst.

Nonetheless, Fe_3O_4/SDC was the most active catalyst up to 500°C compared to other catalysts, since the amount of unreacted CO_2 was the lowest. From 550°C and beyond, $Cu_{50}Fe_{50}$/SDC exhibits more catalytic activity as confirmed by higher CO yield and lower unreacted CO_2 values. It is important to note (Fig. 6.6) that the Fe_3O_4/SDC catalyst became highly selective to CO as of 500°C since the amount of CH_4 yield was marginal.

Cu-SDC catalyst showed negligible amounts of CH_4 by-product within the reaction temperatures. In this case, the only observed components were He, CO_2, H_2, H_2O and CO. Similar observations have been reported in the literature regarding the selectivity of Cu [97]. It is worth noting that the amount of unreacted CO_2 detected over Cu/SDC was considerably higher compared with Fe_3O_4/SDC, implying that the conversion of CO_2 was lower in Cu/SDC. In addition, Figure 6.6 demonstrates negligible CH_4 selectivity over Cu/SDC catalyst. Therefore, it can be deduced that the overall catalytic activity of Cu is lower than that of Fe_3O_4. On the other hand, $Cu_{50}Fe_{50}$ /SDC showed selectivity to CH_4 at 450°C and below; however, CH_4 selectivity of $Cu_{50}Fe_{50}$ was less than Fe_3O_4/SDC. Formation of a surface rich in Cu may be a reason for higher selectivity of $Cu_{50}Fe_{50}$/SDC to CO as opposed to Cu.

6.5 Conclusions

Cu, Fe_3O_4 as well as Cu_xFe_{1-x} (x= 50 and 95 at.%) were synthesized using a polyol method and were deposited on conductive supports (SDC, CeO_2 and YSZ). Their catalytic performance was investigated in RWGS reaction in the temperature range of 300-600°C. SDC showed a better promoting effect on the RWGS activity of Fe_3O_4 and Cu catalysts compared to CeO_2 and YSZ. The activity of Fe_3O_4/SDC was considerably higher compared to Cu/SDC. The higher activity of Fe_3O_4/SDC can be attributed to the reducibility of both oxides, which enhances the redox ability of the catalyst. Nevertheless, the activity of Fe_3O_4/SDC did not reach the equilibrium conversion and it needed to be further improved.

$Cu_{50}Fe_{50}$/SDC showed a higher catalytic activity compared to Fe_3O_4/SDC above 550°C; however, its activity was slightly lower than Fe_3O_4 below 500°C. Moreover, $Cu_{95}Fe_5$/SDC showed a comparable activity to Cu/SDC. The RWGS activity of $Cu_{50}Fe_{50}$/SDC is 25% at 600°C that requires an improvement in order to reach the equilibrium conversion of 39%.

Furthermore, Fe_3O_4/SDC catalyst had considerably higher catalytic stability in comparison to Cu/SDC. Time-on-stream measurements over SDC-supported $Cu_{50}Fe_{50}$, Fe_3O_4 and Cu catalysts indicate a noticeable decrease in the RWGS activity of Cu within 48 hours of exposure to 550°C. The stability of the SDC-supported catalysts decreased in the order of $Cu_{50}Fe_{50}$ > Fe > Cu. Copper proved itself as an inefficient catalyst at high temperatures due to its poor thermal stability. However, a major enhancement in the catalytic stability of Cu was observed with respect to $Cu_{50}Fe_{50}$/SDC. It is significant to note that despite the very low catalytic activity and stability of Cu in RWGS reaction, its selectivity to the formation of CH_4 was negligible.

Chapter 7: Pt- and Ru-based Nanoparticles for RWGS Reaction

7.1 Introduction

Design and optimization of active, selective and stable Pt and Ru-based catalysts for RWGS reaction is the key aim of this chapter. Many studies indicate that the RWGS activity of Pt and Ru catalysts can be markedly enhanced by using partially reducible metal oxides supports [98]. As discussed in Chapter 5, ionic conductivity of metal oxides including SDC, CeO_2, YSZ and Fe_2O_3 contributes considerably in promoting RWGS activity. It was shown that the oxide supports are directly involved in the RWGS reaction mechanism mainly due to their ion (O^{2-}) conductivity.

Pt and Ru have shown promising catalytic performances in RWGS reaction. Ru and Pt are reduction promoter metals, which can induce higher reducibility to ionic conductive supports and subsequently improve their catalytic performance in RWGS reaction [214]. It has been reported that the RWGS activity of these metals is strongly dependent on the type of the support material [215]. For instance, the activity of Ru/Fe_2O_3 is reported to be notably good for the RWGS reaction, while Ru/Al_2O_3 shows activity for CO_2 methantion [216]. In another study, performance of Pt nanoparticles supported on TiO_2 catalysts showed improvement in RWGS reaction compared to those supported on Al_2O_3 [217]. Therefore, it is of the greatest significance to study the effect of the support on the catalytic properties of Ru and Pt nanoparticles.

Ru is active in RWGS reaction and is markedly less expensive than Pt; however, its employment in RWGS reaction is challenging since Ru also shows high activity in CO_2 methantion reaction [218]. It has been reported that the Ru particle size comes into play in determining its selectivity in CO_2 hydrogenation. Basinka et al found that the mean size of Ru is a decisive factor in its RWGS catalytic activity [64]. It is proposed that small Ru nanoparticles with sizes around 1-2 nm are incapable of CO_2 dissociation, which is the first step of methane formation [219]. Eckle et al. also reported that $Ru/\gamma\text{-}Al_2O_3$ catalysts with Ru particle sizes of 2nm exhibit high CO yield than those containing larger Ru particles [220].

Therefore, synthesis and development of selective Ru catalysts is very important for our purpose to inhibit the methanation reaction.

Optimization of the properties of Ru and Pt metals is achievable through using a suitable synthetic technique, selecting appropriate substrates as well as alloying with other metals. Synthesis of bi-metallic catalysts can contribute to exceeding the catalytic properties of individual components since both the composition and atomic ordering would be effective [221]. For instance, Caglayan et al. found high CO selectivity in PtNi/γ-Al_2O_3 catalysts in spite of the high selectivity of Ni metal for CH_4 formation [222].

In this chapter mono-metallic Pt, Ru nanoparticles and bi-metallic nanoparticles, namely Ru_xPt_{1-x} (x =50 at.%) as well as Ru_xFe_{1-x} (x = 80 and 90 at.%) were synthesized using polyol method and then deposited on conductive supports (SDC, CeO_2, YSZ and Fe_2O_3) and subsequently tested for RWGS. The RWGS activity of supported Ru, Pt and $Ru_{50}Pt_{50}$ has been investigated in the temperature range of 300 - 600°C using a feed composition consisting of CO_2 and H_2 in equimolar ratio as described in details in Chapter 3. All catalysts were subjected to a 1h pre-reduction step in a flow of 5 wt.%H_2/He at 450°C in order to induce an appropriate activation for RWGS reaction. The purpose of the present work is to study the effect of the type of the metal oxide support and its correlation with the activity of the metals. Furthermore, an investigation into the effect of the metal loading on the activity of Ru and Pt metals was undertaken.

7.2 Effect of the Support on CO Yield over Ru and Pt Noble Metals

Ruthenium and platinum nanoparticles with average particle size of 1.1 and 1.9 nm were deposited on the conductive metal oxide supports (SDC, CeO_2, YSZ and Fe_2O_3) , with the metal loading of 1 wt.%. Figure 7.1 shows the CO yield of supported Ru and Pt nanoparticles in the temperature range of 300 -600°C.

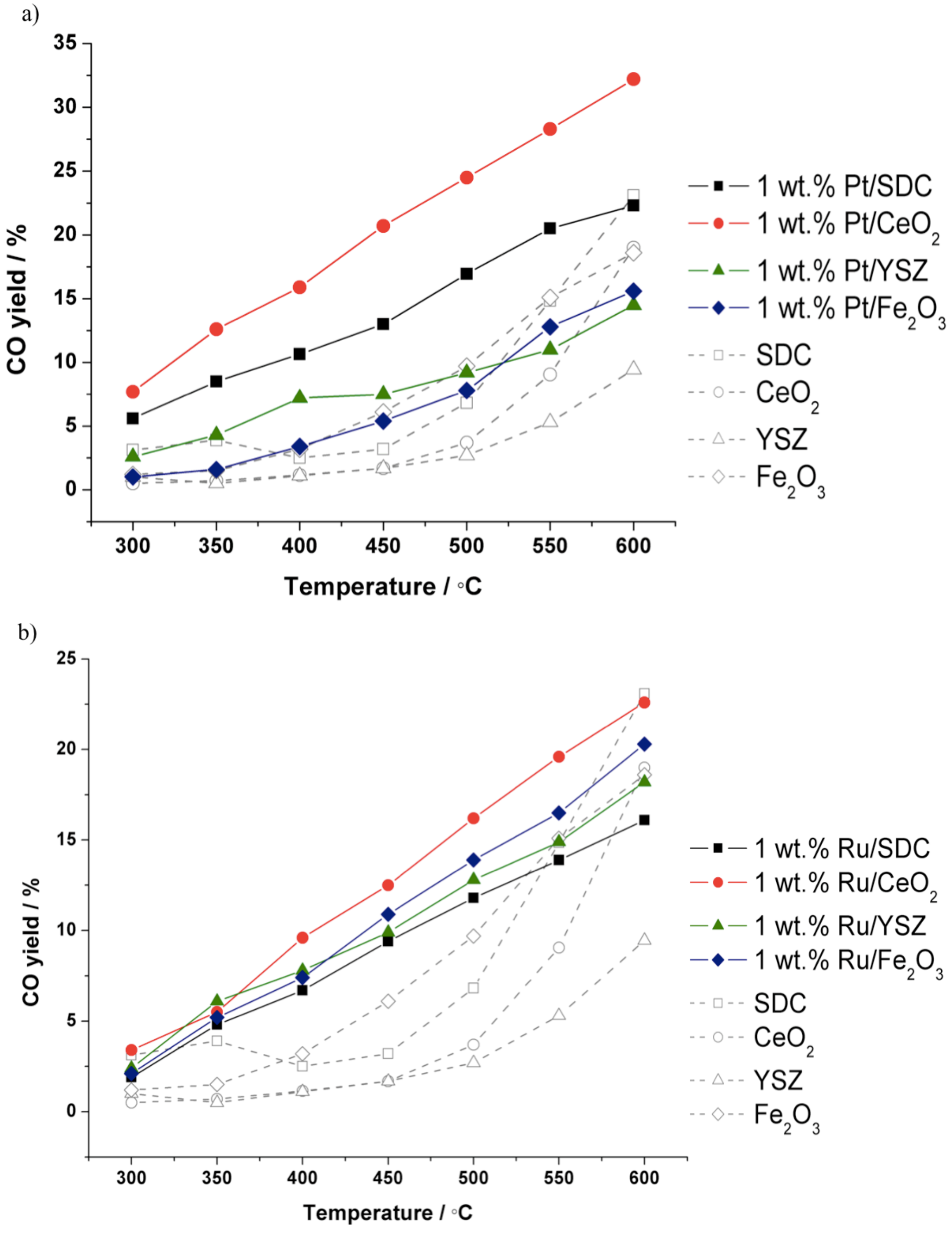

Figure 7.1: CO yield over Ru and Pt nanoparticles supported on YSZ, CeO_2, SDC and Fe_2O_3. Dashed lines represent CO yield over blank YSZ, CeO_2, SDC and Fe_2O_3. Space velocity = 1020000.51h^{-1}; P_{H2}=P_{CO2}= 2kPa, balance He; F = 100 mL.min^{-1}

SDC had the best stand-alone performance due to its high ion conductivity. However, Figure 7.1 shows that CeO_2 has the best promoting effect on both Ru and Pt catalysts, which indicates that higher ionic conductivity and reducibility of SDC did not come into play to induce higher activity to Ru/SDC and Pt/SDC catalysts. In addition, as discussed in Chapter 5, YSZ has lower catalytic activity in RWGS reaction compared to CeO_2 and SDC due to its lower reducibility. Surprisingly, the deposition of 1 wt.% Ru metal evidently had a profound impact on the activity of YSZ support, because Ru/YSZ shows (Fig 7.1) a higher catalytic activity compared to Ru/SDC.

According to Figure 7.1b the promotion effect of the supports in Ru catalysts follows the sequence of $CeO_2 > Fe_2O_3 \geq YSZ \geq SDC$, with Ru/SDC and Ru/YSZ showing comparable activities up to 450°C. Moreover, Ru/Fe_2O_3 apparently outperforms Ru/SDC above 400°C. According to the activity order of the supports for Ru catalysts, it can be deduced that the reducibility of the support is not the most determining factor in promoting the RWGS activity of Ru nanoparticles, since SDC appeared to underperform less reducible supports.

It has been reported that supplying Ru with high amounts of O^{2-} drives the CO_2 hydrogenation reaction towards higher CH_4 yields [199]. This can explain the lower activity of Ru/SDC compared to CeO_2- and YSZ-supported Ru catalysts as a result of higher oxygen conductivity of SDC. It can be inferred that the presence of excessive oxygen species can give rise to the oxidation of Ru and subsequently its deactivation in RWGS reaction. The oxidized Ru bonds markedly weaker with CO and thus larger surface areas would be available for H_2 to dissociatively adsorb and promote CH_4 formation [223]. Therefore, high RuO_x/Ru ratio plays a major role in reducing the RWGS activity of Ru catalysts. Higher activity of Ru/CeO_2 compared to other supported Ru catalysts can be explained by the effect of CeO_2 on Ru. CeO_2 as an oxygen capacitor can either withdraw or provide oxygen. Therefore, superior performance of Ru/CeO_2 might be related to the ability of CeO_2 to deprive oxygen of RuO_x, forming metallic Ru.

Figure 7.1a shows that for Pt catalysts, the activity of the supports is in the sequence of $CeO_2 > SDC > YSZ > Fe_2O_3$. CeO_2 demonstrates the best promotion effect in spite of its lower ion conductivity compared with SDC. Figure 7.1a displays that except for CeO_2, the activity of the rest of the metal oxide supports increases with reducibility. Reducibility of oxide supports is a decisive factor in promoting the activity of Pt catalysts in RWGS reaction [217]. However, the nature of the support is also determining. On the basis of the results, the affinity between Pt and CeO_2 is markedly high, but the incorporation of sm^{3+} ions in CeO_2, leads to its reduction as evidenced by the lower activity of Pt/SDC.

Moreover, it is important to note that the specific surface area of CeO_2 (SSA = 30-50 m^2/g) is higher than that of SDC (SSA = 35 m^2/g) and YSZ (SSA = 13 m^2/g). This gives rise to lower Ru dispersion in Ru/YSZ. Considering the low surface area of YSZ as well as the higher activity of Ru/YSZ compared to Ru/SDC, it can be concluded that the surface area of the support and the Ru dispersion are not mainly influential in the activity of supported Ru catalysts. In contrast, the activity of Pt catalysts appeared to be associated with the specific surface area of the supports, exhibiting better performance with the support's specific surface increasing, as confirmed by the activity order of CeO_2 > SDC > YSZ. It is evident that Pt, like Ru, promotes the oxide supports such as CeO_2 and SDC. However, unlike Ru, the promotion effect of Pt on YSZ is apparently marginal. Thus, we concluded that the activity of Pt catalysts depends strongly not only on the nature of the support, but also on Pt dispersion.

Dispersion values of Ru and Pt metals in 5 wt.% Ru and Pt catalysts supported on CeO_2 and SDC were measured using the CO titration technique (see Chapter 3, section 3.4.4). The results of metal dispersions as well as their corresponding particle sizes are reported in Chapter 4. Results summarized in Table 7.1 clearly show that Ru and Pt catalysts supported on SDC exhibit lower metal dispersion compared to those supported on CeO_2. This is reasonable with respect to the higher specific surface area of CeO_2 (SSA = 30-50 m^2/g) compared to SDC (SSA = 35 m^2/g) as well as the smaller crystallite size of CeO_2 (d_p = 15-30 nm) as opposed to SDC (d_p = 30-50 nm).

Table 7.1: Ru and Pt dispersion and size in CeO_2- and SDC-supported catalysts *From

Catalyst metal	Colloidal particle size from TEM (nm)	Supported catalyst	Dispersion from CO titration method (%)	Supported particle size (nm)*
Ru	1.1	5 wt.% Ru / CeO_2	21	2.7
		5 wt.% Ru / SDC	13	3.3
Pt	1.9	5 wt.% Pt / CeO_2	43	3.1
		5 wt.% Pt / SDC	22	3.6

(Eq. 4.4): $d_{nm} = \frac{600 \, . \, M_w}{\rho \, . \, dispersion \, (\%) . \, a \, . \, N_a}$

It is apparent that Pt dispersion has dropped nearly by half from Pt/CeO_2 to Pt/SDC, while less difference in dispersion values can be observed for Ru catalysts. We found that the activity of Ru catalysts is independent of metal dispersion, whereas the opposite holds true for Pt catalysts. Therefore, improved performance of Pt over CeO_2 compared to Pt on SDC can be also explained by its higher dispersion.

It has been reported that YSZ mostly exhibits ionic conductivity and its electronic conductivity is negligible compared to mixed ionic-electronic conductive ceria-based oxides [224], implying that the interaction between the support and the metal is mainly interfacial due to the surface oxygen vacancies present in ion-conducting YSZ. Furthermore, it has been reported than the ionic conductivity of CeO_2 at 750°C compares with that of YSZ at 1000°C [225]. This indicates that the promoting effect of ion conductivity is lower in YSZ. Therefore, it can be inferred that the interaction of Pt with YSZ is weaker than that of Pt with CeO_2 and SDC. Hence, the lower Pt dispersion over YSZ combined with weaker metal-support interaction results in the inferior performance of Pt/YSZ compared to other investigated Pt catalysts. However, it is presumable that with respect to Ru/YSZ, a specific metal support interaction between Ru and ZrO_2 might be responsible for the improved performance of YSZ-supported Ru. It has been reported that Ru/ZrO_2 catalysts inhibit excessive chemisorption of H_2 upon their reduction at high temperatures [226], which indicates lower CH_4 selectivity and subsequently higher CO yields in Ru/YSZ.

Despite the very low catalytic stability of Fe_2O_3, as earlier reported in Chapter 5, we found it significant to evaluate the activity of Pt and particularly Ru metals on Fe_2O_3 due to the high activity of Fe_2O_3 in RWGS reaction. Activity of noble metals essentially depends on the nature of the support and Ru/Fe_2O_3 is known as an effective RWGS catalytic system due to a specific metal-support interaction [64]. High activity of Ru/Fe_2O_3 shown in Figure 7.1b may be also attributable to the reduction of the support to Fe_3O_4 due to the pre-reduction step. Figure 7.1b displays the higher activity of Fe_2O_3 compared to SDC in Ru catalysts. In contrast, the activity of Pt/Fe_2O_3 is less than that expected for Fe_2O_3 alone. This might be related to low Pt dispersion over Fe_2O_3 as well as weak interaction between the metal and the support. This finding is in agreement with the literature, indicating that ferric oxide-supported platinum catalysts are inactive systems for catalyzing the RWGS reaction [93].

It is important to note that except for Fe_2O_3-supported Ru and Pt catalysts, the activity of all catalysts showed considerably high and reproducible behaviour for three successive heating cycles in the temperature range of 300 – 600°C. Figure 7.2 demonstrates the performance of 5 wt.% Ru, Pt and catalysts supported on Fe_2O_3 at three different catalytic cycles.

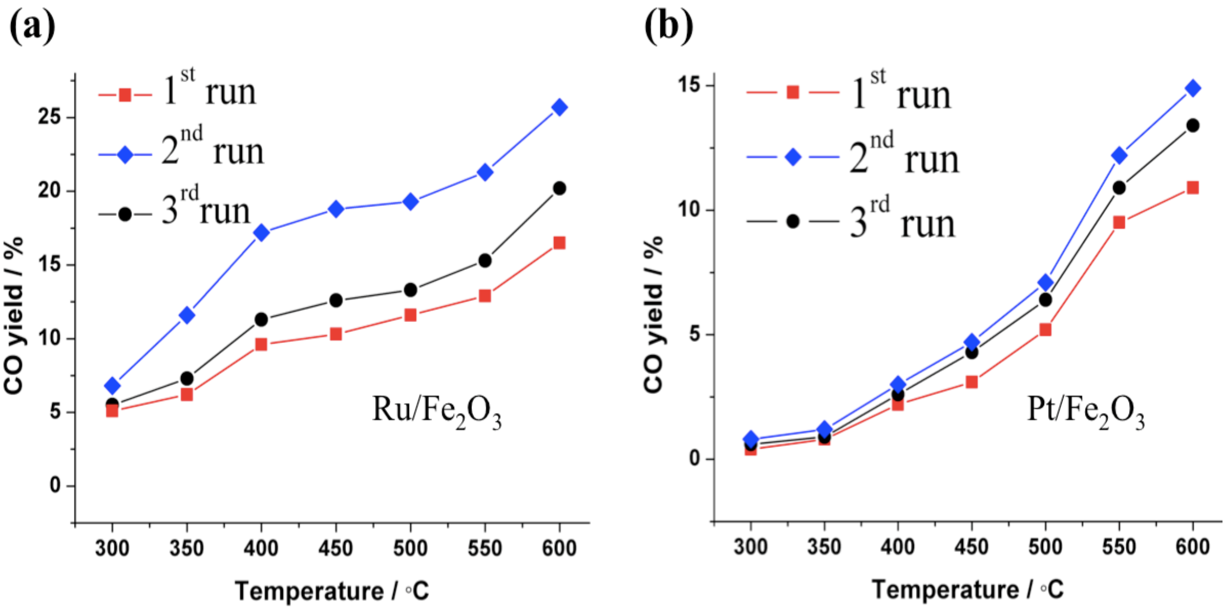

Fig. 7.2: Stability of 1 wt.% (a) Ru, (b) Pt catalysts supported on Fe_2O_3 in three consecutive catalytic runs. Space velocity = 8628805.584 h^{-1}, P_{H2}=P_{CO2}= 2kPa, balance He, F = 100 mL.min^{-1}

Although the activity of the Pt/Fe_2O_3 catalyst is significantly lower, but the catalytic measurements (Fig. 7.2) indicate that it shows higher stability and reproducibility when compared to Ru/Fe_2O_3. The last temperature cycle over Ru/Fe_2O_3 indicates ~10% of reduction in CO yield, while the light-off curves observed for Pt/Fe_2O_3 are more stable with only ~ 4% decrease in CO yield particularly above 500°C.

All things considered, Figure 7.1 clearly denotes that the nature of the support is of great importance for both Ru and Pt metals. Experimental results indicate that the catalyst activity may derive from electronic metal-support interaction (EMSI). It is notable that electron transfer is favourable on CeO_2 support as a mixed ionic-electronic conductive material. The charge transfer between Ru, Pt and CeO_2 can modify the catalytic performance of the metals and it would subsequently increase the oxidation-reduction cycles, leading to the promotion of RWGS reaction. The electronic effects of the metal-support interaction between CeO_2 and noble metals have been studied extensively and proved to be effective in shift reactions [227]. Use of CeO_2 ensured a high selectivity of Ru to CO formation. Furthermore, it can be observed that CeO_2 is by far the most active support for Ru and Pt catalysts, with Pt/CeO_2 of 1 wt.% of metal loading showing a higher promotion effect towards the RWGS activity when compared to 1 wt.% Ru/CeO_2.

7.3 Effect of the Metal Loading on CeO_2-supported Ru and Pt Nanoparticles

The effect of the content of metal nanoparticles has been studied over CeO_2-supported Pt and Ru catalysts with nominal metal contents of 1, 5 and 10 wt. % on CeO_2. The results of the metal loading are shown in Figure 7.3.

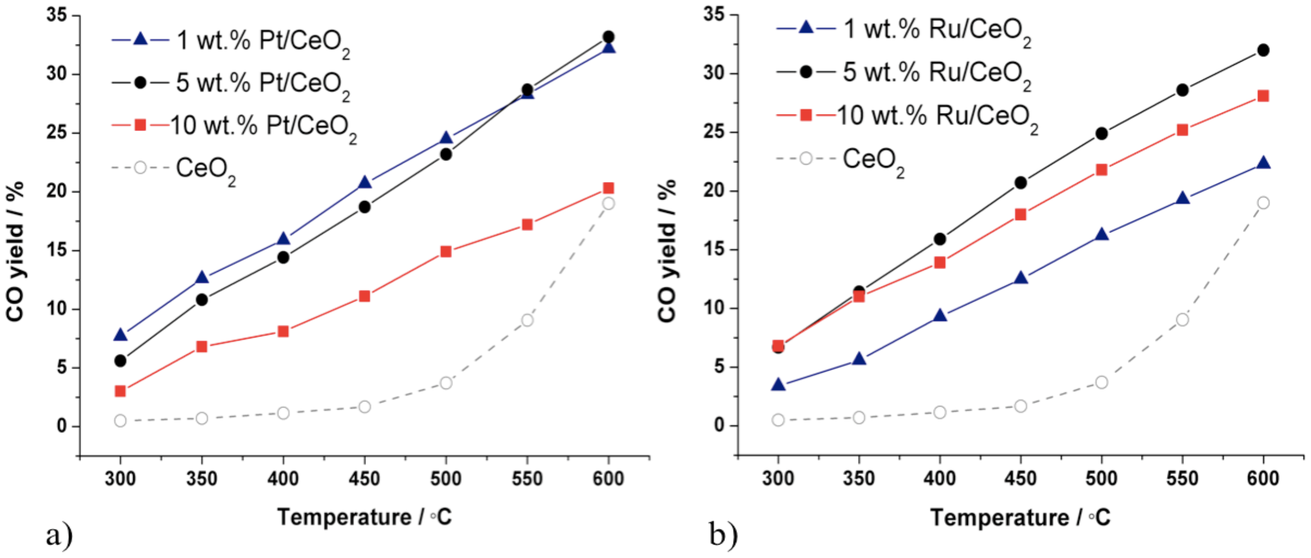

Fig. 7.3: CO yield over (a) Pt and (b) Ru catalysts supported on CeO_2 with varying Ru and Pt loads. Dashed line represents the CO yield over blank CeO_2. Space velocity = 855846.86h^{-1}; P_{H2}=P_{CO2}= 2kPa, balance He; F = 100 mL.min^{-1}

Evidently, increasing the metal loading from 1 wt.% to 10 wt.% drastically deteriorates the activity for Pt catalysts, whereas it appears to favour the RWGS activity of Ru. It is believed that Ru and Pt catalysts at relatively high metal loadings of 10 wt.% are expected to exhibit lower metal dispersion compared to metal loadings of 1 wt.%. Interestingly, this reinforces our previous finding stating that the RWGS activity of Pt catalysts is strongly sensitive to metal dispersion, while the activity of Ru catalysts shows no dependence on Ru dispersion. Figure 7.2 demonstrates that the catalytic activity of Pt/CeO_2 decreases with increasing metal loading, with the 10 wt.% Pt catalyst showing the lowest CO yield. In addition, the activity of 1 wt.% Pt is marginally higher than that of 5 wt.% Pt. Thus, we conclude that Pt catalysts having small metal loadings (5 wt.% and below) are more effective for promoting the RWGS reaction.

As displayed in Figure 7.2, a marked enhancement in activity can be observed by changing the Ru content from 1 wt.% to 5 wt.%, indicating that Ru content of 1 wt.% is definitely not the optimum metal loading in Ru/CeO_2 catalysts. In addition, the difference in the catalytic activity of Ru/CeO_2 catalysts having 5 and 10 wt.% of Ru loading appeared to be negligible, with 5 wt.% Ru/CeO_2 showing an outperformance.

Altogether, the results demonstrate (Fig. 7.2) that the activity of CeO_2-supported Ru and Pt catalysts is in agreement with the order of 5 wt.% Ru ≈ 1 wt.% Pt > 5 wt.% Pt > 10 wt.% Ru > 1 wt.% Ru > 10 wt.% Pt, with 5 wt.% Ru and 1 wt.% Pt showing comparable activities. Catalytic activity of Pt/CeO_2 was proved to be associated with metal loading, with 1wt.% Pt showing the best catalytic performance. Unlike Pt/CeO_2, we found no correlation between the RWGS activity of Ru catalysts and the metal loading, however, 5 wt.% of Ru metal was determined as the optimal loading for Ru/CeO_2 catalysts. It is notable that 5 wt.% Ru/CeO_2 ($d_p = 2.7$) and 1 wt.% Pt/CeO_2 ($d_p = 1.9$) more or less perform similarly and 5 wt.% Pt/CeO_2 ($d_p = 3.8$) shows a slightly lower RWGS activity.

According to TEM results shown in table 7.1, the colloidal particle sizes of Ru and Pt are 1.1 nm and 1.9 nm, respectively. STEM micrograph of 1 wt.% Ru/CeO_2 (shown in Chapter 3) indicated that the particle size of Ru remained unchanged after its dispersion on CeO_2. In addition, the particle size of 1 wt.% Pt/CeO_2 also did not undergo a change with respect to the colloidal Pt particle size. However, increase in particle size was evident after the deposition of 5 wt.% Ru and 5 wt.% Pt nanoparticles over the support, with 5 wt.% Ru/CeO_2 and 5 wt.% Pt/CeO_2 having respectively particle sizes of 2.7 nm and 3.8 nm.

Interestingly, results confirm that in spite of the smaller particle size of Ru than Pt in 1 wt.% CeO_2-supported catalysts, 1 wt.% Pt is significantly more active than 1 wt.% Ru. This implies that smaller particle size of Ru and hence its higher surface area did not come into play to induce higher activity to Ru catalysts in RWGS reaction. Higher activity of 1 wt. % Pt/CeO_2 than 1 wt.% Ru/CeO_2 might be also attributable to an electronic interaction between the Pt metal and the CeO_2 support in RWGS reaction. It has been found that additional CeO_2 expansion as a representative of more oxygen vacancies was mainly observed for Pt/CeO_2 as opposed to Ru/CeO_2 [223]. Therefore, one of the factors responsible for the superior behaviour of Pt with low metal loading could be its stronger reducing effect on CeO_2. We conclude that the promotion effect of Pt on CeO_2 is significantly greater than that of Ru.

Nonetheless, relatively high Pt loadings (e.g. 10 wt.%) dramatically worsen catalyst activity due to lower metal dispersion. Thus, Pt catalysts with low metal content (< 5 wt.%) deposited on CeO_2 are effective systems for catalyzing RWGS reaction, whereas higher Ru content is required in order to provide a catalytic activity similar to that of 1 wt.% Pt/CeO_2.

Hence, it can be inferred that besides the kind of the support, metal content is likewise a decisive parameter.

7.4 Activity and Stability of Ru_xPt_{1-x} (x = 50 at.%) and Ru_xFe_{1-x} (x= 80 and 90 at.%) Catalysts for RWGS Reaction:

As earlier shown in Figure 7.1, CeO_2-supported Ru and Pt catalysts exhibit higher catalytic performance due to the effective metal-support interaction. Moreover, it was found that the metal loading of 5 wt.% showed the best catalytic effect in RWGS reaction for Ru catalysts. Additionally, we found that Pt/CeO_2 catalysts of 1 and 5 wt.% of loading exhibited similar activities, with 1 wt.% Pt having a slightly improved RWGS performance.

Herein, Ru-Pt nanoparticles having nominal composition of $Ru_{50}Pt_{50}$ were synthesized as described in Chapter 3. The nominal metal loading of 5 wt.% was held constant in order to favour the RWGS activity of both Ru and Pt metals in the bi-metallic Ru-Pt systems. The equilibrium conversion curve was obtained using Microsoft Excel as described in Chapter 5. Figure 7.4 summarizes the catalytic activity of 5 wt.% $Ru_{50}Pt_{50}$ catalysts over various metal oxide supports.

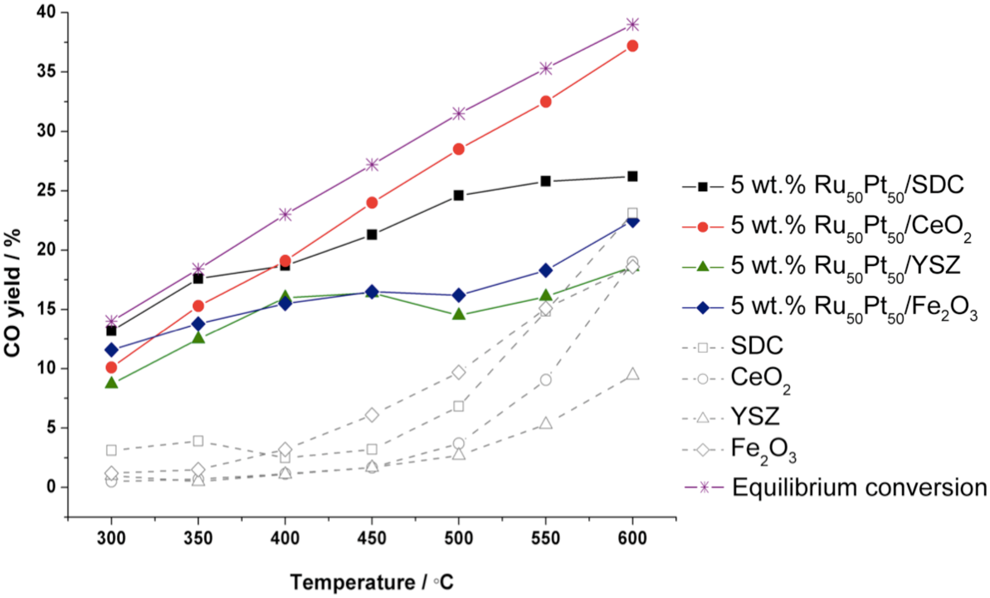

Fig. 7.4: CO yield over 5 wt.% $Ru_{50}Pt_{50}$ nanoparticles supported on YSZ, CeO_2, SDC and Fe_2O_3. Dashed lines represent CO yield over blank YSZ, CeO_2, SDC and Fe_2O_3. Space velocity = 1020000.51h^{-1}; P_{H2}=P_{CO2}= 2kPa, balance He; F = 100 mL.min^{-1}

The characterization results shown in Chapter 4, confirm the formation of Ru-Pt alloy with an average particle size of 1.6 ± 0.5 nm. Interestingly, Figure 7.4 denotes that the promotion effect of 5 wt.% $Ru_{50}Pt_{50}$ on the oxide supports to a great extent follows the trend observed for 1 wt.% Pt catalysts (Fig. 7.1). The catalytic activity of the supports varies in the order of CeO_2 > SDC > Fe_2O_3 > YSZ. It is notable that the metal-support interaction between CeO_2 and $Ru_{50}Pt_{50}$ is more effective compared with $Ru_{50}Pt_{50}$ and other oxides.

Figure 7.5 shows the three consecutive catalytic measurements carried out over 5 wt.% $Ru_{50}Pt_{50}$ catalysts deposited on CeO_2, SDC and Fe_2O_3.

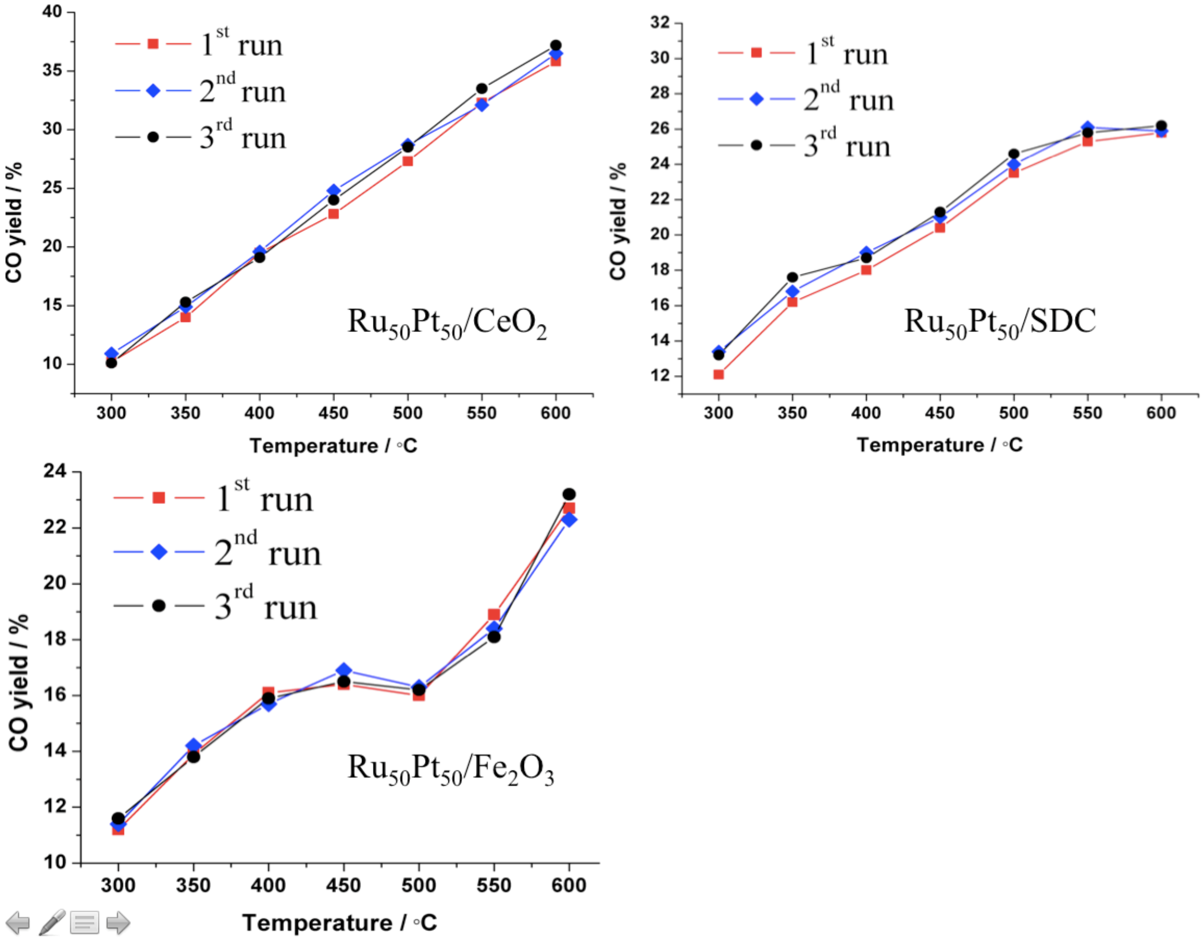

Fig. 7.5: Stability of 5 wt.% $Ru_{50}Pt_{50}$ catalysts supported on CeO_2, SDC and Fe_2O_3 in three consecutive catalytic runs. Space velocity = 8628805.584 h^{-1}, P_{H2}=P_{CO2}= 2kPa, balance He, F = 100 $mL.min^{-1}$

The light-off curves for $Ru_{50}Pt_{50}/Fe_2O_3$ clearly denote its good stability to several catalytic runs as well as the reproducibility of the catalytic measurements. Considering the progressive decrease in the catalytic activity of Ru/Fe_2O_3 (Fig. 7.2), the promoting effect of $Ru_{50}Pt_{50}$ on the catalytic stability of Fe_2O_3 is stronger compared to Ru. The overall performance of $Ru_{50}Pt_{50}/Fe_2O_3$ is better compared to Fe_2O_3-supported Ru and Pt catalysts.

The IR spectroscopy results previously demonstrated in Chapter 4 show that there is more resemblance between the IR spectra of Ru and $Ru_{50}Pt_{50}$ with respect to the adsorbed CO bands. This could result from the presence of higher atomic percentage of Ru than its nominal value, which was calculated as 50 at.%. However, according to the results we conclude that $Ru_{50}Pt_{50}/CeO_2$ exhibits a good performance, possessing mostly Pt features.

Figure 7.4 shows that except for Fe_2O_3, the reducibility and the specific surface area of the supports were determining on the performance of Ru-Pt catalysts. As displayed in Figure 7.1, despite the lower ion conductivity of Fe_2O_3, the catalytic activity of Ru/Fe_2O_3 was outstanding, showing a similar performance to Ru/CeO_2. In contrast, Pt/Fe_2O_3 exhibited a far inferior catalytic activity. $Ru_{50}Pt_{50}/Fe_2O_3$ demonstrated (Fig. 7.5) an improved behavior with respect to Pt/Fe_2O_3, mainly attributable to the promoting effect of Ru. However, It has been observed later in Chapter 5 (Fig. 5.5) that the catalytic stability of Fe_2O_3 markedly deteriorates as a result of long-term exposure to H_2 environments at elevated temperatures, while other conductive oxides (SDC, CeO_2 and YSZ) showed high stability.

Despite the good catalytic performance of 5 wt.% Ru/CeO_2 (Fig. 7.3), the RWGS equilibrium conversion of CO_2 was not reached within the range of 300 – 600°C over this catalyst. Therefore, we attempted to incorporate Fe in order to investigate its promotion effect on the activity of Ru/CeO_2. Thus, Ru-Fe catalysts with nominal compositions of $Ru_{90}Fe_{10}$ and $Ru_{80}Fe_{20}$ were tested. Figure 7.6 compares the catalytic activity of 5 wt.% mono- and bi-metallic Ru- and Pt-based catalysts supported on CeO_2 as a function of temperature.

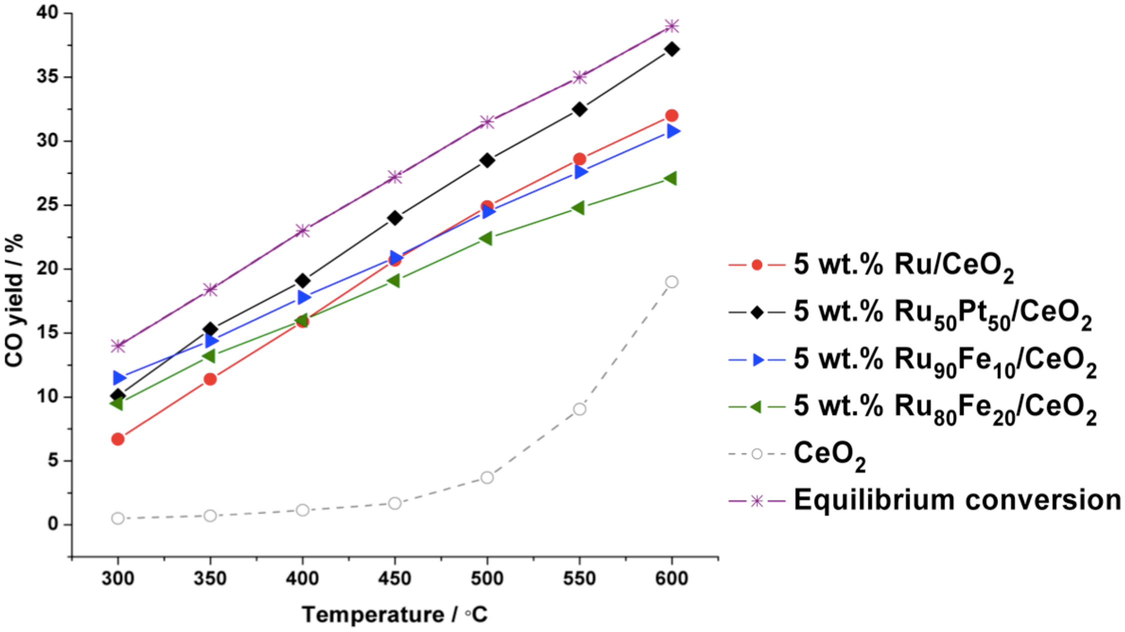

Fig. 7.6: CO yield on 5 wt.% Ru, Ru$_{50}$Pt$_{50}$, Ru$_{90}$Fe$_{10}$, and Ru$_{80}$Fe$_{20}$ catalysts deposited on CeO$_2$. Dashed line represents the CO yield over blank CeO$_2$. Space velocity = 855846.86 h$^{-1,}$ P$_{H2}$=P$_{CO2}$= 2kPa, balance He, F = 100 mL.min^{-1}

It is evident that 5 wt.% Ru$_{50}$Pt$_{50}$ has a superior performance compared to all the other CeO$_2$-supported catalysts of the same metal loading. The CO$_2$ conversion to CO over 5 wt.% Ru$_{50}$Pt$_{50}$/CeO$_2$ exhibited the closest value to the amount of CO$_2$ conversion at thermodynamic equilibrium. It is notable that the combined activity is greater than the sum of that attributable to the Ru and the Pt catalysts alone. Therefore, it can be concluded that the synergism between Ru, Pt and CeO$_2$ resulted in the superior performance of the 5wt.% Ru$_{50}$Pt$_{50}$/CeO$_2$ catalyst. Enhanced activity of Pt-Ru/CeO$_2$ may be ascribed to the ability of the bi-metallic Ru$_{50}$Pt$_{50}$ system to inhibit the dissociation of CO bond, which leads to the hydrogenation of carbon to methane.

Moreover, results displayed in Figure 7.6 indicate that the promoting effect of Fe in Ru$_{90}$Fe$_{10}$/CeO$_2$ catalyst is mostly evident at lower temperatures, while no difference in catalytic activity can be observed above 450°C when compared to Ru/CeO$_2$. It is noted that with respect to Ru-Fe catalysts, increasing Fe content from 10 wt.% to 20 wt.% gives rise to a reduction in activity at high temperatures, while showing slightly enhanced initial activity at 300°C. It is apparent that the initial activity of Ru$_{90}$Fe$_{10}$ is higher than that of Ru$_{80}$Fe$_{20}$. The increase in CO yield at lower temperatures can be associated with higher CO selectivity induced by Fe, as CO_2 methanation mainly occurs up to 450°C.

It has been reported that Ru-Fe oxide catalysts can be remarkably active for RWGS reaction, depending on the iron oxide phase. Furthermore, it has been shown that the reduction of iron oxides follows the steps: Fe(III) to Fe(II,III) to Fe(II) [92]. Improved catalytic activity of $Ru_{90}Fe_{10}/CeO_2$ might be attributed to the facilitation of partial reduction of Fe_2O_3 to Fe_3O_4 at lower temperatures due to the presence of Ru [64]. More importantly, it could be associated with the prevention of Ru oxidation by Fe, as we found oxidized Ru to be highly selective towards CH_4 formation. Nevertheless, this promoting effect was not observed for Ru-Fe/CeO_2 catalysts with higher Fe loading (20 wt.%). It was also found that the subjection of Ru-Fe catalysts to 5 wt.%H_2/He pretreatment decreases the CO yield.

Figure 7.6 indicates that the activity of 5wt.% CeO_2-supported catalysts, in the range of 300 - 600°C, is in the order of $Ru_{50}Pt_{50} > Ru_{90}Fe_{10} \geq Ru > Ru_{80}Fe_{20}$. An interesting remark is that despite the high CH_4 selectivity of Ru reported in the literature [219], the synthesized Ru-based catalysts supported on CeO_2 showed high RWGS activity, which was further promoted by the addition of Pt and Fe metals. We earlier demonstrated the effect of some crucial parameters including the nature of the metal and the support, metal loading and dispersion as well as the promoting effect of each of the components. Nevertheless, another explanation for the improved performance of Ru-based catalysts can be the particle size of metals ranging from 1.1 nm to 2.7 nm. It is noticeable that particles of small size result in an increase in the number of surface active sites, indicating an enhancement in the interaction between the metal and the support. Notably, the metal-support interaction was found to be highly decisive in the RWGS activity of Ru and Pt metals.

Figure 7.7 shows the time-on-stream behaviour of 5 wt.% Ru, Pt and $Ru_{50}Pt_{50}$ catalysts supported on CeO_2 for 48 consecutive hours at 550°C.

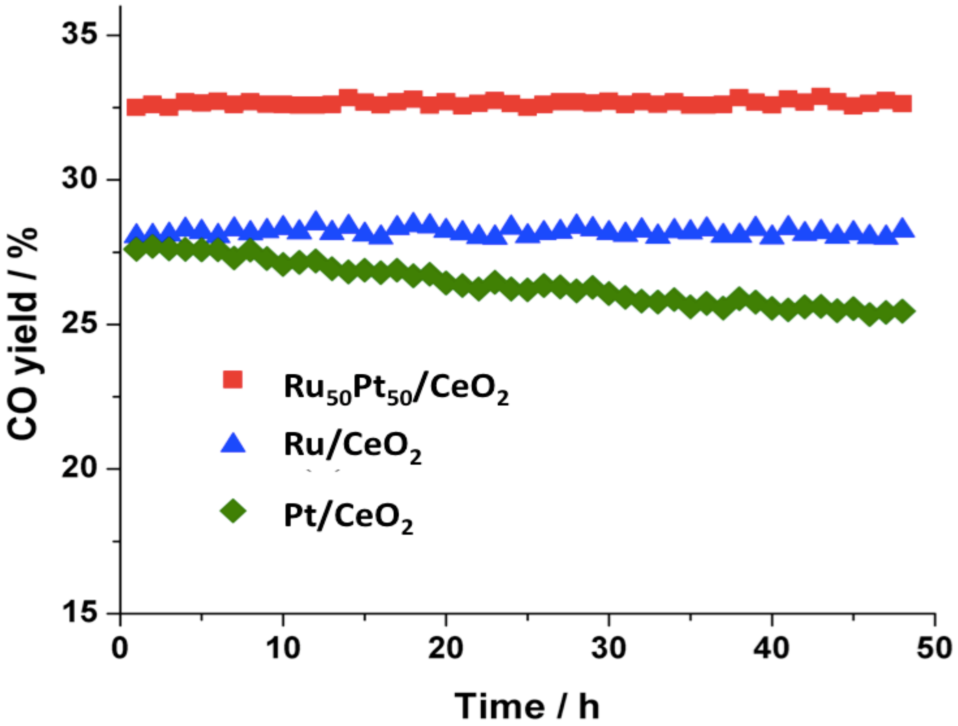

Fig. 7.7: Time-on-stream behaviour of 5 wt.% (a) $Ru_{50}Pt_{50}$, (b) Ru, and (c) Pt at 550°C supported on CeO_2. Space velocity = 855846.86 h^{-1}, $P_{H2}=P_{CO2}$= 2kPa, balance He, F = 100 mL.min^{-1}

Figure 7.7 shows that the catalytic activity of 5 wt.% Pt/CeO_2 was not fully maintained after 48 hours of operation. In contrast, 5 wt.% Ru/CeO_2 is markedly stable over the same period. Moreover, it indicates that $Ru_{50}Pt_{50}$/CeO_2 was highly active for the time-on-stream of 48h, while CO_2 conversion over Pt/CeO_2 dropping ~ 2-3% of CO yield. However, Pt and CeO_2 showed an effective interaction for promoting the RWGS reaction.

As discussed earlier in this chapter, Pt had a higher reducing effect on CeO_2 as opposed to Ru, implying that Pt was more effective at facilitating the reduction of CeO_2 at lower temperatures. It has been reported that CeO_2 can be irreversibly reduced as a result of long-term exposure to H_2 and subsequently it can face sintering [228]. Moreover, the reduction of surface ceria occurs at around 450°C, while its bulk reduction can be observed at roughly 750°C [229]. Presumably, the decrease in Pt/CeO_2 catalytic activity may be explained by the excessive reduction of CeO_2 resulting from the addition of 5 wt.% Pt. Furthermore, it has been reported that the deterioration of the catalytic activity of Pt/CeO_2

might be the carbon deposits resulting from CO disproportionation that can potentially occur on partially reduced ceria surfaces [230].

7.5 Effect of H_2/CO_2 Ratio on CO Yield

The effect of reactant composition and total feed flow rate were investigated in RWGS reaction for 5 wt.% $Ru_{50}Pt_{50}/CeO_2$. The effect of the total feed flow rate was studied by changing the reactant flow rates between 100 mL/min to 400 mL/min. Higher flow rates were achieved by diluting the feed stream with helium. Figure 7.8 shows the light-off curves of 5 wt.% $Ru_{50}Pt_{50}$ supported on CeO_2 at different total feed flow rates.

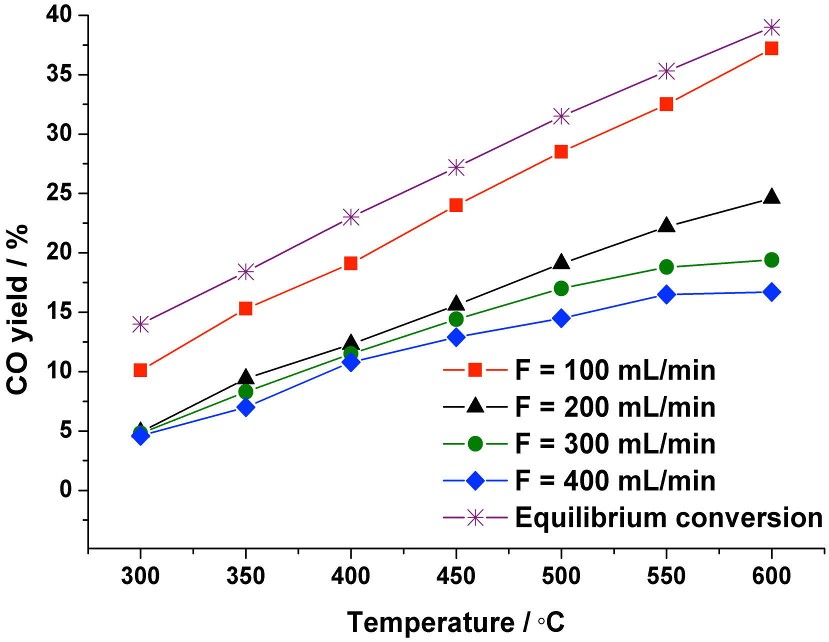

Fig 7.8: CO yield at varying total feed flow rates over 5 wt.% $Ru_{50}Pt_{50}/CeO_2$ in the temperature range of 300°C – 600°C. Space velocity = 855846.86 h^{-1} - 3423387.44h^{-1}; P_{H2} = 1-4kPa, P_{CO2}= 2kPa, balance He

It is noticeable that all the light-off curves shown in Figure 7.8 correspond to the same amount of the CeO_2-supported Ru-Pt catalysts. Therefore, gas hourly space velocity (GHSV) as a representative of the total flow rate to the total catalyst volume can considerably impact the reaction yield. Increasing the total flow rate from 100 to 400 $mL.min^{-1}$ results in the GHSV varying from 855846.86h^{-1} to 3423387.44h^{-1}. It is notable that increasing the total flow rate and subsequently GHSV values significantly reduces the catalyst performance. It is expected that the residence time of the reactants decrease with increasing the total feed flow rate. A shorter residence time is associated with higher GHSV values, which indicates that the contact time between the catalyst and the reactants is shorter. Moreover, Figure 7.8 demonstrates a drastic decrease in CO yield from 100 to 200 mL.min^{-1}, while as of 200 mL.min^{-1} the variation in the catalyst activity is marginal, showing a slight reduction in CO yield from F=300 mL.min^{-1} to F=400 mL.min^{-1}. It can be concluded that the total flow rate of 100 mL.min^{-1} is more favourable for the RWGS reaction.

The H_2/CO_2 ratio was kept constant at 1 throughout this study in order to inhibit the CO_2 methanation reaction. It is crucial to investigate the effect of the H_2 concentration to investigate the catalytic performance under different reactant compositions. Figure 7.9 indicates the effect of the partial pressure of H_2 on the catalytic activity of 5 wt.% $Ru_{50}Pt_{50}/CeO_2$ at different H_2/CO_2 ratios in the range of 1 to 4.

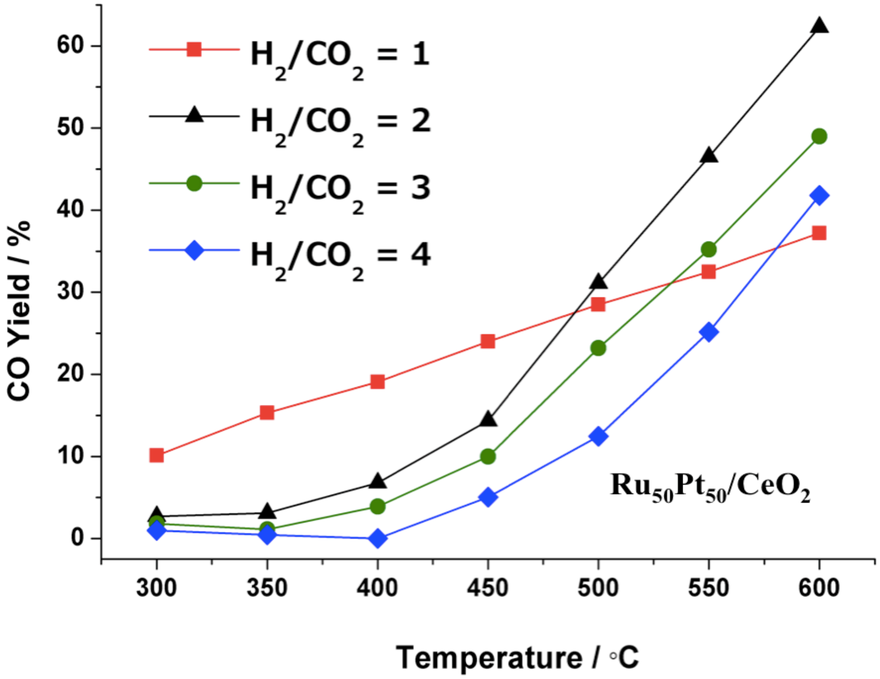

Fig. 7.9: CO yield at varying H_2 partial pressures over 5 wt.% $Ru_{50}Pt_{50}/CeO_2$ in the temperature range of 300 – 600°C. Space velocity = 855846.86 h^{-1}; P_{H2} = 1 - 4kPa, P_{CO2}= 2kPa, balance He; F = 100 mL.min^{-1}

This study indicates that the yield of CO is strongly dependent on H_2 partial pressure. Due to the exothermic nature of the CO_2 methanation reaction, high H_2/CO_2 ratios greatly favour the formation of CH_4 at lower temperatures. Figure 7.9 clearly denotes that CO_2 methanation at $H_2/CO_2 = 2$ is predominant up to 450°C, while a markedly improved RWGS activity is evident as of 500°C. However, by increasing H_2/CO_2 from 2 to 4, CH_4 formation is facilitated at higher temperatures. As for H_2/CO_2=4, CH_4 formation can be noted up to 550°C, with only ~5% of enhancement in RWGS activity at 600°C. In addition, as previously discussed, the irreversible reduction of CeO_2 can result in its catalytic deactivation. Therefore, It is also presumable that at high H_2/CO_2 ratios, the overall catalytic activity of the $Ru_{50}Pt_{50}/CeO_2$ might be deteriorated because of the over-reduction of CeO_2 due to exposure to high H_2 concentrations. In general, it is evident that CO yield progressively decreases upon the introduction of higher amounts of H_2, showing a negative reaction order with respect to H_2 particularly from 300 - 450°C for all reactant ratios.

7.6 Methane Production

CeO_2-supported Ru- and Pt-based catalysts showed good RWGS activities, however, it is significant to evaluate their selectivity for CO formation, as it is likewise a decisive factor for the practical application of these catalysts. Therefore, the formation of methane and other potential by-products such as methanol was carefully monitored using the Mass Spectrometer (MS). The on-line MS analysis indicated that no CO_2 conversion was visible due to the empty reactor up to 600°C. Moreover, according to the findings demonstrated earlier in Chapter 5, CH_4 was the only by-product formed over pure CeO_2 in the temperature range of 300 – 600°C. Figure 7.10 displays the CH_4 selectivity of CeO_2-supported Ru- and Pt-based catalysts.

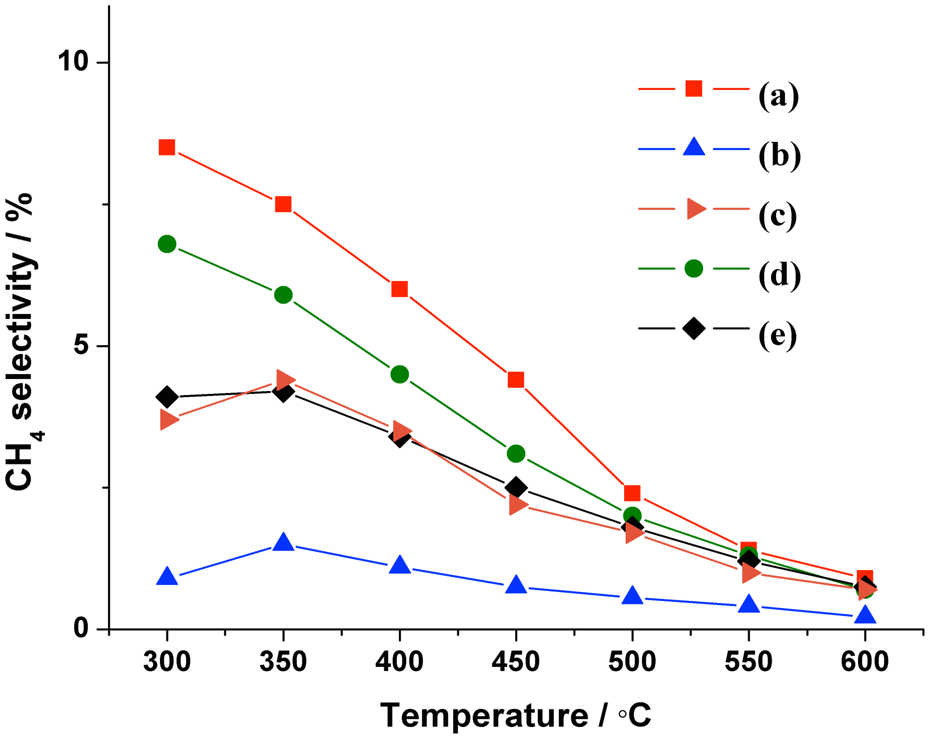

Fig. 7.10: Methane selectivity over 5 wt.% (a) Ru, (b) Pt, (c) $Ru_{50}Pt_{50}$, (d) $Ru_{90}Fe_{10}$, and (e) $Ru_{80}Fe_{20}$ catalysts supported on CeO_2 from 300°C to 600°C. Space velocity = 855846.86 h^{-1}; P_{H2}=P_{CO2}= 2kPa, balance He, F = 100 $mL.min^{-1}$

Mass spectrometry results over Ru/CeO_2 exhibited low amount of unreacted CO_2 at all reaction temperatures, implying the good catalytic activity of Ru/CeO_2. Nevertheless, Figure 7.10 denotes that the Ru catalyst has the highest activity for the formation of CH_4 compared to all the other CeO_2-supported catalysts. An interesting finding observed with respect to Ru/CeO_2 was the formation of trace amounts of methanol up to 500°C, while no methanol has been detected over the rest of the catalysts. As for Pt/CeO_2, it was noted that despite the higher amount of unreacted CO_2 as opposed to Ru/CeO_2, only trace amounts of CH_4 were identified. Interestingly, it can be concluded that the conversion of CO_2 is higher in Ru/CeO_2 compared to Pt/CeO_2; however, the Ru catalyst shows more CH_4 selectivity.

The addition of Fe dopant (Fig. 7.8) exhibited a minimal effect on the catalytic activity with respect to CeO_2-supported $Ru_{90}Fe_{10}$ and $Ru_{80}Fe_{20}$ catalysts, in particular at high temperatures. However, MS analysis shown in Figure 7.10 shows that the amount of CH_4 yield decreases owing to the addition of Fe. We found that the amount of CH_4 yield was associated with Fe content, exhibiting lower methane yield for $Ru_{80}Fe_{20}$ compared to $Ru_{90}Fe_{10}$. As discussed later in this chapter, oxidized Ru species exhibit higher selectivity to CO_2 methanation rather than CO formation. Higher CO selectivity of Ru-Fe catalysts can be attributable to the prevention of Ru oxidation as a result of Fe incorporation. The released oxygen from the reaction can readily interact with Fe, as it has higher propensity for oxidation in comparison to Ru.

Notably, the generation of CH_4 was comparable over $Ru_{50}Pt_{50}$ and $Ru_{80}Fe_{20}$ catalysts, while the amount of unreacted CO_2 was higher in the case of $Ru_{80}Pt_{20}$. As for $Ru_{50}Pt_{50}$, low CH_4 selectivity might derive from the interaction between Ru and Pt by which a stronger bond between the metal and CO would be formed and subsequently less H_2 would be dissociatively adsorbed to cleave the C−O bond. Everything considered, the CH_4 selectivity of the CeO_2-supported catalysts is in conformity with the order of Ru $>$ $Ru_{90}Fe_{10}$ $>$ $Ru_{80}Fe_{20}$ $\approx$ $Ru_{50}Pt_{50}$ $>$ Pt.

7.7 Conclusions

Ru- and Pt-based catalysts were prepared using a modified polyol reduction method. Their RWGS catalytic performance on conductive oxides, namely SDC, CeO_2, YSZ and Fe_2O_3 showed a great dependence on the nature of the support. In the case of Pt catalysts, the reducibility of the support, electronic metal-support interaction (EMSI) and metal dispersion were important factors in determining its catalytic performance in RWGS reaction. The activity of Pt catalysts decreased according to the order: $Pt/CeO_2 > Pt/SDC > Pt/YSZ > Pt/Fe_2O_3$. Pt showed great affinity for CeO_2, however, the incorporation of Sm_2O_3 affected EMSI, which resulted in a lower RWGS activity in Pt/SDC. In the case of Ru catalysts, it was found that their RWGS activity was independent of metal dispersion and was mainly defined by metal-support interaction (MSI). As for Ru catalysts, the RWGS activity varied according to the order of $Ru/CeO_2 > Ru/Fe_2O_3 \geq Ru/YSZ \geq Ru/SDC$. Higher ionic conductivity of SDC gave rise to the formation of oxidized Ru species (RuO_x), which reduced the RWGS activity of Ru catalysts. Ru, Pt and $Ru_{50}Pt_{50}$ metals showed better activity when deposited on CeO_2. This was attributed to the stronger MSI between Ru,Pt and CeO_2.

All the evaluated catalysts except for Ru/Fe_2O_3 and Pt/Fe_2O_3 showed high catalytic stability during three consecutive catalytic runs. It was noted that in spite of the higher activity of Ru/Fe_2O_3, it had a considerably lower catalytic stability compared to Pt/Fe_2O_3. The catalytic instability of Fe_2O_3 has been previously reported in Chapter 5. Therefore, Pt was more effective in stabilizing Fe_2O_3 oxide compared to Ru. One of the major advantages of $Ru_{50}Pt_{50}$ system was inducing high catalytic stability to Fe_2O_3, with only 5 wt.% of metal loading. Moreover, Pt/CeO_2 showed a slight reduction in catalytic activity during a 48-hour stability measurement, whereas CeO_2-supported Ru and $Ru_{50}Pt_{50}$ maintained their activities. Therefore, it was found that it is important to stabilize Pt/CeO_2 catalysts for long-term RWGS experiments.

The RWGS activity of Pt/CeO_2 catalysts is not only a function of support's nature, but also metal loading and dispersion. Low Pt loadings, e.g. 1-5 wt.%, significantly favoured the RWGS activity, while high Pt loadings, e.g. 10 wt.%, deteriorated the RWGS performance. On the other hand, no specific correlation was observed between the activity and metal content in Ru/CeO_2 catalysts. However, low metal loadings, e.g. 1 wt.%, and relatively high metal loadings, e.g. 10 wt.%, appeared to be less favourable compared to the loading of 5 wt.% in Ru/CeO_2 catalysts. 5 wt.% Ru and 1 wt.% Pt catalysts supported on CeO_2 showed higher CO yields.

In the case of CeO_2-supported catalysts with 5 wt.% of metal loading, $Ru_{50}Pt_{50}$ showed the best RWGS activity compared to Ru, Pt, $Ru_{90}Fe_{10}$ and $Ru_{80}Fe_{20}$ catalysts. The high activity of 5wt.% $Ru_{50}Pt_{50}$/CeO_2 was attributed to synergism between Ru, Pt and CeO_2. Moreover, addition of Fe gave rise to higher CO yields up to 450°C with respect to RuFe catalysts. However, increase in the content of Fe from 10 at.% to 20 at.% resulted in lower CO yield at high temperatures. Therefore, $Ru_{90}Fe_{10}$ had a better performance compared to $Ru_{80}Fe_{20}$. Pt exhibited less intermediate activity compared to other CeO_2-supported catalysts, while Ru/CeO_2 showed the highest CH_4 selectivity. However, the overall catalytic activity of Ru/CeO_2 was higher than that of Pt/CeO_2, as the amount of unreacted CO_2 identified over the Ru catalyst was noticeably lower. In the case of Ru_xFe_{1-x} (x= 80 and 90 at.%), it was observed that the CH_4 selectivity decreases with increasing the Fe loading. Nevertheless, higher Fe loading resulted in lower catalytic activity with respect to $Ru_{80}Fe_{20}$. Despite the very high catalytic activity of 5 wt.% $Ru_{50}Pt_{50}$/CeO_2, it did not fully approach the equilibrium conversion. However, 38 % of CO yield can be observed at 600°C, which is only 1% lower than the equilibrium conversion.

Chapter 8: Conclusions and Recommendations

8.1 Summary of the Findings

This chapter presents a summary of the main findings of the thesis with respect to the project objectives:

Objective I: Synthesis and characterization of mono- and bi-metallic nanoparticles based on Cu, Fe, Ru and Pt

Objective II: Investigation of the catalytic performance of three different types of commercial metal oxides (ionically conductive, mixed ionic-electronic and non-conductive) in RWGS reaction for further use as catalytic support

Objective III: Investigation of the catalytic performance of non-noble metal nanoparticles including Cu, Fe and CuFe supported on active metal oxides for RWGS reaction

Objective IV: Investigation of the catalytic performance of noble metal nanoparticles including Ru, Pt, RuPt, RuFe supported on active metal oxides for RWGS reaction

Objective I: The synthesis of mono- and bi-metallic nanoparticles of non-noble metals (Cu,Fe) and noble metals (Ru,Pt) was successfully performed using a polyol synthesis method. This method proved to be facile and effective in controlling the size of metal nanoparticles by adjusting the pH of the solution using NaOH. Therefore, size-controlled nanoparticles were obtained without the need for any stabilizers, e.g. PVP (polyvinylpyrrolidone). Ru, Pt, Ru_xPt_{1-x} (x = 50 at%) and Ru_xFe_{1-x} (x= 80 and 90 at%) were synthesized in ethylene glycol (EG, bp =197.3 °C) at the reflux temperature of 160°C. On the other hand, non-noble metals, namely Cu, Fe and Cu_xFe_{1-x} (x=50 and 95 at%) were synthesized in triethylene glycol (TrEG, bp =285°C) at the reflux temperature of 280°C. The initial pH of all the solution was 11-12 before reflux. One of the novel features of this work was the synthesis of magnetite (Fe_3O_4) in TrEG with the particle size of 8.3 nm.

Objective II: The catalytic performance of three different types of commercial metal oxides (ionically conductive, mixed ionic-electronic and non-conductive) was evaluated in RWGS reaction from 300 - 600°C in order to choose the most active substrates for the deposition of metal nanoparticles. Non-conductive oxides, namely gamma-alumina (γ-Al_2O_3) and carbon (C) showed poor catalytic activity and stability. On the other hand, conductive oxides, namely samarium-doped ceria (SDC), ceria (CeO_2), yttria-stabilized zirconia (YSZ), titania (TiO_2) and hematite (Fe_2O_3) showed improved activity. However, none of the oxides approached the equilibrium conversion under the reaction conditions described in Chapter 3. The RWGS activity of conductive oxides decreased according to the order: SDC$>$ Fe_2O_3 $>$ CeO_2 $>$ YSZ $>$ TiO_2. Samarium-doped ceria showed superior RWGS activity mainly due to its higher oxygen ion (O^{2-}) conductivity and increased the CO_2 to CO conversion to 23% at 600°C (equilibrium conversion at 600°C = 39%). The good activity of Fe_2O_3 was attributed to its partial reduction to magnetite (Fe_3O_4). However, Fe_2O_3 showed a considerable deactivation after 24 hours of RWGS experiment at 550°C, while SDC, CeO_2 and YSZ fully maintained their catalytic activity. Moreover, the Mass Spectrometry (MS) analysis on SDC, CeO_2, YSZ and γ-Al_2O_3 demonstrated that YSZ had the lowest CH_4 selectivity in the temperature range of 300 - 600°C and γ-Al_2O_3 showed the highest CH_4 selectivity below 450°C. Furthermore, it indicated that SDC had the highest catalytic activity compared to the other evaluated oxides because it showed the lowest amount of unreacted CO_2 at all temperatures. SDC, CeO_2, YSZ and Fe_2O_3 were chosen as catalyst support due to their better RWGS activity. However, the catalytic stability of Fe_2O_3 needs to be improved through adding metal promoters.

Objective III: The catalytic performance of mono- and bi-metallic Cu- and Fe_3O_4-based catalysts namely, Cu, Fe_3O_4 and Cu_xFe_{1-x} (x= 50 and 95 at.%) was evaluated in the RWGS reaction using conductive oxides (SDC, YSZ and CeO_2) as supports. SDC showed a higher catalytic improvement on the RWGS activity of non-noble metals. This was mainly attributed to the high ion conductivity of SDC. Higher activity of Fe_3O_4 catalysts compared to Cu was evident over all conductive supports. Furthermore, Fe_3O_4/SDC showed higher catalytic activity compared to other SDC-supported catalysts, namely $Cu_{95}Fe_5$ and $Cu_{50}Fe_{50}$ up to 500°C due to the reducibility of the metal as well as the support. It is notable than $Cu_{50}Fe_{50}$/SDC had a better performance above 550°C, showing 25% of CO yield at 600°C. Higher activity of $Cu_{50}Fe_{50}$/SDC can be also associated with the strong oxide-oxide interaction. Moreover, $Cu_{50}Fe_{50}$ was more stable. $Cu_{95}Fe_5$ showed a similar activity to Cu;

however, unlike Cu, it was stable to several catalytic measurements. Cu/SDC showed a low catalytic activity and stability. Its catalytic stability appeared to improve considerably with respect to $Cu_{50}Fe_{50}$/SDC. Higher RWGS activity was found to be related to the Fe loading in the case of evaluated metals.

Objective IV: It was found that the RWGS catalytic performance of precious metals including Ru, Pt, Ru_xPt_{1-x} (x= 50 at.%) and Ru_xFe_{1-x} (x= 80 and 90 at.%) was mainly determined with respect to their interaction with the support. SDC, CeO_2, YSZ and Fe_2O_3 were the catalyst supports studied within this section. The RWGS activity of all the catalysts was higher when deposited on CeO_2. Beside the metal-support interaction (MSI), the activity of Pt was found to be dependent on metal dispersion, while the activity of Ru was mostly defined by MSI and no dependence on metal dispersion was found. An interesting observation was that in spite of the higher ion conductivity and reducibility of SDC compared to CeO_2, its promoting effect was less on the RWGS activity of Ru and Pt metals. In the case of Ru catalysts, Ru/Fe_2O_3 showed a comparable activity to Ru/CeO_2, while Pt/Fe_2O_3 had a considerably low activity. It was noted that Ru/Fe_2O_3 outperformed Ru/SDC. The only drawback of the Ru/Fe_2O_3 catalyst was its lower catalytic stability compared to Pt/Fe_2O_3 and $Ru_{50}Pt_{50}$/Fe_2O_3. Moreover, it was found that lower Pt loadings, e.g. 1 wt.%, and higher Ru loadings, e.g. 5 wt.%, favour the RWGS reaction. Due to the sensitivity of the Pt catalysts to metal dispersion, a remarkable reduction in catalytic activity was observed for Pt catalysts with 10 wt.% of loading. The $Ru_{50}Pt_{50}$/CeO_2 outperformed all other catalysts in terms of activity and stability. Thus, it was concluded that Ru and Pt acted synergistically to promote the RWGS reaction. On the other hand, Ru-Fe catalysts were capable of increasing the yield of CO up to 450°C compared to Ru. $Ru_{90}Fe_{10}$ showed a comparable activity to $Ru_{50}Pt_{50}$ in the temperature range of 300-450°C. Furthermore, it was found that the CH_4 selectivity of Ru-Fe catalysts decreases with increasing the Fe loading. However, $Ru_{80}Fe_{20}$ showed a lower activity as opposed to Ru above 450°C.

8.2 Future Work and Recommendations

It is significant to investigate the metal-support interaction (MSI) especially in the case of noble metals, because their catalytic activity in RWGS reaction is mainly determined by MSI. Moreover, the catalyst dispersion needs to be enhanced in order to prevent agglomeration and subsequent catalyst deactivation. This can be done through using another metal deposition technique such as acetone precipitation.

More characterization techniques, namely Inductively Coupled Plasma (ICP), transmission electron microscopy (TEM), X-ray photoelectron spectroscopy (XPS) and X-ray diffraction (XRD) measurements should be carried out in order to investigate the metal loading, particle size, surface composition and also identify the crystalline phase of bi-metallic catalysts.

Further study should be done in order to improve the RWGS performance of Cu and Fe_3O_4 catalysts in terms of catalytic activity and stability. Addition of other stabilizers such as potassium (K) and chromia (Cr_2O_3) can be investigated. Reducibility of the oxide support played an important role in the RWGS activity of Cu and Fe-based catalysts. Therefore, supports with higher ionic conductivity and reducibility can be used. Moreover, the cu- and Fe-based catalysts were prepared using 5 metal weight percent. The effect of the metal loading needs to be examined in order to find an optimum loading.

Ru and Pt-based catalysts showed promising results in RWGS reaction; however, it is very significant to reduce the loading weight of Ru and Pt on supports and further improve their catalytic activity. Non precious metals can be added in different compositions and tested in RWGS reaction. It is also interesting to synthesize particles with different sizes using the polyol synthesis method in order to study the effect of the particle size and distribution on RWGS activity.

References

[1] H. Arakawa, M. Aresta, J.N. Armor, M.A. Barteau, E.J. Beckman, A.T Bell, J.E. Bercaw, C. Creutz, E. Dinjus, D.A. Dixon. 2001, Chem. Rev., Vol. 101, p. 953-960

[2] P. Kaiser, R.B. Unde, C. Kern, A. Jess. 2013, Chem. Eng. Tech, Vol. 85, pp. 489-499.

[3] D. Anthoff, R.J. Nicholls. Hamburg University, Research Unit in Sustainibility and Global Warming (R.S.J.). Hamburg : s.n., 2009.

[4] N.L. Bindoff, J. Willebrand, V. Artale, A. Cazenave, J. Gregory, S. Gulev. Cambridge University Press. Cambridge : s.n., 2007.

[5] K.E. Trenberth, P.D. Jones, P. Ambenic, R. Bojariu, D. Easerling, A. Klein, D. Zhai. Cambridge : Cambridge University Press, 2007.

[6] *World Energy Outlook.* International Energy Agency (IEA). Paris : s.n., 2010.

[7] J. Hawecker, J. Lehn, R. Ziessel. 1986, Chem. Act., Vol. 69, pp. 1990-2012.

[8] *Nat.* J. Rogeli, M. Meinshausen, R. Knutti. 2012, Vol. 2, pp. 248-253.

[9] Philips, N.A. 1996, Meterorol. Soc., Vol. 82, pp. 123-154.

[10] M. Peters, B. Kohler, W. Kuckshinrichs, W. Leitner. P. Markewitz, T.E. Muller. 2011, ChemSusChem, Vol. 4, p. 1261.

[11] G. Genti, G. Iaquaniello, S. Perathoner. 2011, ChemSusChem, Vol. 4, pp. 1265-1273.

[12] A.M. Schulenberger, F.R. Jonsson, O. Ingolfsson. *0244208* 2007. US Patent Appl.

[13] J.S. kim, S.B. Lee, M.J. Choi, K.W. Lee. 2006, Catal. Today, Vol. 115, pp. 228-234.

[14] H. Beech, F.P. Ragonese. *US5059738* 1990. Grant.

[15] S. Sankaranarayanan, K. Srinivasan. 2012, Ind. J. Chem, Vol. 51, pp. 1252-1262.

[16] S. Manish, R. Banerjee. 2008, Int. J. Hydr. Ene., Vol. 33, pp. 279-286.

[17] Abe, R. 2010, J. Photochem. Photobiol., Vol. 11, pp. 179-209.

[18] J. Gao, Y. Wang, Y. Ping, D. Hu, G. Xu, F. Gu, F. Su. 2012, RSC Adv., Vol. 2, pp. 2358-2368.

[19] Vanderklippe, N. *Synthetic fuel sees new life.* The globe and Mail. Calgary, 2012.

[20] E.A. Quadrelli, G. Centi, J. Duplan, S. Perathoner. 2011, ChemSusChem, Vol. 4, pp. 1194-2015.

[21]. L. Wang, S. Zhang, Y. Liu. 2008, *J. Rare Earths,* Vol. 26, pp. 66-70.

[22] E.S. Van-Dal, C. Bouallou. 2013, J. Cleaner Prod., Vol. 57, pp. 38-45.

[23] B. Todona, C. Koppold, A. Bansode, A. Irakawa, P. Rudolf Von Rohr. 2013, J. Supercritic. Flu., Vol. 78, pp. 70-77.

[24]S. Saeidi, N.A.S Amin, M.R. Rahimpour. 2014, J. CO2 Utiliz., Vol. 5, pp. 66-81.

[25] M. Khoshtinat Nikoo, N.A.S. Amin. 2011, Fuel Proc. Tech, Vol. 92, pp. 678-691.

[26] Schlogl, R. *Chemical Energy Storge.* de Gruyter. Berlin : s.n., 2012.

[27] P. Prasad, J. Bae, K. Jun, K. Lee. 2008, Catal. Surv. Asia, Vol. 12, pp. 170-183.

[28] K.G. Schulz, B. Ramos, R. Zeebe, U. Riebesell. 2009, J. Biogeosci., Vol. 6, pp. 2145-2153.

[29] Merchant, B. *Fossil fuels.* Energy, Treehugger. 2012.

[30] N. Homs, J. Toyir, P. Ramirez de la Piscina. Catalytic Processes for the Activation of CO_2. *CO_2 Utilization Techniques.*

[31] G. Centi, S. Perathoner. 2009, Catal. Today, Vol. 148, pp. 191-205.

[32] O.S. Joo, K.D. Moon, AY. Rozovskii, G.I. Han, S.J. Uhm. 1999, Ind. Eng. Chem. Res., Vol.

38 pp. 1808-1812.

[33] Miller, L. *An Alternative Route for Coal to liquid Fuel.* ExxonMobil. 2008.

[34] G.C. Chinchen, K.C. Waugh, D.A. Whan. 1986, Appl. Catal, Vol. 25, pp. 101-110.

[35] P. Panagiotopoulou, D.I. Kondarides, X.E. Verykios. 2008, Appl. catal. A:Gen, Vol. 344, pp. 45-54.

[36] G.A. Olah, A. Goeppert, G.K.S. Prakash. 2008, J. Org. Chem., Vol. 74, pp. 487-498.

[37] D. González-Quijano, W.J. Pech-Rodríguez, J.A. González-Quijano, J.I. Escalante-García, c, G. Vargas-Gutiérrez, I. Alonso-Lemus, F.J. Rodríguez-Varela. 2015, Inter. J. Hydrogen Energy, Vol. 40, pp. 17291-17299.

[38] C.V. Miguel, M.A. Soria , A. Mendes , L.M. Madeira. 2015, J. of Nat. Gas Sci. and Eng., Vol. 22, pp. 1-8.

[39] T. Riedel, M. Claeys, H. Schulz, G. Schaub, S.-S. Nam, K.-W. Jun. 1999, Appl. Catal A: Gen, Vol. 186, pp. 201-213.

[40] X. Zhang, B. Dai, A. Zhu, W. Gong, C. Liu. 2002, Catal. Today, Vol. 72, pp. 223-227.

[41] Y. Zhang, G. Jacobs, D.E. Sparks, M.E. Dry, B.H. Davis. 2002, Catal. Today, Vol. 71, pp. 411-419.

[42] W. Wei, G. Jinlong. 2010, Frontiers of Chem. Sci. and Eng., Vol. 5, pp. 2-10.

[43] J. Gao, Y. Wang, Y. Ping, D. Hu, G. Xu, F. Gu and F. Su. 2012, RSC Adv., Vol. 112, pp. 2358-2368.

[44] X. Duan, G. Qian, X. Zhou, Z. Sui, D. Chen, W. Yuan. 2011, Appl. Catal. B: Environ., Vol. 101, pp. 189-196.

[45] W. Wang, S. Wang, X. Ma, J. Gong. 2011, Chem. Soc. Rev. , Vol. 40, pp. 3703-3713.

[46] S.J. Tauster, S.C. Fung, R.L. Garten. 1978, J. Am. Chem. Soc., Vol. 100, pp. 170-175.

[47] A. Marinoiu, E. Carcadea, M. raceanu, C. Cobzaru, M. Varlam. 2013, Adv. in Environ. Agri. Sci., Vol. 101, pp. 237-241.

[48] G.C. Chinchen, K.C Waugh. 1986, J. Catal, Vol. 97, pp. 280-283.

[49] W.C. McKee, K. R. Boyd, S. J. Berger. *The US Patent. US8318112* 2007. Grant.

[50] S.W Park, O.S. Joo, K.D. Jung, H. H. Kim. 2000, Korean J. Chem. Eng., Vol. 17, pp. 719-722.

[51] J.B. Hansen, P.E. Hojlund Nielsen. *Handbook of Heterogeneous Catalysis.* 2008. pp. 2920-2949.

[52] Y. Choi, K. Futagami, T. Fujitani, J. Nakamura. 2001, Appl. Catal. A, Vol. 208, pp. 163-169.

[53] M. Saito, M. Takeuchi, T. Fujitani, J. Toyir, S. Luo, J. Wu, H. Mabuse, K. Ushikoshi, K. Mori, T. Watanabe. 2000, Appl. Organometal. Chem. , Vol. 14, pp. 763-771.

[54] T.O. Eschemanna, W. S. Lammea, R. L. Manchestera, T.E. Parmentiera, A. Cognignib, M Ronning, Krijn P. de Jong. 2015, J. of Catal., Vol. 328, pp. 130-138.

[55] Dry, M. E. 2002, Catal. Today., Vol. 71, pp. 227-241.

[56] Steven L. Suib, B. Hu, E.R. Kreidler, C. J. Brooks. *The US patent. US8987160* 2015. Grant.

[57] K.M. Cook, H.D. Perez, C.H. Bartholomew, W.C. Hecker. 2014, Appl. Catal. A:Gen, Vol. 482, pp. 275-286.

[58] J. Hu, F. Yu, Y. Lu. 2012, Catalyts, Vol. 2, pp. 303-326.

[59] A.Y. Khodakov, W. Chu , P. Fongarland. 2007, Chem. Rev., Vol. 107, pp. 1692-1744.

[60] E. Van Steen, M. Claeys. 2008, Chem. Eng. and Techno., Vol. 119, pp. 367-374.

[61] R.L. Vannice, L. Garten. 1975, J. Catal., Vol. 63, pp. 345-349.

[62] L. Chacóna, M. Almohalla, E. Gallegos-Suareza, A. Guerrero-Ruizb, I. Rodríguez-Ramos. 2014, Appl. Catal A:Gen., Vol. 480, pp. 86-92.

[63] www.infomine.com/metal-prices. *InvestmentMine.* [Online] 2015.

[64] A. Basinska, L. Kepinski, F. Domka. 1999, Appl. Catal. A: Gen., Vol. 183, p. 143.

[65] F.C. Meunier, D. Tibiletti, A. Gouguet, S. Shekhtman, C Hardacre, R. Burch. 2007, Catal. Today, Vol. 126, pp. 143-147.

[66] C.S. Chen, W.H. Cheng. 2002, Catal. Lett., Vol. 83, pp. 121-126.

[67] C. Liu, T.R. Cundari, A.k. Wilson. 2011, Ing. Chem., Vol. 50, pp. 8782-8789.

[68] S. Hilaire, X. Wang, T. Luo, R.J Gorte, J. Wagner. 2001, Appl. Catal. A:Gen, Vol. 215, pp. 271-278.

[69] A. Goguet, F. Meunier, J.P Breen, R. Burch M.I Petch, A.F. Ghenciu. 2004, J. of Catal. , Vol. 226, pp. 382-392.

[70] V.S. Stenkamp, J.D. Holladay, P.H. Humble, R.A. Dagle, K.P. Brooks. *Non-Recator Micro-Component Development.* 2007.

[71] F. Bustamante, R. Enick, K. Rothenberger, B. Howard, A. Cugini, M. Cioccoand B. Morreale,. 2002, Fuel Chem Divis. Pre., Vol. 47, p. 664.

[72] Tingey, G.J. 1966, Phys. Chem. , Vol. 70, pp. 1406-1410.

[73] S. I. Fujita, M. Usui, N. Takezawa. 1992, J. Catal., Vol. 134, pp. 220-225.

[74] A. G. Kharaji, M. A. Takassi, A. Shariati. 2012, Int. Proc. Chem., Bio. Environ. Eng. , Vol. 30, pp. 118-123.

[75] M. C. Roman-Martinez, D. Cazorla-Amorós, A. Linares-Solano, C. S.-M. n. de Lecea. 1994, Appl. Catal. A, Vol. 116, pp. 187-204.

[76] S. S. Kim, H. H. Lee, and S. C. Hong. 2012, Appl. Catal. A:Gen, Vol. 154, pp. 423-424.

[77] S. S. Kim, K. H. Park, S. C. Hong. 2013, Fuel Process. Technol., Vol. 108, pp. 47-54.

[78] S.G. Jadhav, P.D. Vaidya, B.M. Bhanage, J.B. Joshi. 2015, Canadian J. Chem. Eng., Vol. 94, pp. 101-106.

[79] Holladay, J.D. 2009, Catal. Today, Vol. 139, pp. 244-249.

[80] M. E. Adrover, E. López, D.O. Borio, M.N. Pedernera. 2009, Chem Eng. J., Vol. 154, pp. 196-202.

[81] D. Tibiletti, A. Goguet, F.C. Meunier, J.P. Breen, and R. Burch. 2004, Chem. Commun., Vol. 14, pp. 1636-1641.

[82] S. Scir`e, C. Crisafulli, R. Maggiore, S. Minic`o and S. Galvagno. 1998, Catal. Lett., Vol. 51, pp. 41-45.

[83] D.W. Jeong, W.-J. Jang, J.-O. Shim, W.B. Han, H.S. Roh, U. H. Jung, and W.L. Yoon. 2014, Renew. Energy, Vol. 65, pp. 102-107.

[84] J.A. Amels, L.H. Schwartz, J.B. Butts. 1981, J. Catal., Vol. 72, pp. 95-110.

[85] Wagner, C. Ratnasamy and J. P. 2009, Catal. Rev., Vol. 51, pp. 325-440.

[86] S. Natesakhawat, X. Wang, L. Zhang, and U. S. Ozkan. 2006, Catal. A Chem, Vol. 260, pp. 82-94.

[87] Ghenciu, A.F. 2002, Sol. State Mater. Sci., Vol. 6, pp. 389-399.

[88] M. Peters, B. Köhler, W. Kuckshinrichs, W. Leitner, P. Markewitz, T.E. Müller. 2011, ChemSusChem, Vol. 4, pp. 1216-1221.

[89] Y. Choi, K. Futagami, T. Fujitani, J. Nakamura. 2001, Appl. Catal. A, Vol. 208, pp. 163-169.

[90] J. Toyir, M. Saito, I. Yamauchi, S. Luo, J. Wu, I. Takahara, M. Takeuchi. 1998, Catal Today, Vol. 45, pp. 24-30.

[91]A. Basińska, T.P. Maniecki and W.K. Jóźwiakb. 2006, Catal. Lett., Vol. 89, pp. 319-324.

[92] A. Basinska, F. Domka. 1997, Catal. Lett., Vol. 43, p. 59.

[93] A. Barinska, T. Maniecki, W. Jozwiak. 2006, React. Kinet. Catal. Lett. , Vol. 89, pp. 319-324.

[94] T. Tabakova, V. Idakiev, D Andreeva, I Mitov. 2000, Catal. A Gen., Vol. 202, pp. 91-97.

[95] T. Bunluesin, R.J. Gorte, G.W. Graham. 1998, Appl. Catal. B, Vol. 15, pp. 107-112.

[96] Newsome, D.S. 1980, Catal. Rev. Sci. Eng. , Vol. 21, pp. 275-282.

[97] A. Jha, D.W. Jeong, W.J. Jang, C. V. Rode, H.S Roh. 2015, RSC Adv., Vol. 5, p. 1430.

[98] D. Andreeva, V. Idakiev, T. Tabakova. 1998, J. Catal., Vol. 158, pp. 354-355.

[99] D.C. Grenoble, M.M. Estadt. 1981, *J. Catal,* Vol. 67, pp. 90-102.

[100] P. Panagiotopoulou, D. I. Kondarides. 2006, Catal. Today, Vol. 112, pp. 49-52.

[101] O. Thinon, F. Diehl, P. Avenier, Y. Schuurman. 2008, Catal. Today, Vol. 134, pp. 137-143.

[102] X. Wenqian, S. Rui, S. Senanayake , J. Llorca , H. Idriss , D. Stacchiola, J.C. Hanson, J.A. Rodriguez. 2012, *J Catal*., Vol. 291, pp. 117-126.

[103]. J.D. Halloday, R.A. Dagle, D.R. Palo. 2007, *Chem. Rev*, Vol. 107, pp. 3992-4003.

[104] U Toshimasa, O. Takeou, T. Tatsuya, K. Ryuji, E. Koichi. 2003, Appl. Catal A:Gen, Vol. 245, pp. 343-351.

[105] *C.* B. M. Reddy, P. Bharali, P. Saikia, A. Khan, S. Loridant, M. Muhler, W. Grunert. 2007, *J. Phys. Chem.*, Vol. 111, p. 1878.

[106] Pinna, F. 1998, Catal. Today, Vol. 41, pp. 129-137.

[107] Bond, G. C. *Heterogenous Catalysis.* s.l. : Claredon Press, 1974.

[108] Jin, R. 2012, Nanotechnol. Rev., Vol. 1, p. 31.

[109] S. Royer, F. Berube, S. Kaliaguine. 2005, Appl. Catal. A: Gen, Vol. 282, pp. 273-284.

[110] M.J.L. Gines, A.J. Marchi, C.R. Apestegula. 1997, Appl. Catal. A:Gen, Vol. 154, pp. 155-171.

[111] Cardatos H, Bunluesin T, Stbenrauch J, Vohs JM, Gorte RJ. 1996, J Phy Chem , Vol. 100, pp. 758- 789.

[112] Y. Xia, J. Chen, T.E. Herricks. *United States Patent. US8114187 B2* US, 2005. Grant.

[113] Y-C Wei, C-W Liu, W-J Chang, K-W Wang. 2011, J. of All. and comp., Vol. 509, pp. 535-541.

[114] R.M. Lain, A. Sellinger. *United States Patent. 960 B1* 2003.

[115] H. Dong, Y.C. Chen and C. Feldmann. 2015, Green Chem., Vol. 17, pp. 4107-4132.

[116] P. Toneguzzo, G. Viau, O. Acher, F. Guillet, E. Bruneton and F. Fievet, J. Mater. Sci., 2000, 35, 3767. 2000, J Master. Sci., Vol. 35, p. 3767.

[117] E.A. Baranova, C. Bock, D. Ilin, D. Wang, B. MacDougall. 2006, Surface Science, Vol. 600, pp. 3502-3511.

[118] Y. Pe, P. Wu, X. Zhang, T. Zhou, X. Tang, Y. Zhou and T. Lu, RSC Adv., 2014, 4, 17401. 2014, RSC adv, Vol. 4, p. 17401.

[119] H. Hei, H. He, R. Wang, X. Liu, G. Zhang. 2012, Soft Nanosci. Lett., Vol. 2, pp. 34-40.

[120] Wei Cai, Jiaqi Wan. 2007, Vol. 305, pp. 366-370.

[121] G. Viau, F Fievet-Vincent and F. Fievet. 1996, J. Mater. Chem., Vol. 6, pp. 1047-1053.

[122] R. J Joseyphusa, D. Kodamaa, T. Matsumotob, Y. Satoa, B. Jeyadevana,K. Tohjia. 2007, J. of Magnetism and Magnetic Materials, Vol. 310, pp. 2393-2395.

[123] T. Zheng, J. He, Y. Zhao, W. Xia, J. He. 2014, J. Rare Earths, Vol. 32, p. 97.

[124] R.D. Green, *Carbon Dioxide Reduction on Gadolina Doped Ceria Cathodes.* Case Wester Reserve University. 2009.

[125] P. Vernoux, L. Lizarraga, M. N. Tsampas, F. M. Sapountzi, A. De Lucas-consuegra, J. Valverde, S. Souentie, C. G. Vayenas, D. Tsiplakides, S. Balomenou, and E. A. Baranova,. 2013, Chem. Rev. .

[126] H. Yahiro, Y. Eguchi, K. Eguchi, and H. Arai. 1988, J. Appl. Electrochem., Vol. 18, pp. 527-531.

[127] Huang, W. Dow and T. 1994, J. Catal.

[128] Gazquez, M. G. Sanchez and J. L. 1987, J. Catal, Vol. 104, pp. 120-135.

[129] M. Machida, K. Eguchi, and H. Arai. 1987, J. Catal, Vol. 103, pp. 385-393.

[130] M. Stoukides, G. Vayenas. 1981, J. Catal., Vol. 70, pp. 137-146.

[131] P. Vernoux, M. Guth, and X. Li. 2009, Electrochem. Sol-Sta. Lett., Vol. 12, pp. 567-571.

[132] Sung Su Kim, Hyun Hee Lee, Sung Chang Hong. 2012, Appl. Catal. A:Gen, Vol. 423, pp. 100-107.

[133] C.M. Kalamaras, P. Panagiotopoulou, D.I. Kondarides, A.M. Efstathiou. 2009, J. catal, Vol. 264, pp. 117-129.

[134] C. Chen, C. Ruan, Y. Zhan, X. Lin, Q. Zheng, and K. Wei. 2014, Int. J. Hydrogen Energy, Vol. 39, pp. 317-324.

[135] S. Hosokawa, M. Taniguchi, K. Utan, H. Kanai, S. Mamura. 2005, Appl. Catal. A Gen, Vol. 289, pp. 115-121.

[136] Â. Omil, J. M. Pintado, S. Bernal, J. J. Calvino, M. A. Cauqui, J. M. Gatica, C. Larese, J. A. Pe, A. Metalu. 1999, Catal. Today, Vol. 50, pp. 175-182.

[137] A. S. Ivanova, E. M. Slavinskaya, R. V. Gulyaev, V. I. Zaikovskii, O. A. Stonkus, I. G. Danilova, L. M. Plyasova, A. I. Boronin. 2010, Appl. Catal. B Environ., Vol. 97, pp. 57-65.

[138] H. Miho, T. Naoki, T. Toshitaka, N. Yasutaka, D. Kazuhiko, A. Yuki, Y. Takeru, S. Hirofumi. 2010, Appl. Catal. B Environ. , Vol. 99, pp. 336-346.

[139] R. Strobel, S. E. Pratsinis. 2009, Platin. Met. Rev., Vol. 53, pp. 11-21.

[140] S. J. Tauster, S. C. Fung, R. T. K. Baker, J. A. Horsley. 1981, Science, Vol. 211, pp. 1121-1132.

[141] A. Bruix, J. A. Rodriguez, P.J. Ramírez, S. D. Senanayake, J B. Park, Dario Stacchiola, Ping Liu, Jan Hrbek, and Francesc, 2012, JACS, Vol. 134, pp. 8968-8974.

[142] B. L. Mojet, M. J. Kappers, J. T. Miller, D. C. Koningsberger. 1996, Surf. Sci. Catal., Vol. 101, pp. 1165-1161.

[143] C. Zhang, C.J. Li, G. Zhang, X.-J. Ning, C.X. Li, H. Liao, and C. Coddet,. 2007, Mater. Sci. Eng. B, Vol. 137, pp. 24-30.

[144] C. Li, X.J. Ning, and C.X. Li,. 2005, Surf. Coatings Technol., Vol. 190, pp. 60-64.

[145] G.B. Balazs, R.S. Glass, *2nd International Symposium on Ionic and Mixed Conducting Cermamics.* : Electrochemical Society, 1994.

[146] T. Shimonosono, Y. Hirata, Y. Ehira, S. Sameshima, T. Horita, H. Yokokawa. 2004, Sol. State. Ion., Vol. 174, pp. 27-33.

[147] S.T. Mrowec, *Introduction to Defects and Diffusion in Solids.* 1980. pp. 17-19.

[148] L. Wang, H. Liu, Y. Chen, R. Zhang, S. Yang. 2013, Chem. Lett., Vol. 42, pp. 682-689.

[149] K. Eguchi, T. Setoguchi, T. Inoue, H. Arai. 1992, Solid State Ion., Vol. 52, pp. 165-172.

[150] Ismail, M. *Model Development and Validation of Samaria Doped Ceria (SDC) Based Solid Oxide Fuel Cell Operating with Practical Fuels.* University of Waterloo. 2013.

[151] T. Suzuki, I Kosacki, H U Anderson. 2002, Sol. Stat. Ion., Vol. 151, pp. 111-121.

[152] O. Bohnke, V. Gunes, K. V. Kracchyk, A. G. Belous, OZ Yanchevskii, O. I. V'Yunov. 2014, J of Sol. State Ion., Vol. 262, pp. 517- 521.

[153] Y. Xiong, K. Yamaji, N. Sakai, H. Negishi, T. Horita, H. Yokokawa. 2001, Electrochem. Soc., Vol. 148, pp. 489-492.

[154] K.E Swider, S. Loughin, W.L. Worrel. 1991, Electrochem. Soc., Vol. 324, p. 73.

[155] P. Knauth, H.L. Tuller. 1999, J. Appl. Phys., Vol. 85, pp. 897-902.

[156] H.A.E. Dole, R.J. Isaifan, F.M. Sapountzi, L. Lizarraga, D. Aubert, A. Princivalle, P. Vernoux, E.A. Baranova. 2011, Electrochem. Soc., Vol. 35, pp. 43-57.

[157] C. Ratnasamy, J.P. Wagner. 2009, Catal. Rev., Vol. 51, pp. 325-440.

[158] L. Arteta, A.T. Aguayo, A. Remiro, J. Bilbao, A.G. Gayubo. 2015, Eng. Chem. Res, Vol. 54, pp. 11285-11294.

[159] Tuller, H.L. 1999, Electrochem Soc., Vol. 4, pp. 33-40.

[160] C. Bock, C. Paquet, M. Couillard, G.A. Botton, B.R. MacDougall. 2004, J. Am. Chem. Soc., Vol. 126, pp. 8028-8037.

[161] R.J. Isaifan, E.A. Baranova. 2015, Catal. Today, Vol. 241, pp. 107-113.

[162] *J. Catal.* M. Marwood, C. G. Vayenas. 1998, Vol. 178, p. 429.

[163] M. H. Kim, J. R. Ebner, R. M. Friedman, M. A. Vannice. 2002, Vol. 208, p. 381.

[164] Cullity, B. D. *Elements of X-ray Diffraction.* s.l. : Addison-Wesley, 1978.

[165] R. W. Cornell, U. Schewrtmann. *The Iron Oxides.* 2000.

[166] Lepp, H. *The Am. Mineral.* 1957. p. 679. Vol. 42.

[167] *J Phy. Chem.* K. Starke, Z. Struktur Kinstlicher. 1939, Vol. 42, pp. 159-172.

[168] M. Kobayashi, T. Shirasaki. 1973, J. Catal., Vol. 28, p. 289.

[169] A. Schlapka, U. Kasberger, D. Menzel, P. Jakob. 2002, Surf. Sci., Vol. 502, p. 129.

[170] Boudart, M. 1969, Adv. Catal, Vol. 20, p. 153.

[171] Bond, G. C. *Heterogenous Catalysis: Principles and Application.* s.l. : Clarendon press, 1974.

[172] R.J Isaifan, H.A.E. Dole, E. Obeid, L. Lizarraga, P. Vernoux, E.A. Baranova. 2012, Electrochem. Sol. St. Lett., Vol. 15, pp. E1-E4.

[173] R.J. Isaifan, S. Ntais, M. Couillard, E.A. Baranova. 2015, J. Catal, Vol. 324, pp. 32-40.

[174] Brandon, I. Levin and D. 1998, J Am. Ceramics Soc., Vol. 81, p. 1995.

[175] A. Birds, A. Stiles. *Catalyst Supports and Supported Catalysts.* Boston : Butterworth.

[176] E. Auer, A. Freund, J. Pietsch, T. Tacke. 1998, Appl. Catal. A Gen , Vol. 173, p. 259.

[177] William C. Chueh, Anthony H. McDaniel, Michael E. Grass, Yong Hao, Naila Jabeen, Zhi Liu, Sossina M. Haile, Kevin F. McCarty, Hendrik Bluhm, and Farid El Gabaly. 2012, Chem. Mater., Vol. 24, pp. 1876-1882.

[178] S-F Wang, C-T Yeh, Y-R Wang, Y-C Wu. 2013, J of Mater. Res. and Tech., Vol. 2, pp. 141-148.

[179] *Catal. Lett.* G. Li, D. I. Enache, J. Edwards, A. F. Carley, D. W. Knight, G. J. Hutchings. 2006, Vol. 110, pp. 7-13.

[180] Lindgren T, Wang H, Beermann N. 2002, Sol Energy Mater Sol Cells, Vol. 71, p. 231.

[181] R. J. Byron Smith, M. Loganathan, M. S. Shantha. 2010, Inter. J of Chem. Reac. Eng., Vol. 8, p. R4.

[182] H Yahiro, Y Eguchi, K Eguchi, H Arai. 1988, J. of Applied Electrochemistry, Vol. 18, pp. 527-531.

[183] Karasali, H. *Ph.D. thesis.* Chemical Engineering, University of patras. 1988.

[184] Gorte, RJ. 2010, AlChE J, Vol. 56, p. No 5.

[185] Toshio Suzuki, Igor Kosacki, Harlan U Anderson. 2002, Sol. State Ion., Vol. 151, pp. 111-121.

[186]. J Wright, A. V. Virkar. 2011, *J of Power Sources,* Vol. 196, pp. 6118-6124.

[187] T. Matsui, M. Inaba, A. Mineshige, Z. Ogumi. 2005, Solid State Ionics, Vol. 176, pp. 647-654.

[188] X. J. Wang, J. Renn, J. Spencer, C. Ratnasamy, Y. Cai. 2013, Top. in Catal., Vol. 56, pp. 1899-1905.

[189] Smirnov MY, Graham GW. 2001, *J. Catal*, Vol. 72, pp. 39-44.

[190] Oberlander, R. K. 1984, Appl. Indus. Catal., Vol. 3, p. 67.

[191] Zhang, D. *Morphology Genetic Materials Templated from Nature Species.* 1980.

[192] G. P. Lan, A. A. C. M. Beenackers. 2000, Appl. Catal. A, Vol. 193, pp. 39-53.

[193] Y. Li, Q. Fu, M. Flytzani-Stephanopoulos. 2000, Appl. Caral. B: Env., Vol. 27, pp. 179-191.

[194] A. E. Aksoylu, A. N. Akin, Z. Onsan, D. L. Trimm. 1996, Appl. Catal. A. Gen., Vol. 145, pp. 185-193.

[195] S.J. Sing, K. S. W.Gregg *Surface Area and Porosity.* New York : Academic Press, 1967.

[196] H. Liu, X. Zou, X. Wang, X. Lu, W. Ding. 2012, J of Natu. Gas Chem., Vol. 21, pp. 703-707.

[197] Z. Cheng, B. J. Sherman, C. S. Lo. 2013, Chem. Phys., Vol. 138, p. 147.

[198] E. Kock, M. Kogler, T. Bielz, B. Klotzer, S. Penner. 2013, J. Phys. Chem. C. Nanomater. Interfaces, Vol. 34, p. 117.

[199] D. Theleritis, S. Souentie, A. Siokou, A. Katsaounis, and C. G. Vayenas. 2012, ACS Catal., Vol. 2 (5), pp. 770-780.

[200] C.S. Chen, W.H. Cheng, S.S. Lin. 2004, Appl. Catal. A: Gen., Vol. 257, pp. 97-106.

[201] K. H. Ernst, C. T. Campbell, G. Moretti. 1992, J. Catal., Vol. 134, p. 66.

[202] J. Papavasiliou, G. Avgouropoulos, and T. Ioannides. 2007, Appl. Catal. B Environ., Vol. 69, pp. 226-234.

[203] X. Qi, M. Flytzani-Stephanopoulos. 2007, Ind. Eng. Chem. Res. , Vol. 43, p. 3055.
s
[204] C. S. Chen, W. H. Cheng, S. S. Lin. 2003, Appl. Catal. A: Gen., Vol. 238, pp. 55-67.

[205] Y. Okamoto, T. Kubota, H. Gotoh, Y. Ohto, H. Aritani, T. Tanaka, S. Yoshida. 1998, J. Chem. Soc. , Vol. 94, p. 3743.

[206] Dumesic, D. G. Rethwisch and J. A. 1986, J. Catal., Vol. 101, pp. 35-42.

[207] M. A. Edwards, D. M. Whittle, C. Rhodes, A. M. Ward, D. Rohan, M. D. Shannon, G. J. Hutchings and C. J. Kiely. 2002, Phys. Chem. Chem. Phys. , Vol. 4, pp. 3902- 3908.

[208] A. Matthews, 1976, Am. Miner., Vol. 61, pp. 927-932.

[209] R. K. Grasselli, and J. F. Brazdil. Amer. Chem. Soc. Washington. D.C. : s.n., 1985.

[210] C. R. Lund, J. E Kubsh, J. A. Dumesic. 1985, *Sol. Sta. Chem. in Catal,* Vol. 279, p. 313.

[211] L. Barrio, M. Estrella, G. Zhou, W. Wen, J. C. Hanson, A. B. Hungria, A. Hornes, M. Fernandez-Garcia, A. Martinez-Arias, and J. A. Rodriguez. 2010, J. Phys. Chem. C, Vol. 114, pp. 3580-3587.

[212] C.C Chen, W.H. Cheng, S.S Lin. 2000, Catal. Lett., Vol. 68, pp. 45-48.

[213] Spencer, M. V. Twigg and M. S. 2001, Appl. Catal A Gen, Vol. 212, pp. 161-174.

[214] F. C. Meunier, D. Reid, A. Goguet, S. Shekhtman, C. Hardacre, R. Burch, W. Deng, Flytzani-Stephanopoulos. 2007, J. Catal., Vol. 247, pp. 277-287.

[215] Z. Kowalczyk, K. Stolecki, W. Rarog-Pilecka, E. Miskiewicz, E. Wilczkowska, Z. Karpinski. 2008, Appl. Catal. A: Gen., Vol. 342, pp. 35-49.

[216] F. Solymosi, A. Erdohelyi, M. Kocsis. 1981, J. Chem. Soc. , Vol. 77, pp. 1003-1012.

[217] P. Panagiotopoulou, D. I. Kondarides. 2004, J. Catal., Vol. 225, p. 327-323.

[218] A.L. Kustov, A.M. Frey, K.E. Larsen, T. Johannsessen, J.K. Norskov, C.H. Christensen. 2007, Appl. Catal. A : Gen, Vol. 320, p. 98.

[219] A.M. Abdel-Mageed, S. Eckle, R. Behm. 2015, J. Am. Chem. Soc., Vol. 137, pp. 8672-8675.

[220] S. Eckle, M. Augustin, H.G. Anfang, R. Behm. 2012, J. Catal. Today, Vol. 181, p. 40.

[221] X. Lian, W. Guo, J. Shu, X. Zhang, Z. Liu, Y. Zhang, R. Liu. 2015, Theor. Che,. Acc, Vol. 134, p. 19.

[222] B. Caglayan, A. Aksoylu. 2009, Turk. J. Chem, Vol. 33, pp. 249-256.

[223] W. Xu, R. Si, S. Senanayake, J. Llorca, H. Idriss, D. Stacchiola, J. Hanson, J. Rodriguez. 2012, J. Catal., Vol. 291, pp. 117-126.

[224] N.M. Sammes, Z. Cai. 1997, Sol. Sta. Ion. , Vol. 100, pp. 39-44.

[225] T. Kudo, H. Obayashi. 1975, *J. Electrochem. Soc.,* Vol. 122, pp. 142-147.

[226] B. Coq, P.S. Kumbhar, C. Moreau, P. Moreau, F. Figueras. 1994, J. Phys. Chem. , Vol. 98, pp. 10180-10188.

[227] M.S. Bera, P. Hegdem, 2015, Catal. Today, Vol. 253, pp. 40-50.

[228] J.M. Zalc, V. Sokolovskii, D.G. Loffler. 2001, Appl. Catal. A: Gen, Vol. 215, p. 271-277.

[229] G. Jacobs, L. Williams, U. Graham, G. Thomas, D. Sparks, B. Davis. 2003, Appl. Catal A: Gen, Vol. 252, pp. 107-118.

[230] A. Holmgren, B. Andersson. 1998, J. Catal. , Vol. 178, p. 14.